COMMISSIONING AND CHARACTERIZATION OF THE NSCL'S LARGE VOLUME
LINEAR GAS CELL

By

Kortney Lynn Cooper

A DISSERTATION

Submitted to
Michigan State University
in partial fulfillment of the requirements
for the degree of

Chemistry - Doctor of Philosophy

2016

ABSTRACT

COMMISSIONING AND CHARACTERIZATION OF THE NSCL'S LARGE VOLUME LINEAR GAS CELL

By

Kortney Lynn Cooper

The thermalization of fast moving ions plays a pivotal role in the ability of projectile fragmentation facilities such as the National Superconducting Cyclotron Laboratory (NSCL) to provide experimenters with low-energy ion beams for precision experiments. The NSCL produces radioactive ion beams (RIBs) with kinetic energies of the order ∼100 MeV/u and velocities of up to half the speed of light. More than ten years ago, the NSCL first proposed and demonstrated a beam thermalization technique for projectile fragments [1]. In order to provide beams with energies on the order of ∼10 keV, the fast RIBs first pass through a dispersive ion-optical system, solid degraders, and then a monoenergetic wedge to remove the bulk of their kinetic energy. The remaining kinetic energy of ∼1 MeV/u is then dissipated through collisions with the buffer gas atoms in a large volume linear gas cell. The original NSCL gas cell was compact (5 cm wide x 50 cm long), ran at a high pressure (750 torr), and used a DC drag field and gas flow to guide and extract the ions [1]. The new, large volume linear gas cell constructed by Argonne National Lab (ANL), is larger (25 cm x 120 cm), operates at medium pressures (55 to 100 torr), and employs an elaborate electrode structure with both static and dynamic electric fields as well as gas flow to guide and to extract the thermalized ions. The present work describes a series of commissioning experiments for the NSCL's large volume linear gas cell that were conducted using ^{76}Ga beams produced at approximately 90 MeV/u in the A1900 [2]. Since the commissioning experiments, numerous additional ion beams have been thermalized and extracted from this gas cell, and some

of the results are also presented here. The fast beams were delivered to the large volume linear gas cell in a new momentum compression beam line, and the range distributions, extraction efficiency, and the overall efficiency of the system were measured as a function of the incident intensity. The data from the commissioning runs were compared to predictions from the stopping and range of ions in matter (SRIM) code [3, 4] and the LISE++ code [5, 6]. Particle-in-cell (PIC) calculations [7] were carried out to evaluate the space charge produced by the stopping of the energetic fragments, and finally, SIMION calculations [8] of the ion migration in the gas cell were performed to evaluate the effectiveness of the changes and upgrades from the previous cell. Results from these studies revealed that the larger size, upgraded electrode structure, and additional dynamic potential on the walls and cone of the NSCL's large volume linear gas cell did, in fact, improve the extraction efficiency of the system when compared to previous generation devices.

TABLE OF CONTENTS

LIST OF TABLES

LIST OF FIGURES

x

Chapter 1

Evolution and Impementation of the Gas Cell

Radioactive beam facilities can be divided into two categories–those based on Projectile Fragmentation (PF) and those based on Isotope Separation On-Line (ISOL). Projectile fragmentation facilities produce secondary RIBs by impinging a high energy primary beam on a relatively thin target. The fragments are separated and collected "in-flight" for transit to the experimental areas. In contrast, ISOL facilities bombard a thick target with a very intense, light-ion beam. The secondary products then diffuse out of the target, and the beam is created and separated for transport to the experimental areas [9]. Due to the nature of the secondary beam production, these secondary beams have low and precise energies as well as low emittances. Low-energy precision techniques and experiments were therefore primarily developed at and exclusive to ISOL facilities.

Although ISOL methods produce very high quality beams, the accessible ions are limited to those with longer half lifes and the chemical properties required to survive the diffusion process. In order for projectile fragmentation facilites, whose processes are unhindered by diffusion, to deliver similar types of beams for low-energy experiments, the fast fragments produced must be thermalized. A key element of beam thermalization is the gas cell. Over the years, gas cells have evolved from simple designs that solely relied on gas flow and/or
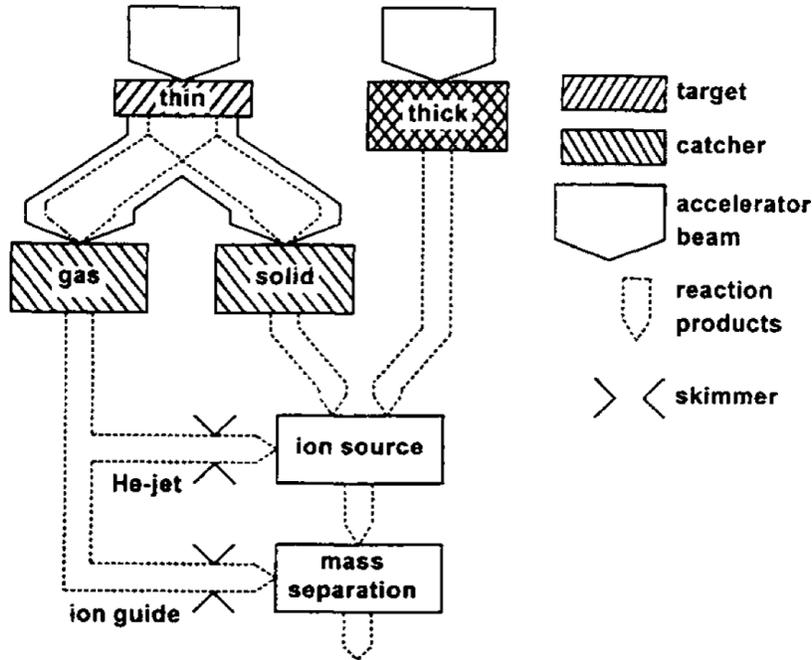
Figure 1.1: The most important ISOL concepts are depicted to show the various ways the reaction products are stopped. The left side depicts the recoil method while the right side shows the diffusion method [10].

DC drift fields to more complex designs that include RF carpets and even RF walls. Both low energy facilities and gas cells are discussed within this chapter.

1.1 Isotope Separation On-Line (ISOL)

The traditional ISOL method, as mentioned above, involves bombarding a thick target with an intense light ion beam. Atoms of interest then diffuse out of the target and are transported by bulk gas or molecular flow to the ion source. Diffusion and separation times of this method limit the observable iosotopes to those that are not only mobile, but longer lived. Given these restrictions, more techniques were developed to collect nonvolatile and shorter-lived species.

For such species, two methods were employed that exploited the kinetic energy and motion of the recoiling reaction products. In both methods, a thin target, whose thickness is
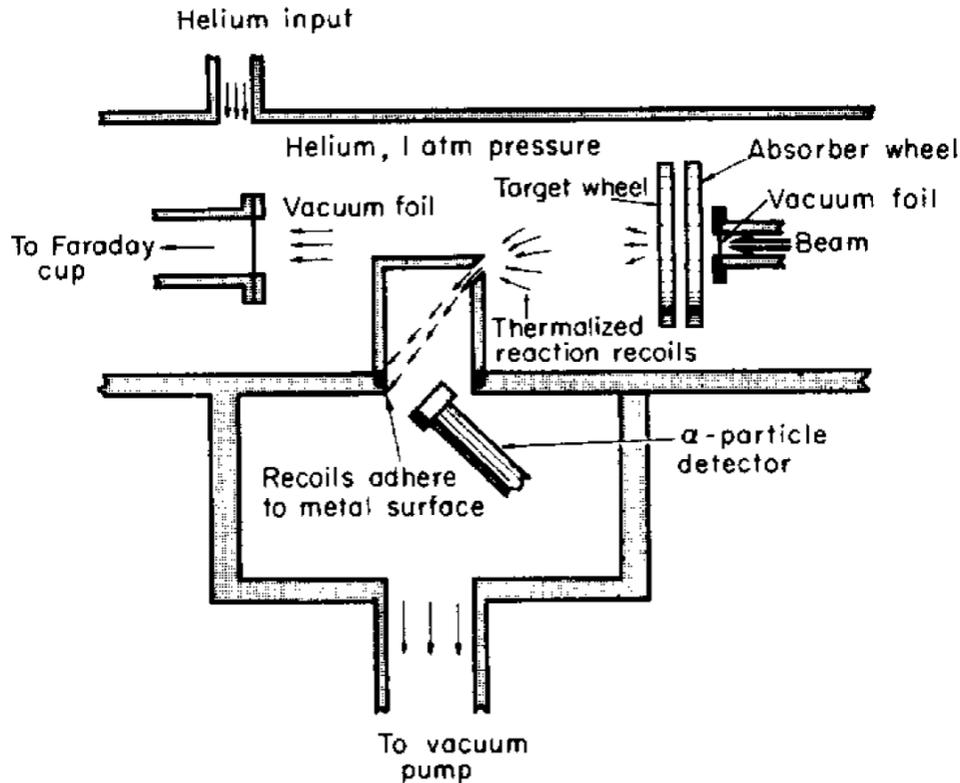
Figure 1.2: Schematic diagram of alpha emitter target with He-jet assembly and detector set-up [11].

limited by the recoil range, is bombarded by a light-ion beam. The reaction products recoil out of the target and are thermalized in either a solid stopper or a gas stopper. A summary of these techniques is depicted in Fig. 1.1 [10].

He-jets were introduced as a means to improve efficiencies and transport times of the recoiling nuclei from the gas stopping targets to distant detectors or an ion source [12]. Scientists studying short lived alpha emitters ($t_{1/2} \sim 0.06$ s) [11] first employed this type of set-up for off-line experiments, where the beam is produced by a source. A schematic of this He-jet set-up can be found in Fig. 1.2 [11].

Over the next few years, He-jet systems continued to evolve and improve as studies of impurity cluster size [13] as well as various gas and vapor carriers [14] and aerosol generators

[15] were explored. The best aerosols found to efficiently transport the ions were NaCl and carbon clusters. After these findings, aerosol-loaded He-jets were incorporated into on-line experiments first conducted at Oak Ridge National Laboratory (ORNL) [16] and the University of Jväskylä [17]. These systems were shown to achieve total efficiencies between 0.01% and 1.00%, and have since been incorporated at other facilities including Chalk River Laboratories (CRL) [18] and Japan Atomic Energy Research Institute (JAERI) [19].

Although He-jets improved on the extraction times observed for the traditional ISOL method, short-lived nuclei ($t_{1/2} \leq 10$ ms) were still inaccessible due to the transport and ionization times associated with an ion source. Since reaction products are neutralized upon adhering to the surface of the aerosols within the He-jet, and ions are required for acceleration and mass separation, the realization of ions from the cluster was a severely limiting step. As such, the ion source was pivotal to the overall performance of any ISOL facility, and a wide variety of sources were available, tested, and used. For detailed discriptions of the design and function of these sources, see [20] and [21] and references therein. In order to study more exotic, shorter lived isotopes, the dependence of these facilities on the ion source had to be alleviated.

1.2   IGISOL

Ion extraction advances at ISOL facilities were built off of the concepts established with the He-jet system, and a new technique was developed that was no longer dependent on an ion source. The Ion-Guide Isotope Separation On-Line (IGISOL) method allowed the bulk of the reaction products to retain a positive charge which therein, renders an ion source irrelevant.
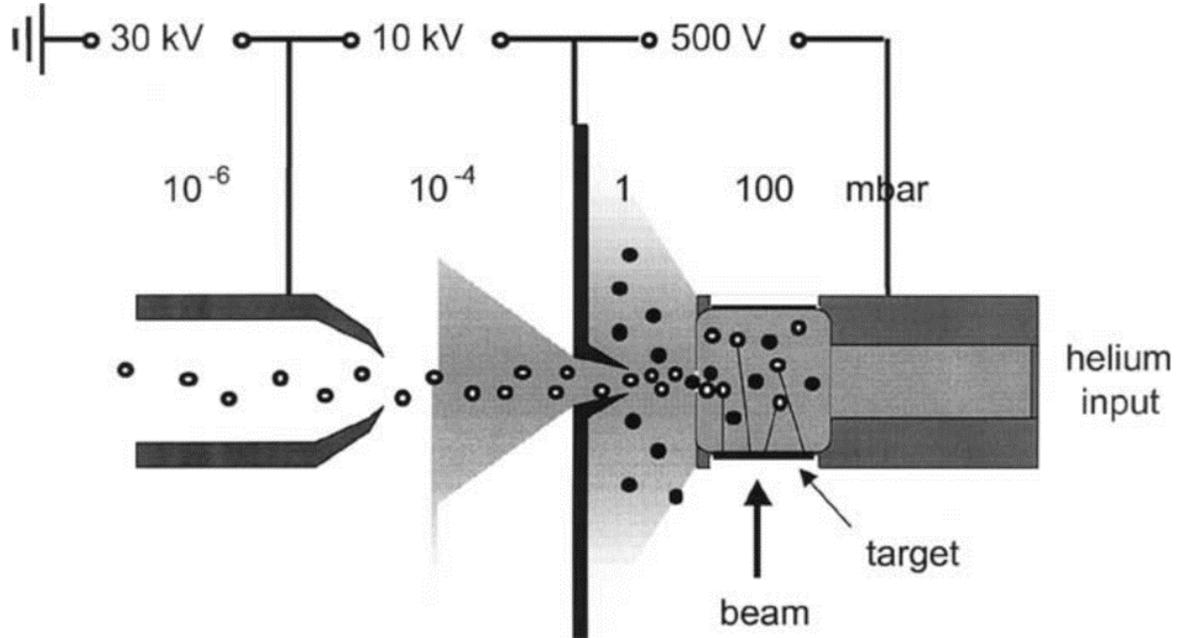
Figure 1.3: The principle of the ion guide involves first thermalizing primary reaction products in a gas chamber and then transporting these products by gas flow and electric fields directly into the accelerating section of the mass separator [22].

1.2.1 Components and Principles of ISOL-Gas Catchers

The components of an IGISOL system include: a gas-filled target chamber where the reaction products are thermalized, an exit nozzle through which the reaction products as well as the helium, or thermalizing gas, atoms are accelerated and columnated, a skimmer designed to simultaneously avert helium atoms while focusing the ions of interest, and a differential pumping system complete with electric fields to remove the helium atoms and continue to guide the ions directly into the mass separator. These components are depicted in Fig. 1.3 [22]. A brief summary of the development of the IGISOL concept will be discussed below. For further details, please see references herein.

The stopping power of the gas chamber and the range of the ions were key to determining chamber sizes and operating pressures. Due to the lower energy of the reaction products, these ions lose their kinetic energy and are thermalized through collisions with the buffer

gas atoms of the gas chamber. The linear stopping power, S, for a given medium is given by the formula [23]:

$$S = -\frac{dE}{dx},$$

(1.1)

where $\frac{dE}{dx}$ is the rate at which energy is lost as the particle moves through the material, or the specific energy loss. S increases as the particle velocity decreases, and for particles with a given charge state, the Bethe formula for the specific energy loss is [23]:

$$-\frac{dE}{dx} = \frac{4\pi e^4 z^2}{m_o v^2} \rho_N B,$$

(1.2)

where e is the fundamental charge of an electron, z is the charge of the primary particle, m_o is the rest mass of an electron, v is the velocity of the primary particle, ρ_N is the number density of the material, and B is a parameter dependent upon the medium and ion velocity [23]:

$$B \equiv Z \left[ln\frac{2m_o v^2}{I} - ln\left(1 - \frac{v^2}{c^2}\right) - \frac{v^2}{c^2} \right].$$

(1.3)

Here, Z is the atomic number of the stopping material, I is the average energy for ionization of the material, and c is the speed of light.

The Bethe fomula (1.2) shows the significant dependence of specific energy loss on a particle's velocity. As such, for most of its track through a material, a particle's specific energy loss increases roughly as $1/E$. As the particle comes to rest, however, its interaction cross section increases, and near the end of its track, the charge is reduced through electron pickup and the $\frac{dE}{dx}$ goes to zero. This characteristic behavior for stopping power as a function of path length, or range in the material, is known as a Bragg curve [23]. The range of a particle through a given material, R, is therefore dependent upon the stopping power and

can be defined as [4]:

$$R = \int_{E_O}^{0} \frac{dE}{dE/dx},$$

(1.4)

where E_O is the initial kinetic energy of the ion and $- dE/dx$ is the energy loss function of the ion. Given the range and initial energies of the reaction products, these ions were expected to range-out and to be completely thermalized by the gas.

The IGISOL method was first tested off-line by using an ^{227}Ac source, and the experimental set-up can be found in Fig. 1.4 [24]. Not only did this method reduce the transport times from the ~10 ms times achieved with He-jets down to ~1 ms, but the total efficiency, which includes mass separation, was reported to be a minimum of five times higher at ~5% with roughly 98% of the decay products leaving the ion guide in a +1 charge state. Since this was purely a proof of concept experiment, it is important to note that this efficiency was obtained without significant time or effort spent on system optimization [24]. These results prompted researchers to conduct further experiments to explain the +1 charge rentention prior to the first on-line experiments. Three main processes were proposed to produce charged ions within the gas: internal ionization, Auger cascades, and stripping in helium [10, 22].

These processes were believed to create high and very distributed charge states among the reaction products. The charge state, which is generally proportional to the ion's velocity, is therefore constantly changing and reset by charge exchange reactions while slowing down in the gas [10, 22]. Collisions between the charged reaction products and the neutral helium atoms were thought to reduce the charge states to +2 with the final reduction to +1 occurring from collisions with impurity molecules found within the helium [25]. Ions then remain in the +1 charge state due to a lack of energetically favored reactions within the gas [10]. A full
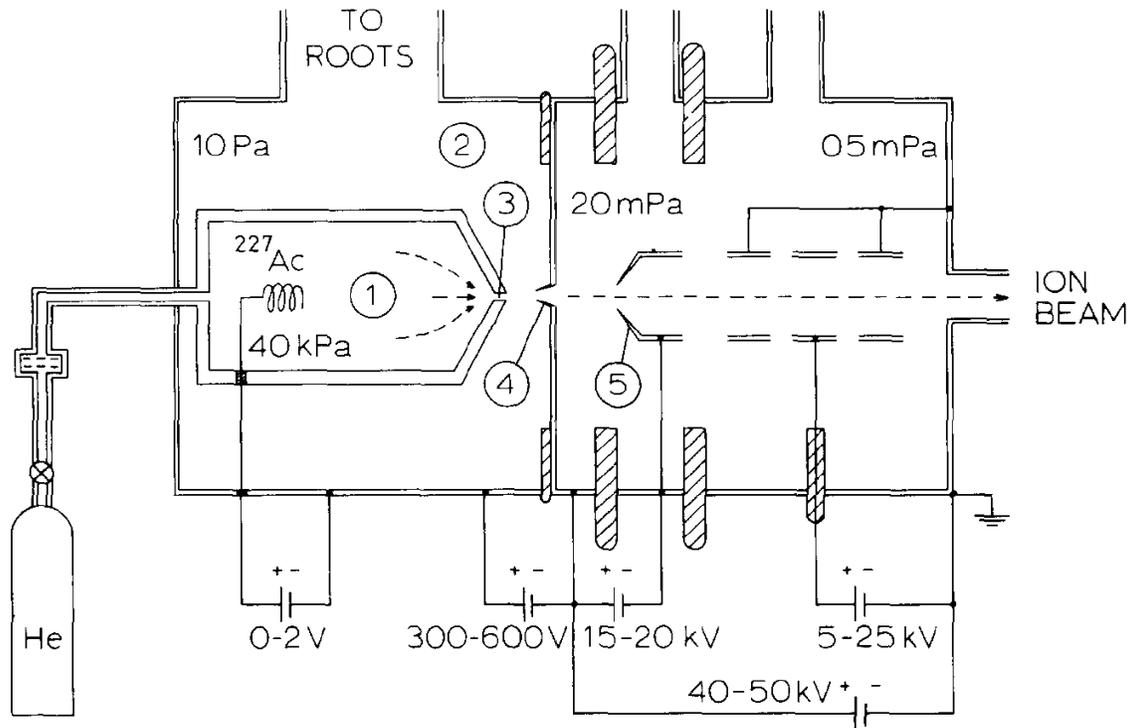
Figure 1.4: Schematic diagram (not to scale) of a Helium-jet ion guide connected to the accelerator stage of a mass separator where (1) is the Recoil chamber, (2) is the vacuum chamber, (3) is the capillary, (4) is the skimmer, and (5) is the extraction electrode [24].

understanding of the ion-gas reactions and ion losses within the gas was therefore essential to further improve these systems.

1.2.2   Reaction Losses and Mechanisms within the Gas

Although the efficiency of ions leaving the ion guide in a +1 charge state is nearly perfect, the overall efficiency of the system is significantly lower. Numerous losses occur within the gas that either prevent ions from leaving the guide or from being collected if they do in fact leave. These ion losses occur through three main processes: diffusion to the chamber walls, formation of molecular ions with impurities in the buffer gas, and neutralization [10, 22, 26].

Diffusion either causes ions to neutralize or to stick to the walls of the chamber. These

ions are usually trapped after they reach thermal energies and are lost for mass separation. Although thermal motion is unavoidable, significant losses from diffusion can be avoided with careful consideration of the chamber geometry and flow trajectories, increasing the gas pressure or mass of the stopping gas, and decreasing the evacuation time of the chamber by increasing the flow rate [10].

Another loss mechanism that occurs within the gas is molecular ion formation. Impurities in the helium gas allow the reaction products to attain the previously mentioned +1 charge state. Large reaction cross sections also exist between the impurities and the ions of interest that lead to the formation of molecular ions [22]. These molecular ions can form within the gas, but can also form after the ions exit the gas cell. While these molecules are still charged and can reach the mass separater, the effective mass of the ion of interest is unvariably increased. These increased reaction pathways lead to a fractionalized beam where the ion of interest is spread over a wide mass range instead of concentrated at one mass as a bare ion. Since statistics are paramount and molecular compounds react differently than bare ions, a fractionalized beam is not ideal for experiments. The losses from the mass shift and fractionalization vary depending on the mass range or resolution of the system, but reducing the number of impurites within the gas would reduce these losses [26].

Despite the significant losses from diffusion and molecular ion formation, the final and most important loss mechanism within the gas is neutralization, which occurs at very high beam rates due to the plasma effect [26]. As the primary beam and/or the reaction products propogate through the gas, a large density of ion-electron pairs are created ($\sim 10^5$ pairs/incoming ion). The lighter electrons are much more mobile than the heavier cations and can be collected almost immediately by applied electric fields. This ionization and resultant build up of positive charge, or space charge potential, creates numerous problems,

9

including: shielding of any electric fields, pushing thermal ions out of the central gas flow and toward the walls, and facilitating three-body neutralization.

In order to understand how space charge builds up, it is important to know the significant reaction mechanisms within the gas. Although monomer gas ions, He^+, are created by collisions with the primary beam or the reaction products, these monomers quickly dimerize to He_2^+ in the three-body reaction [26]:

$$He^+ + 2He \rightarrow He_2^+ + He. \qquad (1.5)$$

Due to their lower ionization potential, impurities in the helium gas can then charge-exchange with this dimer to ionize and to dominate the charge of the plasma. Nitrogen is used as an example below [26]:

$$He_2^+ + N_2 \rightarrow 2He + N_2^+. \qquad (1.6)$$

The larger the residual positive charge, the more likely any applied electric fields will be shielded and the more likely the ions of interest will be pushed towards the walls. As discussed above, this behavior either leads to the ions of interest being trapped in the plasma or lost on the walls through diffusion, respectively. To prevent the impurities from becoming the dominant charge carriers, and thereby determing the charge in the plasma, it is important to keep their presence to a minimum. Even if the helium dimer is the dominant charge carrier, a positive space charge potential can still develop because of the various ion mobilities–electrons move $\sim$1000 times faster than their cation partners.

If this space charge potential shields the applied electric fields, a weak plasma is created where the ions of interest, electrons, and netral helium atoms no longer migrate which

facilitates three-body neutralization as shown below [26]:

$$X^+ + e^- + He \rightarrow X + He, \tag{1.7}$$
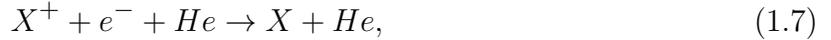
where X^+ is an ion of interest or buffer gas ion, e^- is an electron, and B is a buffer gas atom [26].

The space charge and plasma effects are apparent in the non-linear reduction in extraction efficiency as a function of the incoming beam intensity. This beam intensity affect can be scaled to show the same trend for all gas catcher facilities independent of buffer gas chosen, volume of gas used, energy of projectiles, or electric fields present [10, 22, 26]. The parameter used for these comparisons is the ionization-rate density, Q [26]:

$$Q = 6.25 \times 10^{12} \, \frac{I}{A} \, \frac{dE/dx}{W}. \tag{1.8}$$

that gives the density of ion-electron pairs created for an incoming beam intensity, I (pμA), the area of the beam spot, A (cm^2), the linear energy loss of the ion, dE/dx (eV/cm), and the energy required to produce an ion-electron pair, W (41 eV for He) [26]. Unnavoidable losses occur within the gas at high rates no matter the design or set-up of the system, although variations in efficiency occer depending on the reaction products studied as discussed below.

1.2.3 Efficiencies of Various Reaction Products

Three main types of ion guides exist that are meant to accomodate the reaction kinematics of a given experiment: light-ion ion guides, heavy-ion ion guides, and fission ion guides [26]. The first ion guides were designed to thermalize and to transport reaction products

from light-ion induced fusion evaporation reactions. These ion guides had a simple design consisting of a cylinder with a target mounted directly into the stopping volume of the cell and an exit-hole at the opposite end. Products from these reactions recoil in the forward direction with any accelerator beam and then both the products and beam enter the stopping chamber. Effective stopping volumes of these ion guides are on the order of a few cm^3 with a typical exit nozzle diameter of ∼1 mm which facilitates extraction times as short as 1 millisecond and efficiencies that vary between 1% and 10% [10, 22, 26].

Heavy-Ion-Guide Isotope Separation On-Line (HIGISOL) guides were designed for heavy-ion induced fusion-evaporation reactions. These reaction products are peaked in the forward direction, and again both the reaction products and the accelerator beam penetrate into the chamber. Here, targets were installed along the beam axis on a water-cooled frame upstream of the stopping volume. Effective stopping volumes were somewhat larger, on the order of hundreds of cm^3, with a typical exit nozzle diameter of still only ∼1 mm [26]. Initial results from these ion guides showed reduced efficiencies compared to their light-ion counterparts. This decrease in efficiency was attributed to less efficient stopping of the more energetic recoils and to the ionization produced by the primary ion beam in the stopping gas which leads to space charge and plasma effects [22].

Three main methods were employed to reduce the losses associated with the primary accelerator beam [10]. In the first method, reaction products were separated from the primary beam by a gas-filled dipole magnet, whereby the ion guide efficiencies reached 10% to 40% [22]. The second method, dubbed the "shadow method," exploited the angular distribution of the reaction products, and a "plug" was used to supress the primary beam [10, 22, 26]. Overall efficiencies for this set-up reached nearly 1%. The third method was more advanced and will be discussed later. This method involves laser ionization with a pulsed primary beam
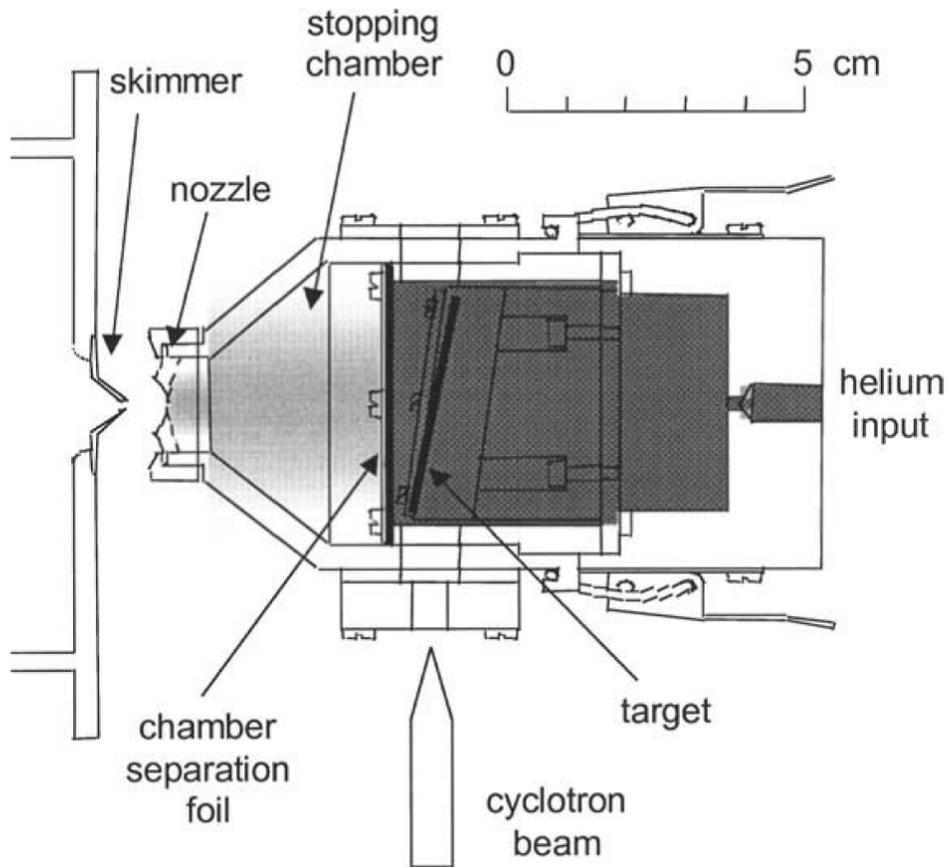
Figure 1.5: Schematic of a fission ion guide operated by the University of Jyväskylä [22].

[22]. Extraction times for these ion guides was on the order of hundreds of milliseconds with 0.04% efficiencies [26].

Fission ion guides were used to collect products from the proton-induced fission of uranium, or other actinide targets [26]. The effective stopping volumes and extraction nozzles of these guides are similar to those of HIGISOL, on the order of a hundred cm^3 and $\sim$1 mm, respectively. Unlike the previous reaction products, though, fission products are emitted isotropically in space, which allowed the reaction products to be physically separated from the primary beam. Several designs to separate the fission products from the primary beam were tested and used, including the use of a separation foil. An example of such an ion guide set-up is shown in Fig. 1.5 [22]. The plasma effect was still observed, however,

and was attributed to the ionization created by the fission fragments themselves. Moreover, only $\sim$30% of the fission products enter the stopping chamber, and the stopping efficiency was reported to only be $\sim$1% [10, 26]. As expected with increased space charge and plasma effects, absolute effeiciencies of these systems were on the order of a few tens of thousandths, with the ions of interest more often than not being overshadowed by unwanted isobars. Laser ionization was also implemented in these ion guides [26] and will be discussed in the next section on advanced systems.

1.2.4 Advanced IGISOL Systems

Numerous advances to the IGISOL method were developed and employed to overcome the plasma effect and improve the beam quality. Upgrades included the laser ion guide, the squeezer ion guide, and the sextupole ion-beam guide (SPIG) [10, 22, 26]. For standard IGISOL set-ups, the voltage placed on the skimmer accelerates the ions through the higher pressure region located between the exit hole and the skimmer itself. Ions can collide with neutral helium atoms before they are removed, which causes an energy spread in the beam [27].

This energy spread significantly reduces the mass resolving power (MRP) of the system [10]. Here, the MRP is defined as $m/\Delta m$ where m is the mass of the ion separated and Δm is the full width at half max (FWHM) of the ion's mass peak [27]. The easiest proposed solution for improving the MRP, without reducing the beam intensity, was to bring the ions into high vacuum before they were accelerated, this concept was first implemented by the University of Jyväskylä in their so-called "squeezer" ion guide depicted in Fig. 1.6 [27]. In this guide, the ions were focused through the skimmer with both viscous drag of the helium flow and weak electric fields [10]. Three rings, all with voltages less than 25V, were placed
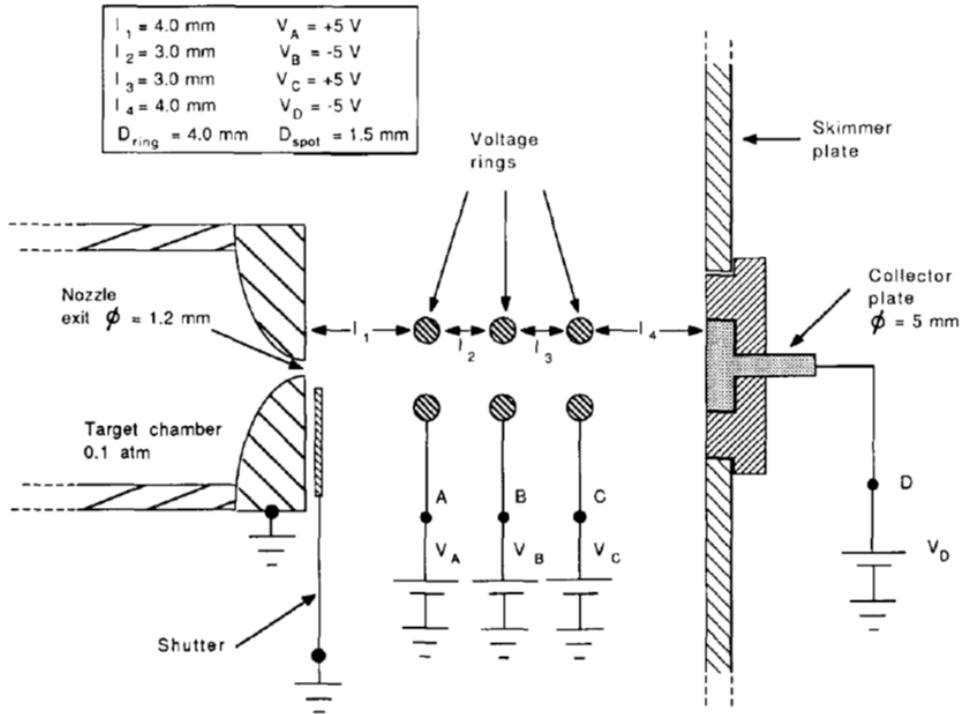
Figure 1.6: Typical geometry and electric potentials of a squeezer with three grids operated between the exit hole and skimmer [27].

between the exit hole and the skimmer. Given the experimentally determined geometries for the grids, off-line tests showed that the transport efficiency was about 75% with an energy spread (FWHM) of 2.5 eV. Although adding a squeezer did not improve the online yields, the MRP more than doubled [10].

With the intent of producing well-focused beams with small energy spreads, another improvement to the IGISOL method was the addition of a sextupole ion-beam guide (SPIG). The SPIG, which was developed by the University of Tokyo's Institure for Nuclear Study, consists of six circular rods distributed uniformly on a circle. Every other rod is connected to the opposite phase of an alternating radio frequency voltage [10]. As seen in Fig. 1.7 [28], the SPIG is located just downstream of the stopping chamber, eliminating the need for a skimmer voltage. No applied skimmer voltage and the implementation of the SPIG decreased
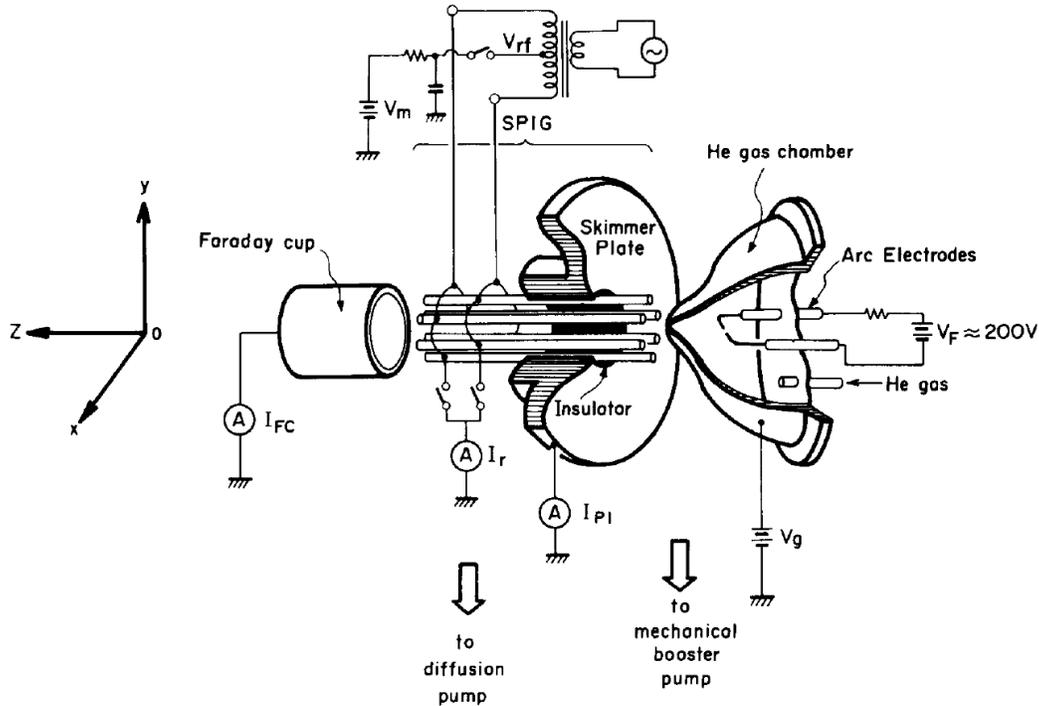
Figure 1.7: Schematic of SPIG set-up used for the study of ions produced by a discharge ion source at the University of Tokyo's Institure for Nuclear Study [28].

the energy spread (FWHM) to 0.8 eV and increased the transport efficiency to 90%, but it also resulted in most of the ions leaving the ion guide in molecular form. The small energy spread of the beam is maintained because the ions are re-thermalized in the first part of the SPIG, which operates at a high helium pressure. As for the molecular ion-formation, the voltage on the skimmer would normally accelerate the ions to an energy whereby the molecular ions would be broken by collisions with the buffer gas ions. In order to obtain similar results, the SPIG was placed $\sim$150 V below the voltage applied to the ion guide [10].

In an attempt to overcome plasma effects, as well as provide atomic number selectivity, a resonant laser ionization scheme was developed [22]. The Leuven Isotope Separation On-Line (LISOL) group in Leuven mainly pioneered this technique. In order to achieve neutralization of the recoiling nuclei prior to selective ionization of the laser, the exit hole for this technique

could only be 0.5 mm, not the standard 1.2 mm, which led to lower extraction times. In addition laser ionization only produces a weakly-ionized plasma, the required flow rates were much lower. These reduced flow rates not only allowed for higher gas pressures, but also the use of heavier stopping gases, such as nitrogen or argon. Both of these scenarios lead to higher stopping efficiencies, but also to slower extraction times. Incorporating electric fields to facilitate faster transport times was proposed and studied and will be discussed later [22].

Two distinct laser ion guides have been used for laser ionization studies: one at the University of Leuven and the other at the University of Jyväskylä. In LISOL's ion guide, the volume of the gas cell was divided into two parts–the main cell and a small channel leading to the exit hole. The exit hole for this system was, as previously mentioned, 0.5 mm which resulted in the poorer extraction times of ∼480 ms for the whole guide and ∼18 ms for the extraction channel [22]. The laser ion guide constructed by Jyväskylä, however, was a modified HIGISOL system. This modified system was optimized for efficient gas flow transport and included capabilities for both water cooling and chamber baking. The Jyväskylä design was also made more modular to facilitate the installation of filaments and/or dc electrodes. The evacuation time for the necessary 0.5 mm exit nozzle was 2.25 s, which is much longer than the ∼500 ms extraction time of the LISOL system and only 390 ms for the standard 1.2 mm exit hole [26].

Highly-efficient ionization for these systems was achieved; however, similar to the other IGISOL chambers and systems, it was noted that the plasma created by the thermalization process still played an important role in the survival of the ions. It was also noted that the gas impurities still impacted the production and survival of the singular ions of interest [22]. After the ion guide technique was proven effective by low-energy facilities, ways to implement such techniques in high-energy facilities were explored.

17

Chapter 2

The NSCL Projectile Fragmentation Facility and Low-Energy Experiments

The NSCL is a projectile fragmentation facility that employs two coupled cyclotrons to produce a variety of rare ion beams over a broad energy range for nuclear physics experiments. Projectile fragmentation creates ion beams with energies on the order of 100 MeV per nucleon (MeV/u). While suitable for high-energy experiments, these beams must be dramatically reduced in energy by an intermediate process, known as beam thermalization, to energies of ∼50 keV for low-energy precision experiments or reaccelerated as a very low emittance beam for certain astrophysical experiments.

Low-energy and reaccelerated experiments housed at the NSCL include the Low-Energy Beam and Ion Trap (LEBIT) facility [29], the BEam COoling and LAser spectroscopy (BECOLA) facility [30], and the ReAccelerator facility (ReA) [31]. The NSCL's large volume linear gas cell plays a central role in the beam thermalization process which ultimately allows this projectile fragmentation facility to carry out these low-energy projects.

2.1 Isotope Production

As previously discussed in Chapter 1, the projectile fragmentation method is a chemically insensitive technique not generally limited by the properties and lifetimes of the nuclides
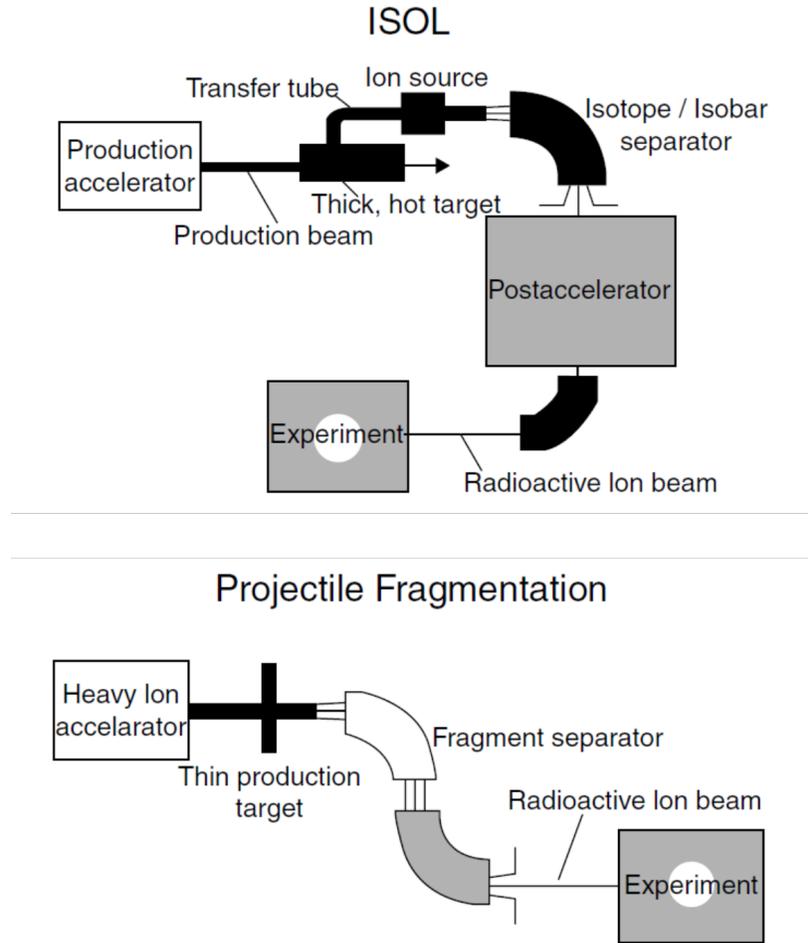
Figure 2.1: Schematic views of the ISOL and projectile fragmentation methods used to produce radioactive isotope beams [32].

produced. The complementary ISOL method has chemical dependencies to the diffusion of products formed by the interaction of high-energy, light-ion beam deep inside a thick target. Projectile fragmentation avoids this problem as the high-energy, heavy-ion beam interacts in a thin target, and products are then collected in-flight. Peripheral interactions between the projectile nuclei and the target nuclei allow some nucleons from the projectile nuclei to be randomly removed. These residues then undergo a small recoil and are focused forward and out of the target by the large initial velocity of the projectile beam [33]. A schematic representation of these two methods is shown in Fig. 2.1 [32].

The NSCL utilizes two cyclotrons in series to accerlerate heavy-ions. Cyclotrons rely on the fact that charged particles move in a circular orbit when placed in a sufficiantly large and uniform magnetic field. The force causing the ions to spiral is known as the Lorentz force, and the acceleration in each revolution is tuned so that the frequency of the circular motion of the particle is constant. The Lorentz force is described by the equation [32]:

$$F_{Lorentz} = B \times qv, \tag{2.1}$$

where B is the (vector) magnetic field, q is the charge of the particle, and v is the (vector) velocity. Since the cross product follows the "right-hand rule," the Lorentz force is perpendicular to the ion motion. The radius of the ion motion, r, is found by setting this force equal to the centripetal acceleration [32]:

$$F_{Lorentz} = Bqv = \frac{mv^2}{r}, \tag{2.2}$$

and solving for r:

$$r = \frac{mv}{Bq}. \tag{2.3}$$

The cyclotron resonance frequency, t_{cyc}, or the time that it takes a particle to complete one orbit, is the circumference of the particle's path divided by the velocity of the particle [32]:

$$t_{cyc} = \frac{2\pi r}{v} = \frac{2\pi mv}{Bqv} = \frac{2\pi m}{Bq}, \tag{2.4}$$

which, after substituting for r, is ultimately solely dependent on the mass and charge of the particle as well as the applied magnetic field and independent of the ion's velocity. This

property of the cyclotron frequency is also the basis for precise mass measurements that will be discussed in Section 2.3.1.

As the velocity of the particle increases, the orbital radii will increase, and the particles will appear to spiral out from the center of the cyclotron. The particles, however, can only spiral out so far. The maximum orbital radius and particle velocity is, therefore, limited by the maximum physical radius, ρ_{max}, and the magnetic field of the cyclotron. As a result, most cyclotrons are identified by their K value which is given in MeV and calculated as $(B\rho_{max})^2/2$. For greater detail of the operating principles of cyclotrons, please see [32] and references therein.

The two cyclotrons at the NCSL are a K-500 and a K-1200. By coupling the beam from one machine into the other, stable ion beams can reach velocities of about half the speed of light with beam energies on the order of $\sim$150 MeV/u. These stable ion beams then impinge on a beryllium foil, and the projectile fragments formed by the nuclear reactions are separated "in-flight" and focused by the A1900 fragment separator [34] for delivery to the experimental areas of the laboratory. The beam thermalization area shown in Fig. 2.2 serves as the bridge from the high-energy experimental areas of the lab to the low-energy experimental areas of the lab. Without this bridge, low-energy precision experiments and certain astrophyisical studies would be limited to ISOL production methods and facilities. A gas catcher designed for energetic particles, whose principles are discussed below, is pivotal to the successful operation of the thermalization area.
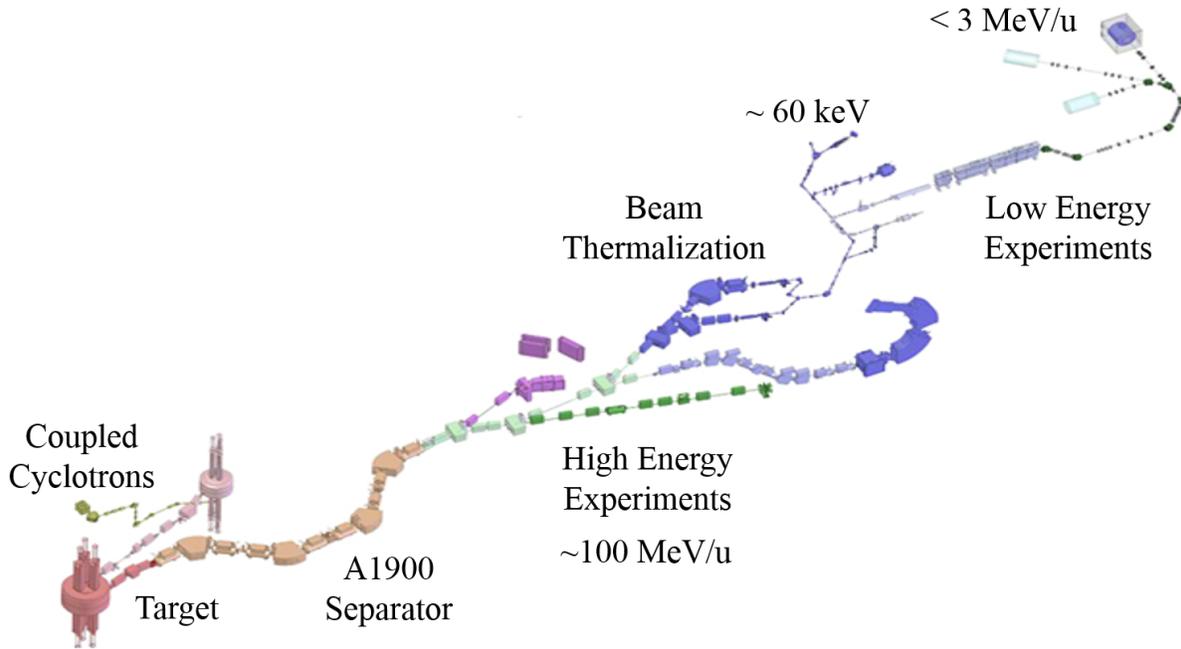
Figure 2.2: Schematic overview of the NSCL–a projectile fragmentation facility that incorporates coupled cyclotrons to accelerate the heavy beam.

2.2 Gas Catchers for Energetic Fragments

Given the success of the IGISOL method for thermalizing and transporting lower-energy reaction products at ISOL facilities, several laboratories began investigating the feasibility of implementing ion guide techniques to collect the more energetic reaction products produced at projectile fragmentation facilities. The advantage of projectile fragmentation facilities to ISOL facilities is that in-flight production is not sensitive to the chemical properties or the lifetimes of the nuclides of interest [35]. A major disadvantage of projectile fragmentation facilities is the higer-energy beams and fragments, which have higher emittances and are harder to control and focus. There is also a separation between production and thermalization in projectile fragmentation which is both an advantage and disadvantage. The significance of these conditions is shown in Fig. 2.3 [6], which compares the predicted LISE++ [6] produc-
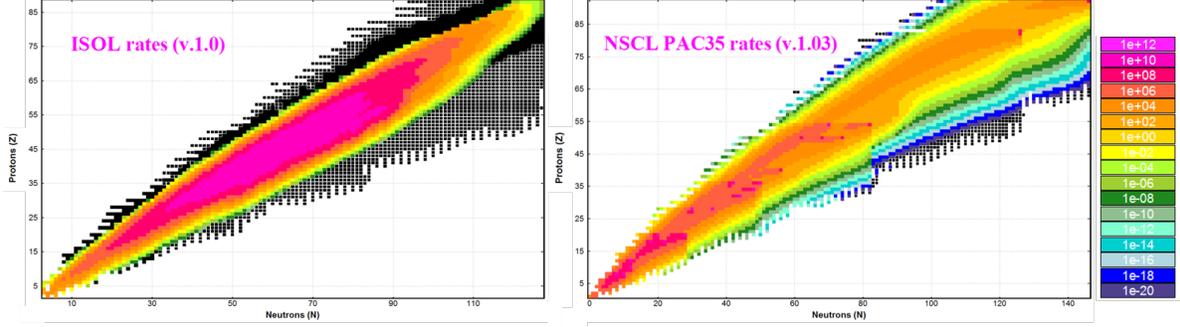
Figure 2.3: Predicted LISE++ production rates plotted on a nuclear chart for both an ISOL facility (left) and for the NSCL projectiile fragmentation facility (right) [6].

tion rates for both an ISOL facility and the NSCL projectile gragmentation facility.

The same general features exist in higher-energy ion guide systems that existed in IGISOL set-ups, and the principles established through IGISOL research still hold true–the repulsive effects of space charge, the distortion of any electric fields by the plasma effect, and the interaction of an ion of interest with buffer gas impurities all contribute to efficiency losses within the system [22].

2.2.1   Components of PF-Gas Catchers

Similar to their low-energy counterparts, medium and high-energy gas catchers contain a buffer gas-filled chamber, exit nozzle, skimmer or SPIG, and a differential pumping system. These higher energy set-ups, however, also generally include a degrader and wedge system located upstream of the gas cell to produce a monoenergetic beam and as well as to remove nearly all of the kinetic energy of the beam prior to gas stopping. The gas cells also contain larger stopping volumes and higher buffer gas presures, which necessitate electrode structures to generate DC and/or AC fields for fast ion extraction.

Initial beam energies range from ∼1 MeV/u to ∼1000 MeV/u, with energy spreads up to a few percent. The higher-energy beams require a degrader(s) to reduce the kinetic energy

Monoenergetic Wedge Degrader

Higher Energy Portion of Beam

Lower Energy Portion of Beam
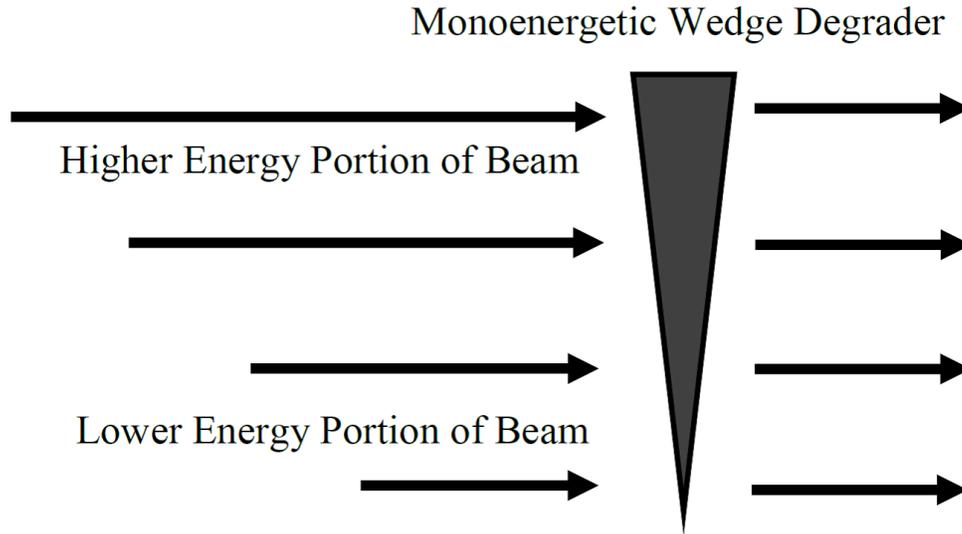
Figure 2.4: Simple cartoon depicting the working principle of a monoenergetic wedge.

of the incoming product beam down to ~1 MeV/u to allow for a manageable gas volume. The energy spread of the beam also needs to be compensated. This compensation is accomplished by dispersing the beam on a monoenergetic wedge [35]. A schematic depiction of a monoeregetic wedge is shown in Fig. 2.4. Various facilities employ different degrader/wedge arrangements, which are discussed in section 2.2.2.

Higher beam energies also warrant larger gas stopping volumes. Conventional IGISOL gas chambers were only a few cm in length. As discussed earlier, reaction products were stopped in these small volumes and simply transported out of the cell by gas flow. Higher energy gas cells, however, have ranged from 30 cm to 200 cm in length. The larger volumes have a significant impact on extraction times. Relying solely on gas flow, extraction times on the order of minutes are expected with significant losses occuring from not only radioactive decay but also charge exchange reactions and diffusion as discussed in section 1.2.2 [35]. Numerous ion-transport methods utilizing electric fields and respective electrode structures

Laboratory	Isotope Separator RI-Beam Energy	Gas Pressure Cell Size	Guiding Force out of Gas
RIKEN/Japan	RIPS ~100 MeV/u	~130 mbar 40 cm x 200 cm	DC + RF Funnel, DC + RF Carpet
GSI/Germany	FRS 100–1000 MeV/u	0.5–1 bar 20 cm x 125 cm	DC + RF Funnel
NSCL/US	A1900 ~100 MeV/u	<5 bar 5 cm x 50 cm	DC + Gas Flow
ANL/US	GARIS ~5 MeV/u	~150 mbar 10 cm x 20 cm	DC + RF Funnel + Gas Flow
GSI/Germany	SHIP ~ 5 MeV/u	~0.1 bar 17 cm x 18 cm	DC + RF Funnel + Gas Flow
CYRIC/Japan	n-fission + IGISOL ~1 MeV/u	~100 mbar 24 cm x 30 cm	DC + Gas Flow

Table 2.1: Summary of the first large gas cells developed for energetic radioactive ion (RI) beams [35].

have been explored in order to improve the transport times inside large volume cells. These methods are discussed in detail below.

2.2.2 In-Gas Ion-Transport Methods

Several medium and high-energy accelerator laboratories constructed and tested their own gas catchers, and a summary of these initial gas cells can be found in Table 2.1 [35]. The medium energy catchers will not be discussed here, and the focus will solely be placed on high-energy facilities (beam energy $\geq$ 100 MeV/u) and their respective catchers with the understanding that the same principles and techniques were employed for both energy ranges.

Given the sheer volume of these higher-energy cells, the extraction times of the ions would be dominated by the drift time to the nozzle without the help of DC electric fields. The velocity of an ion in gas is directly related to the applied DC field and can be calculated using the equation [36]:

$$v_d = K \cdot E \cdot \frac{P \cdot T_0}{P_0 \cdot T} \tag{2.5}$$

where v_d is the drift velocity (cm/s), K is the ion mobility (cm^2/V·s), E is the electric field (V/cm), P is the operating pressure (mbar), T_0 is the standard temperature (273 K), P_0 is the standard pressure (1000 mbar), and T is the operating temperature (K). Once the ion motion is damped by the gas, the ions' trajectories follow the electric field lines produced by the applied DC voltage. Therefore, the electric field applied to the cell not only dictates the ion motion but more importantly the ion velocity in the gas. Since the electric field terminates at the end wall of the cell, it is necessary to employ gas flow to ensure ions exit through the nozzle.

Inside the gas cell, a dynamic (RF) field can be applied to repel the ions from the wall and generally guide them toward the small exit hole. Wada [35] expressed the repelling force as:

$$F_{avg} = m \left(\mu_o \frac{\rho_o}{\rho} \right)^2 \frac{V_{RF}^2}{r_o^3}, \tag{2.6}$$

where m is the mass of the ion, μ_o is the reduced ion mobility, ρ_o is the normal gas density, ρ is the gas density, V_{RF} is the zero-to-peak voltage for the RF amplitude, and r_o is half of the spacing between the electrodes.

This average repelling force exerted on charged particles decreases as the distance from the electrode structure increases and also decreases in the presence of buffer gas and can also be described by the following equation [35, 36]:

$$\overline{F_{vac}} = -\frac{e^2}{2mw^2} \overline{\left[E \frac{dE}{dx} \right]}, \tag{2.7}$$

where $\overline{F_{vac}}$ is the average force exerted on charged particles by the inhomogeneous RF field, e is the fundamental charge of an electron, m is the mass of the ion, w is the angular frequency of the RF field, and E is the amplitude of the RF field. In the presence of gas, it is reduced

to the form [36]:

$$\overline{F_{damp}} = \overline{F_{vac}} \cdot \frac{1}{1 + (\frac{e}{Kmw})^2}.$$ (2.8)

Since K is the ion mobility in gas, the force scales with the RF amplitude squared over the pressure squared. The repelling force experienced by an ion is also approximately proportional to the square of the mass. Given the ions of interest are much more massive than the buffer gas ions, one expects the heavier ions to move toward the nozzle while the lighter ions diffuse to the electrode surface and are neutralized. Also considering the repelling force provided by an RF field is inversely proportional to the square of the gas pressure, the maximum pressure of the gas cell is limited by the desired strenth of the RF field[35]. Two main ion transport methods will be discussed– static field and gas flow only [37] and DC, RF, and gas flow [35].

The first generation gas cell at the NSCL was 50 cm in length and generally operated under a helium pressure of 1 bar (750 torr). A schematic of the experimental test set-up is shown in Fig. 2.5 [37]. The kinetic energy as well as the momentum spread of the beam was reduced upstream of the cell by a 1.49-mm thick rotatable borosilicate glass degrader, a 0.74 mm aluminum monoenergetic wedge, and a 1-mm thick beryllium window such that the ions would range-out in the gas [37].

A set of 21 ring electrodes and 4 concentric spherical electrodes provided a DC gradient along the gas cell cylindrical axis to guide and to focus the stopped ions toward the exit hole. From there, the ions were jetted through a supersonic nozzle and into an expansion chamber. The ions were then either collected and measured or caught and delivered to low-energy experiments by an RF ion-guide system [37]. The extraction efficiency of the first generation cell was a few percent.
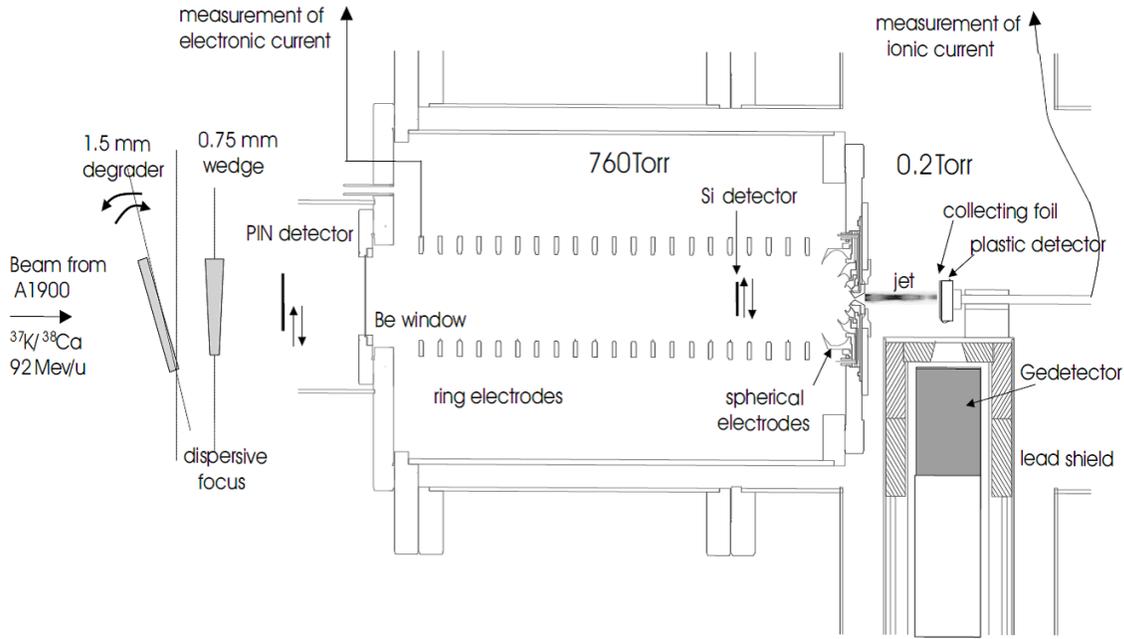
Figure 2.5: Schematic of experimental set-up for testing the first generation gas cell at NSCL [37].

This efficiency dramatically decreased with an increase in the implantation rate; similar to the effects reported in IGISOL systems. It was also noted that although the extraction efficiency curve as a function of degrader thickness approximately followed the stopping efficiency curve, the maximum yields were much lower than those calculated for the stopping efficiency. The same space charge and plasma effects reported in the low-energy ion guides were expected to be present in the nozzle region of this high-energy gas cell and was attributed to these significant losses [37]. Further discussion of these results will be given after examining the RF based gas systems and properties.

The idea behind implementing both a static DC field and a dynamic RF field was that the DC potential would drag the ions through the gas, while the average force due to the RF gradient field would drive the ions away from the electrodes along the wall and focus the
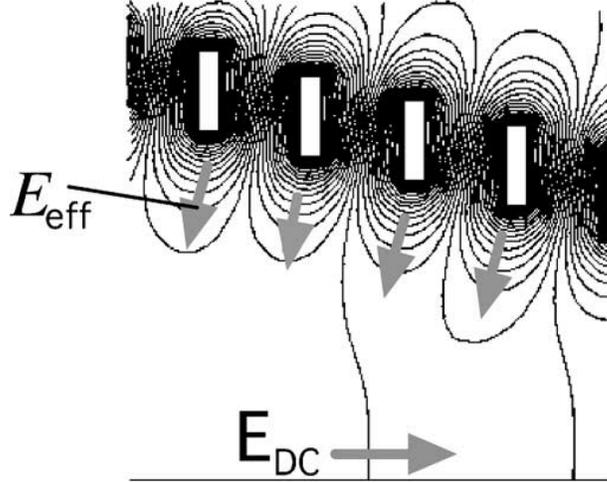
Figure 2.6: A series of ring electrodes rotationally symmetric to the lower line provide an RF-barrier field (E_{eff}) as well as a superimposed DC field (E_{DC}). The ions are pulled by E_{DC} while E_{eff} drives them away from the electrodes [35].

ions toward the exit. This concept is depicted in Fig. 2.6 [35]. The first RF-based gas cell was constructed at RIKEN and was used off-line to test the working principles of the RF funnel inside a gas cell. This first generation RIKEN gas cell was 30 cm in length and was kept at a helium pressure of 20 torr. The funnel, as pictured in Fig. 2.7, contained 80 ring electrodes with both an RF voltage and decreasing DC offset applied to each electrode. A transmission of ∼70% was obtained for the funnel [35].

The next iteration of the RF gas catcher was tested on-line and dubbed the POP, or proof-of-principle, system. This gas cell was 70 cm in length and the helium pressure was tested at both 30 and 60 torr. Here, a double RF funnel structure was employed. The two funnels were built of flexible printed circuit boards and stacked to transport ions the entire length of the cell. The efficiency for the POP system was reported as 0.43% stopping efficiency with a 2.4% ion-guide efficiency. Helium gas pressures, as well as the geometry of the gas cell, limited the stopping efficiency, while the RF voltage limited the ion-guide efficiency [35].
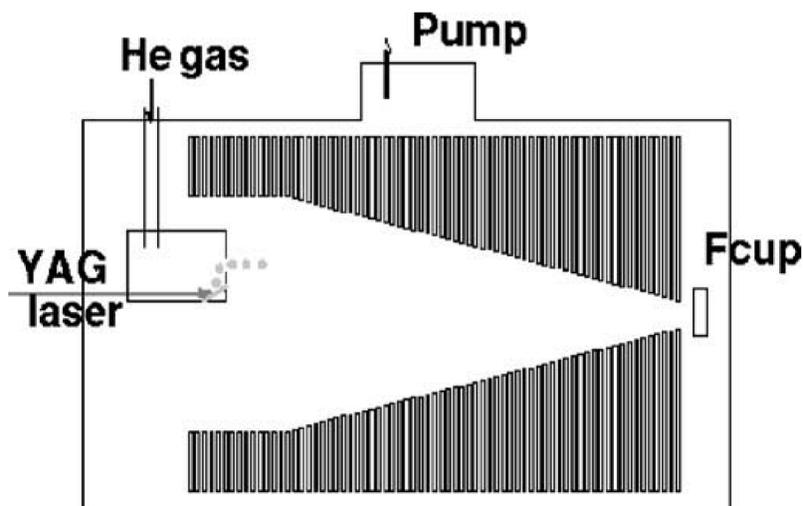
Figure 2.7: Off-line RF funnel experimental set-up for transporting Ta$^+$ ions [35].

Based on the experience with both of these RF test cells, a third RF gas catcher was constructed at RIKEN. It was 2 m in length and was operated at a helium pressure of 100 torr. New RF electrodes were constructed to alleviate large capacities and high heat dissipation that was experienced in the POP system. These electrodes consisted of two layers of planar printed circuit boards (PCB). The top PCB had a diameter of 29 cm with 280 ring electrodes and a central hole of 10 mm. The bottom PCB had a diameter of 3 cm with 48 ring electrodes and an exit nozzle of 0.6 mm. These structures were named RF-carpets and are shown in Fig. 2.8 [35]. The top layer was operated with only a static push field while the bottom layer was operated with both RF and DC fields. A DC drift was applied perpendicular to the carpets along the length of the cell while the RF-carpets were located at the exit, and a maximum overall efficiency of 0.2% was reported for the lowest beam intensity tested.

As seen with all of the previous gas cells, the efficiency of this cell decreased with increasing beam intensity [35]. These results, as well as the results from the NSCL and other gas
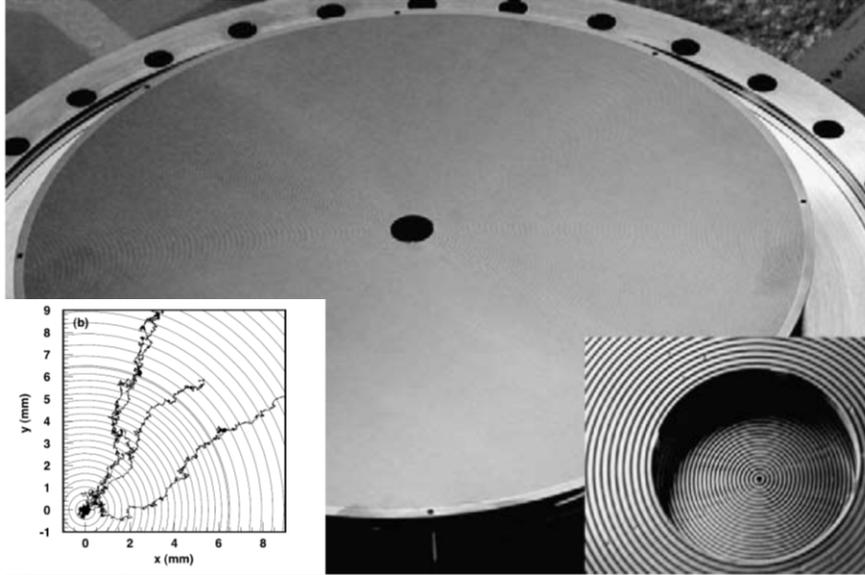
Figure 2.8:   The RF-carpet electrode employed by RIKEN in the RF based gas cell was made of two layers of PCBs. Details of these layers can be found in the text (b) Typical ion trajectories determined by a microscopic particle simulation for ^{8}Li ions in 90 torr helium gas where the RF voltage between neighboring electrodes was 190V at 26 MHz. The superimposed DC field was 8 V/cm [35].

catcher facilities were combined in an overall analysis of the impact of beam intensity on efficiency. A summary of the "world data" is shown in Fig. 2.9 [38]. It is clear that efforts were still needed to improve the extraction efficiency trend observed for all operational gas cells. Since the greatest extraction losses were attributed to space charge and plasma build-up, most of the experimental efforts were focused on reducing these effects in next generation devices. One such device, the focus of the next chapter, is essential to the low-energy and reaccelerated facilities located at the NSCL.

2.3   Low-Energy and ReA Facilities

Low-energy, so-called precision techniques and experiments, as previously mentioned, were initially developed at ISOL facilities. The low-energy secondary beams produced by the ISOL
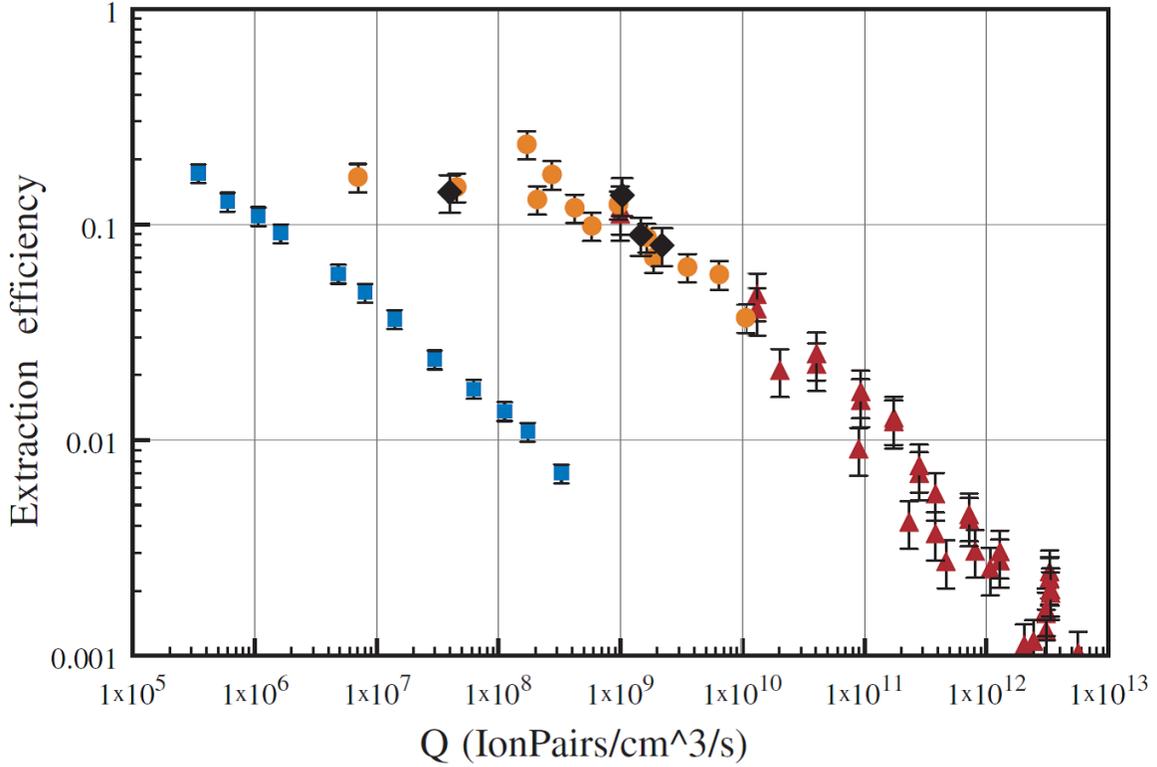
Figure 2.9: Summary of the decrease in extraction efficiency for a variety of gas cell systems as a function of the ionization-rate density. The data were obtained for ^{8}Li, ^{38}Ca, ^{107}Ag, and ^{58}Ni from the projectile fragmentation facilities at RIKEN (squares), MSU/NSCL (circles), and GSI (diamonds), as well as the ISOL facility at Leuven (triangles), respectively [38].

method were simply matched to the needs of the techniques as compared to the high-energy secondary beams produced by projectile fragmentation. The development of gas catchers and beam thermalization made these low-energy techniques available to projectile fragmentation facilities and provide a wider range of exotic isotopes. The beam thermalization area at the NSCL provides beams for the LEBIT [29], BECOLA [30], and ReA [31] facilities.

2.3.1   LEBIT

The Low-Energy Beam and Ion Trap facility (LEBIT) at the NSCL performs Penning-trap mass spectrometry on rare isotopes [29]. Ion traps are used in a variety of research as a means to confine, or trap, ions in small volumes in well-controlled fields. These devices can
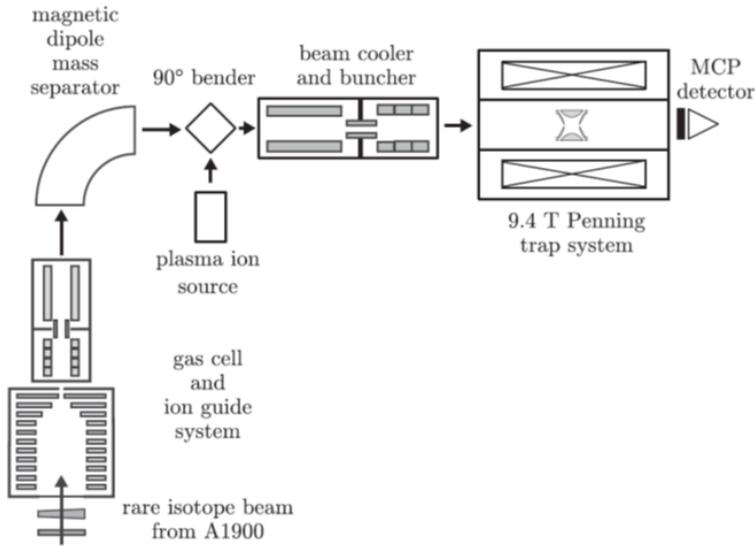
Figure 2.10: (Left) A schematic overview of the LEBIT facility. (Right) The LEBIT high-precision Penning trap with its end-cap removed. A bottle cap is shown with the trap for scale [41].

be very sensitive, and in experiments where the frequencies of revolution are measured, high precision can be achieved by trapping the ions for extended amounts of time. Penning ion traps confine ions with a strong static magnetic field combined with a weak static electric field. If the charge state of the ion and the strength of the magnetic field are known, the mass of the ion can be inferred from the ion's resonant cyclotron frequency (2.4). This frequency can be determined by monitoring an induced current on the trap electrodes or through time of flight measurements for ions leaving the Penning trap. The mass resolving power of Penning traps is directly proportional to the observation time of the ion motion. The longer the motion can be observed, the higher the resolving power of the trap [39]. Precise mass measurements are important fundamental features of nuclear structure and provide input for nuclear astrophysics and fundamental interactions [40].

Low-energy beams emerge from the NSCL large volume linear gas cell at a continuous rate and are cooled and bunched upon entering the LEBIT facility for batch mode mass

measurements. The bunched beam is then injected into and trapped by the LEBIT Penning trap. Ions are excited by known frequencies, and the time of flight of the excited ions are measured for each frequency. These time of flight measurements show a resonance when the ion frequency matches the excitation frequency. The excitation frequency can be used to calculate the mass of the ion. A schematic view of this facility as well as the LEBIT high-precision Penning trap is shown in Fig. 2.10 [42].

The LEBIT facility was the first to perform precision Penning trap mass measurements on rare isotopes produced by the projectile fragmentation [29]. Since its commissioning, LEBIT has determined the mass of many exotic nuclei over a broad range of atomic numbers and half-lives all with a relative precisions on the order of 10^{-8} atomic mass units (amu), or 1 keV in mc^2 [40, 42, 41, 43, 44, and references therein].

2.3.2 BECOLA

The BEam COoling and LAser spectroscopy facility (BECOLA) located at the NSCL can perform both laser-hyperfine-structure measurements and atomic/nuclear spin manipulations on exotic ions [30]. These studies use collinear laser spectroscopy (CLS), optical pumping, and nuclear-magnetic resonance (NMR) techniques. Laser-spectroscopy techniques can determine fundamental properties of nuclei such as the magnetic dipole moment, the electric quadrupole moment, the nuclear spin, and the mean-square charge radius.

Similar to the LEBIT facility, the continuous low-energy beams from the NSCL large volume linear gas cell are cooled and bunched for the BECOLA measurements. A laser beam is then directed collinearly with the bunched ion beam. Since the ion beam produced from the large volume gas cell is typically singly charged, a charge-exchange cell (CEC) is utilized for experiments that require neutral beams. For hyperfine measurements, the laser
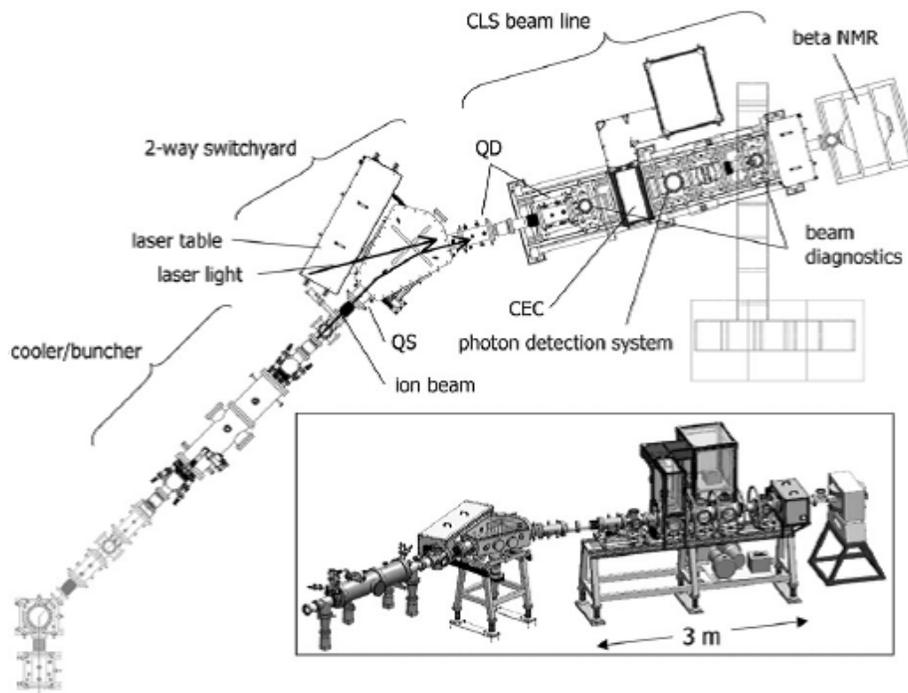
Figure 2.11: A schematic overview of the BECOLA facility with a three-dimensional model shown in the inlet. QS and QD indicate quadrupole singlet or doublet electrostatic focusing elements, respectively [30].

frequency is tuned into resonance with the hyperfine transition of interest, and the resonant fluorescent light is collected and analyzed. For beta-NMR measurements, the bunched ion beam is polarized using an optical pumping technique in conjuction with circularly polarized laser light before entering the beta-NMR device where the beta-decay of the exotic ions are analyzed [30]. A schematic view of this facility is shown in Fig. 2.11 [30]. The BECOLA facility was recently commissioned on-line using ^{36}K and ^{37}K radioactive ion beams from the NSCL's large volume linear gas cell [45].

2.3.3 ReA

The ReAccelerator facility (ReA) located at the NSCL is a post-accelerator designed to reaccelerate rare, thermalized isotopes up to energies of a few MeV/u with excellent emittances.
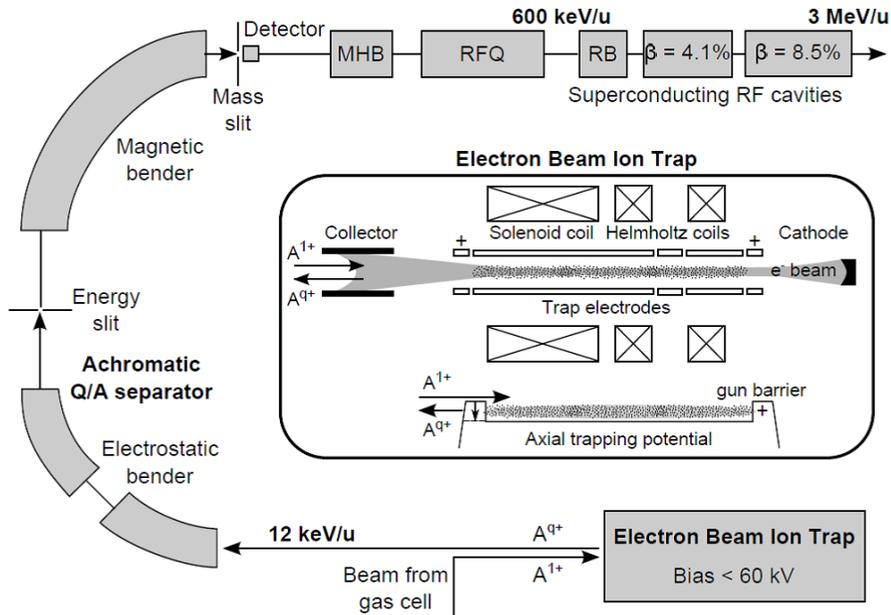
Figure 2.12: A schematic overview of the ReA facility located at the NSCL [46].

For nuclear reaction studies, Coulomb excitation, nucleon capture, and fusion reaction experiments can be conducted in this energy range. Very recently, a beam cooler and buncher was added just upstream of the ReA facility to better match the beam from the large volume linear gas cell into the charge breeder.

After entering ReA, the ions, typically in the 1+ charge state, must be charge bred into highly ionized states by the facility's Electron-Beam Ion Trap (EBIT) for efficient acceleration. In order for a specific charge state to be used, pulses of the highly charged ions are ejected from the EBIT and sent through a charge-over-mass (Q/A) separator. The selected ions are then injected into a radio-frequency quadrupole accelerator (RFQ) and finally into a superconducting radio-frequency linear accelerator (SRF-LINAC) for reacceleration. The ReA facility was commissioned using a stable ^{39}K beam, and later with ^{46}Ar, ^{46}K, and ^{37}K ions. ReA was the first reacceleration facility to successfully accelerate ions produced by the projectile fragmentation method.

The present ReA facility (ReA3), schematically depicted in Fig. 2.12, contains 15 reaccelerator cavities and can accelerate ions with Q/A of 0.2–0.5 to energies of 0.3–6.0 MeV/u, respectively. The proposed configuration of the full facility (ReA12), though, will contain thirty-nine linear reaccelerator cavities and will be capable of providing beams from 0.3 to 12 MeV/u for heavy ions and up to 20 MeV/u for light ions [31]. The ReA facility enables a variety of nuclear structure and astrophysical experimental projects using equipment that includes the Array for Nuclear Astrophysics Studies with Exotic Nuclei (ANASEN) [47], the Active Target-Time Projection Chamber (AT-TPC) [48], the Summing NaI(Tl) (SuN) detector [49], and the Jet Experiments in Nuclear Structure and Astrophysics (JENSA) [50]. All of these low-energy facilities and experiments conducted at the NSCL rely on successful operation of the laboratory's beam thermalization area.

Chapter 3

The NSCL Beam Thermalization Area

The first version of the NSCL beam thermalization area successfully ran from 2004-2009 and proved that precision experiments were possible at this projectile fragmentation facility [1, 44, 51, and references therein]. Over the next four years, the beam thermalization area was completely rebuilt, upgraded, and finally recommissioned in 2013. Upgrades to the area included adding two new high-resolution, momentum compression beam lines and a new large volume linear gas cell constructed by ANL [2].

Since its installation, numerous radioactive isotope beams at a variety of incoming beam rates have been thermalized and extracted from the NSCL's large volume linear gas cell. The present work will concentrate on the commissioing results obtained with ^{76}Ga and the characterization results obtained with numerous other incoming rates and ions. Results from these experiments were used to establish the stopping process and the extraction efficiency of the gas cell as a function of the ionization-rate density, Q. The behavior of the NSCL's large volume linear gas cell is generally consistent with previous systems, however, the efficiencies from this gas cell are shown to be higher at large Q values.

3.1 Area Overview

The beam thermalization area at the NSCL receives high-energy projectile fragment beams from the A1900 separator [34] and reduces the beam energies from $\sim$100 MeV/u down to

thermal energies of ≤ 1 eV [2]. This area contains two analysis beam lines, but the current experiments were carried out using the so-called north line. The high-energy beamline located on the north side of the beam thermalization area was designed to disperse the fragment beam in momentum onto a monoenergetic wedge [35] and then to reshape and focus the beam into the large volume linear gas cell.

During this process, the high-energy beams are passed through solid degraders and the monoenergetic wedge to reduce the bulk of the beam's kinetic energy down to ~ 1 MeV/u and to reduce the energy spread of the beam, respectively. Ions then pass into the large volume linear gas cell where they are thermalized through collisions with ultra-pure helium buffer gas [2]. The thermalized ions, which retain either a 1+ or 2+ charge state due to the high ionization potential of the helium buffer gas, are guided and concentrated towards a supersonic nozzle with a static DC potenital, dynamic RF potential, and gas flow where they are then jetted out of the cell and into a differentially pumped RFQ ion-guide [52]. Once through the ion-guide, the ions are accelerated to ~ 30 keV/q, mass analyzed, and sent to the low-energy experimental areas of the laboratory. A schematic of the beam thermalization area is shown in Fig. 3.1 [2].

3.2   NSCL's Large Volume Linear Gas Cell

The beam thermalization area centers around the gas cell. In 2012, the NSCL obtained a large volume linear gas cell from ANL as part of the research and development for the Facility of Rare Isotopes Beams (FRIB), a next generation RIB facility. This gas cell replaced the first generation NSCL gas cell, discussed in Section 2.2, that was 50 cm in length and operated at 1 bar (750 torr) helium. The NSCL's large volume linear gas cell is 1.2 meters in length
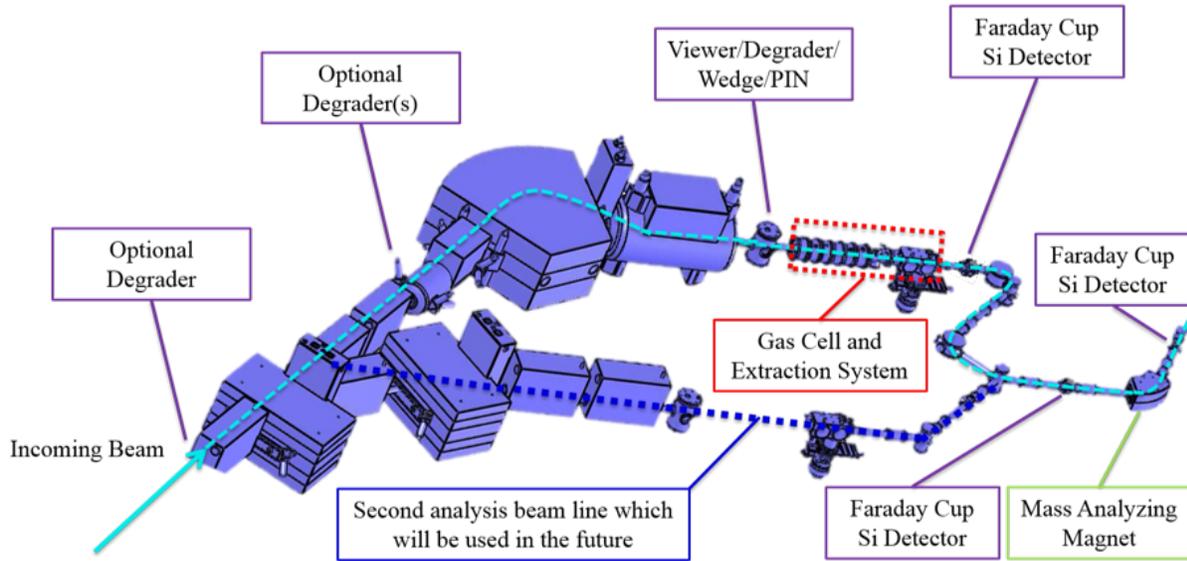
Figure 3.1: A schematic overview of the beam thermalization area located at the NSCL including optional degrader and detector positions.

with a 25 cm diameter and is operated at $\sim$100 mbar ($\sim$75 torr) [53]. The larger stopping volume and wider cell width allows for the capture of ions with substantial range straggling as well as provides a larger volume to mitigate the space charge. Larger beam dimensions allow the ionization to be distributed within the gas and, in theory, reduce the losses from space charge and plasma effects discussed in Section 1.2.2.

In addition to the sheer size of the gas catcher, the NSCL's large volume linear gas cell utilizes an enhanced ion-transport method, shown in Fig. 3.2 [36], that consists of a DC drag field throughout the volume of the cell, an RF cone and gas flow at the extraction region, and an additional RF potential applied to the electrodes along the walls of the cell. This additional RF potential was implemented to keep the fragment ions of interest from diffusing to the chamber walls as they are pushed outward by any space charge potential. The final modification made when compared to the first generation design was the inclusion of an elaborate RF electrode stucture along the walls that was incorporated to reduce the build
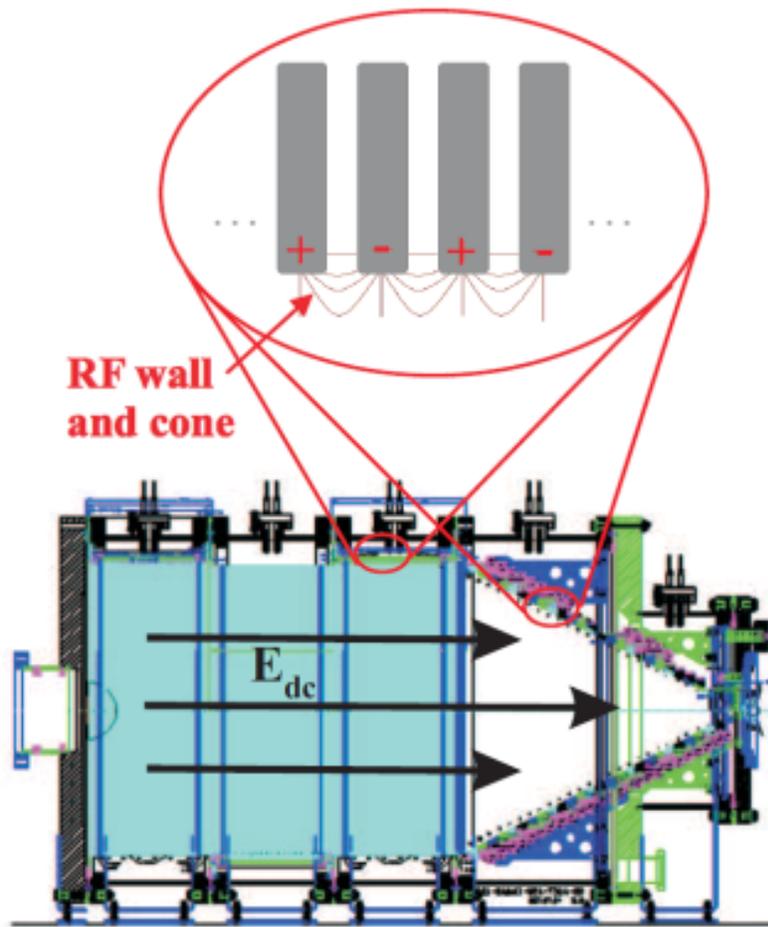
Figure 3.2: Schematic depicting the various electromagnetic fields implemented to increase and improve the extraction times and overall extraction efficiencies for the NSCL's large volume linear gas cell. Arrows show the direction that the ions are dragged by the DC electric field while the focusing potential created by the RF field is shown in detail at the top of the figure [36].

up of the space charge potential by providing large surfaces to collect the ionized buffer gas.

Remember that the RF repelling potential is weak for low mass ions such as helium.

As discussed in the previous chapter, high energy gas catchers employ electromagnetic fields to overcome the slower evacuation times associated with the larger stopping volumes. Although the gas evacuation time is still on the order of tens of minutes, well designed systems can achieve ion extraction times on the order of tens of milliseconds [36]. The

NSCL's large volume linear gas cell has an applied DC potential to drag the ions the entire length of the cell and toward the extraction region, millimeters from the nozzle. Ions in this region of the gas cell are then propelled by gas flow through a supersonic nozzle and into the RFQ ion guide. The gas cell was typically operated with a drift field of 7.5 V/cm, a pressure of 123 mbar of helium, and a temperature of 269 K for the commissioning experiments. By using Eq.(2.5), the drift velocity of the ^{76}Ga$^+$ ions in the gas cell under thes conditions was $\sim$19 m/s.

In order to sustain the concentration of field lines at the nozzle, a stronger field gradient is required in the extraction region. The field strength in any one area of the cell, though, is limited by electrical discharges that can occur within the gas, as given by the Paschen curve for the helium buffer gas. Since the field strength applied to the nozzle region is the most limited, the strength of the applied field in the rest of the gas cell is also limited. However, given that the electric field strength is directly proportional to the ions' velocities and thereby their extraction times, the DC gradient is kept as high as possible to not only drag the ions of interest quickly and efficiently through the gas but to also remove the ions responsible for the build up of space charge [36].

As discussed in Chapter 1, the buildup of space charge occurs when the cations created by the fast ions are not removed quickly from the gas cell. Each incoming ion creates about 10^5 He$^+$/e$^-$ pairs. The electrons are rapidly removed due to their low mass and high velocity by the electric field, while the much heavier helium buffer gas ions must drift along with the ions of interest. The space charge potential is therefore strongest along the center of the beam axis. An example of this stronger build-up along the center of the beam axis is shown in Fig. 3.3 [36]. In this example, it was assumed that the full range of the Bragg peak for the particles fell within the gas cell; however, as will be discussed with the NSCL's large volume
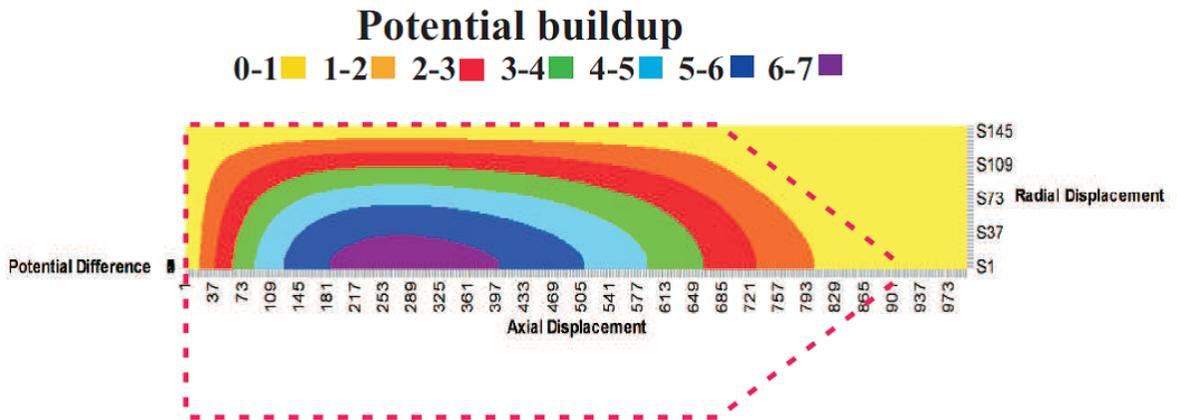
Figure 3.3: A self-consistent calculation to show the potential buildup for 60 million ions entering into and ionizing the gas within a small gas catcher is shown. Notice that the intensity is the strongest along the center of the beam axis. The outline of this gas catcher is represented by the dashed red line [36].

linear gas cell, only part of this range falls within the catcher.

The accumulation of space charge in the center of the device shields the externally applied fields and can cause thermal ions to move towards the walls and not toward the extraction region. The so-called RF walls and an RF cone were included in other gas cells designed by ANL [54, 53] and were also included in the NSCL's large volume linear gas cell to overcome these space charge effects by providing better focusing toward the nozzle. These structures are composed of closely packed, thin electrodes with an overall repelling force created by applying opposite phases of an RF electric field to neighboring electrodes as highlighted in the inset of Fig. 3.2. Recall that the RF repelling force experienced by an ion is approximately proportional to the square of the mass, and since the ions of interest are much more massive than the buffer gas ions, the heavier ions move toward the nozzle while the lighter ions diffuse to the electrode surface and are neutralized [35, 36].

The RF cone, Fig. 3.4, is composed of 280 independent consintric rings of decreasing radius. These electrodes are 0.4 mm thick and 0.5 mm apart from each other. The cone is

43
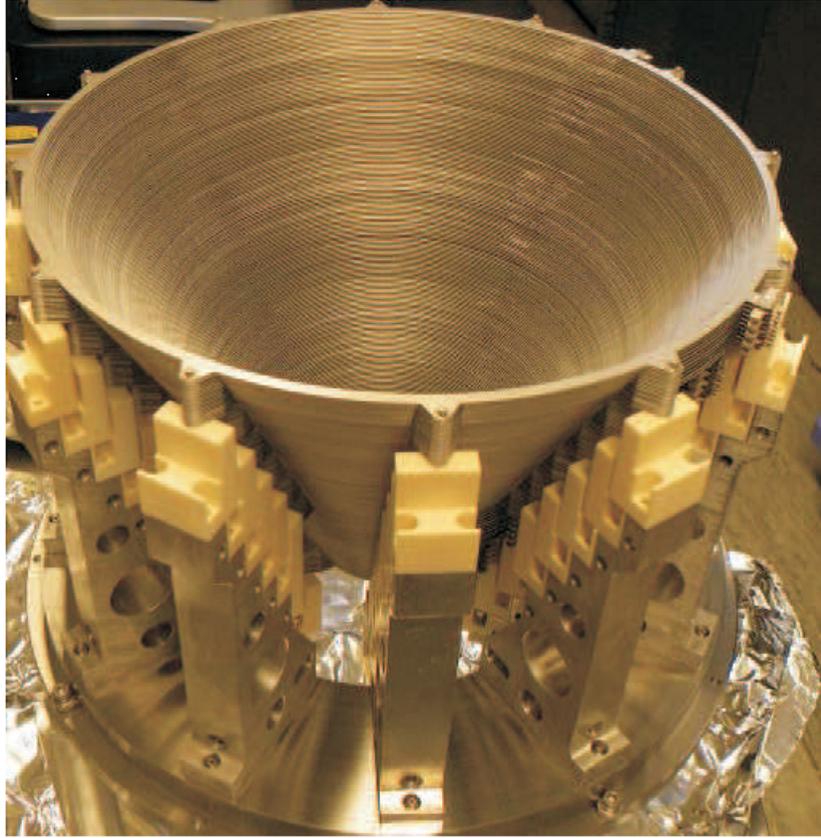
Figure 3.4: Photograph of the RF cone structure used in the NSCL's large volume linear gas cell.

designed in such a way to focus the ions directly onto the supersonic nozzle. The elctrode structure designed for the body of the NSCL's large volume linear gas cell was slightly more elaborate, as shown in Fig. 3.5. There are roughly 750 independent electrodes that are each 0.8 mm thick and separated by a 0.6 mm gap. Each electrode includes 12 spokes 30 degrees apart from one another. Every second spoke is 3.8 cm in length with the others alternating between 7.5 cm and 9.8 cm. Since the helium ions are less sensitive to the RF repelling force, the spokes along the wall were incorporated into the electrode design to shorten the distance these ions must travel before thier collection. The goal was to reduce the overall buildup of He^+ as a function of the incoming beam rate.
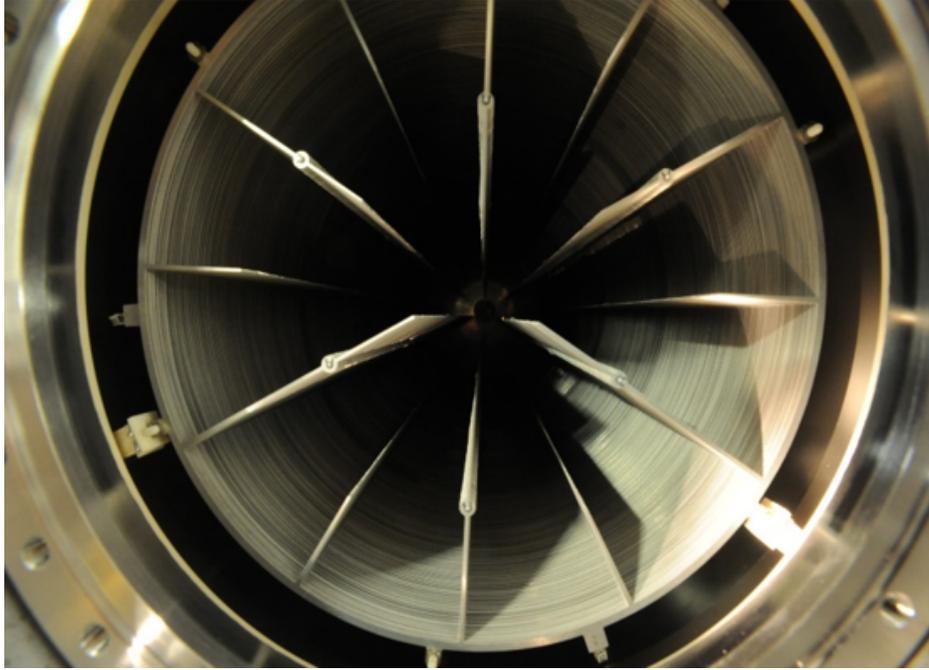
Figure 3.5: Photograph of the RF electrode structure used along the walls in the NSCL's large volume linear gas cell.

As was true with the maximum DC voltage, the maximum RF amplitude is limited by electrical discharges and breakdown voltages within the gas. Also remember that the repelling force exerted on charged particles decreases as the distance from the electrode structure increases and also decreases in the presence of a buffer gas. A higher gas pressure, therefore, leads to higher stopping efficiency, but results in a decrease in the extraction efficiency. A lower gas pressure ensures a higher transport efficiency but severely limits the stopping efficiency of energetic and/or light ions. The operating gas pressure and the applied electric field strengths are, therefore, a compromise between the maximum stopping efficiency for the fast ions and the maximum ion transport efficiency.

The DC drag field is necessary to obtain reasonable extraction times while the RF focusing field is necessary to overcome the defocusing effects associated with space charge. By extending the RF field to include not only the extraction region, but also the body of
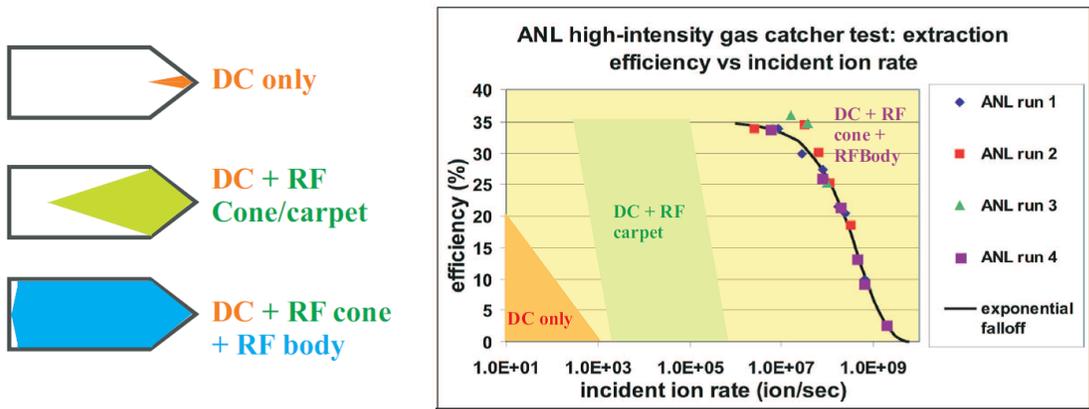
Figure 3.6: The schematics on the left show the areas of the gas cells from which radioactive ions can be extracted given the electric fields present and when operating at high intensities. The NSCL's large volume linear gas cell is represented by the lower left schematic. The graph on the right compares results for online experiments with the NSCL's large volume linear gas cell design to results obtained from gas catchers with little to no RF refocusing [36].

the cell, radioactive ions can, theoretically, be extracted from the whole cell which should increase the efficiency. ANL tested the efficienciey effects of this extended extraction region, see Fig. 3.6 [36]. As shown, the efficiency was improved for higher incoming beam rates. A unique spoke design was also incorporated into the electrode stucture of the new large volume linear gas cell which should reduce the overall space charge build up as a function of the incoming beam rate and should further increase the reported extraction efficiencies. The results from commissioning and testing with ^{76}Ga and other ions as well as a detailed discussion on the operation of the new large volume linear gas cell are contained in the next section.

3.2.1 Commissioning Experiments

The recent upgrades of the NSCL's beam thermalization area were completed by the addition of the large volume linear gas cell obtained from ANL. Several experiments were conducted

46

to commission the thermalization system that includes the beam line, the degrader system, the gas cell, and the extraction system. The experimental set-up, measurements, and results obtained from these commissioning runs will be discussed in detail below [2].

3.2.1.1   Experiment Description

For the commissioning of the large volume linear gas cell, the coupled cyclotrons produced a primary $^{82}\text{Se}^{34+}$ beam at 140 MeV/u. This high-energy beam was then impinged upon a 415 mg/cm^2 beryllium target, and a wide range of projectile fragments were produced. The primary beam current was frequently monitored at the target position by inserting a Faraday cup into the beam's path, and typical currents were 1.1(0.1) pμA for full beam. The A1900 fragment separator [34] employed a 299 mg/cm^2 aluminum achromatic wedge to separate the fragments in order to provide the beam thermalization line with a 79% pure $^{76}\text{Ga}^{31+}$ secondary beam. During separation, projectile fragments began with $B\rho = 3.83400$ Tm while the final ^{76}Ga fragments had a $B\rho = 3.43310$ Tm and entered the beam thermalization area at 90 MeV/u. The full acceptance of the separator was set to a momentum spread of $\Delta P/P$ = 0.5% where the largest contaminant ion in the secondary beam was $^{78}\text{Ge}^{32+}$. A schematic diagram of the experimental set-up for thermalization is shown in Fig. 3.7.

The degrader system reduced the kinetic energy of the high-energy beam down to $\sim$1 MeV/u and included a 1503(5) μm thick aluminum plate (so-called final degrader) whose effective thickness was varied by remotely adjusting its angle with respect to the beam's path. It also included a monoenergetic silicon dioxide (glass) wedge that was 1050(50) μm thick in the middle with a 5(0.9) mrad wedging angle that further reduced the relatively small momentum spread of the secondary beam (0.5% $\Delta P/P$), and a 37(2) μm thick aluminum window with a titanium alloy support grid (85(5)% transmission efficiency) located at the
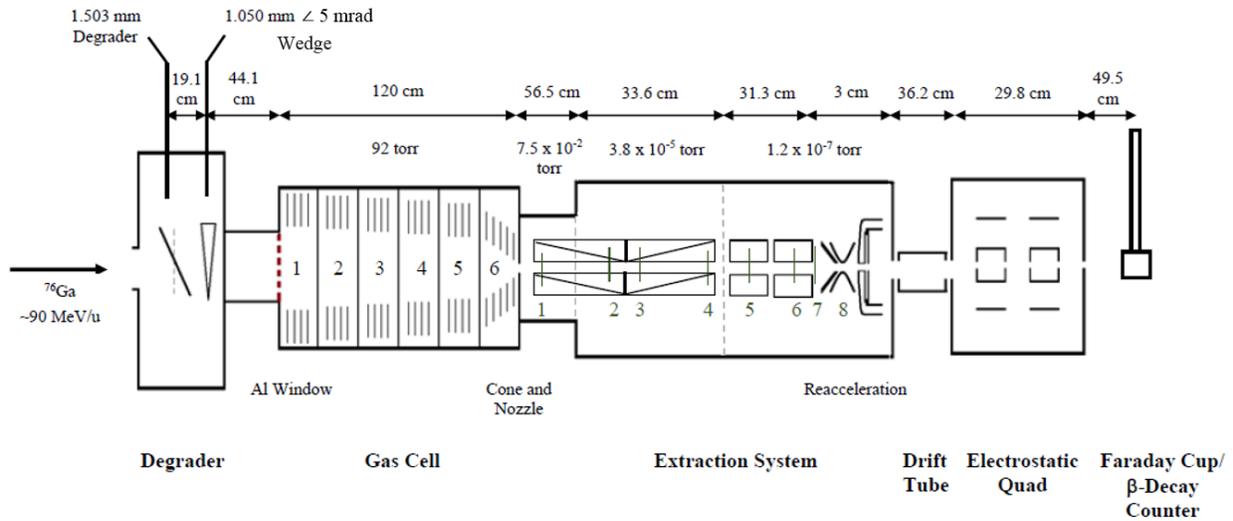
Figure 3.7: Schematic layout of the experimental equipment and set-up used to commission the NSCL's beam thermalization system. Distances between the components are given above in cm (not to scale).

entrance of the gas cell. The dispersion of the beam line was measured to be 15.4(0.9) mm/% difference in momentum, which results from the A1900 wedge angle [55].

Fragments proceed through the degrader system and into the buffer gas of the cell. Ultra high purity helium (99.999%) served as the buffer gas and was passed through a Monotorr purifier and a gas regulator system prior to entering the chamber. The helium gas was then flowed through the chamber at a rate in which a constant pressure of 123(12) mbar could be maintained. Due to the possibility of reactions during the drift, all components of the chamber were assembled to ultra-high vacuum standards, which kept the level of contaminants on the order of ppb or less [56]. Although limiting contaminants was a priority, some joints of the chamber were sealed with indium, which prevented the chamber from being baked. As a result, the chamber was found to contain a relatively high level of water vapor [2].

Even though the gas cell could not be baked, it was chilled to temperatures as low as
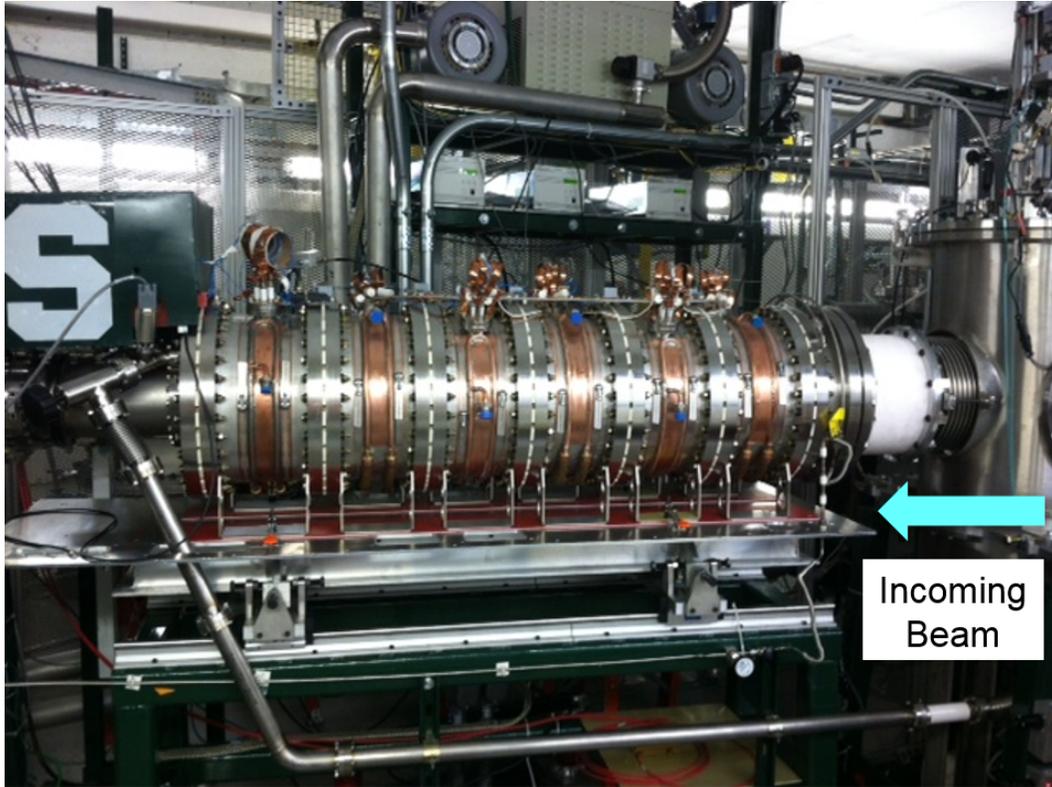
Figure 3.8: Photograph of the large volume linear gas cell when first installed at the NSCL. Note the large ceramic insulator at the front of the chamber.

-10°C. Therefore, in order to prevent short circuits from condensation and to protect the experimenters from the applied voltages, the gas was housed inside a stainless steel box filled with dry nitrogen, dubbed the "dry box." A picture of the gas cell without the surrounding dry box is shown in Fig. 3.8, where the six orange bonds are copper cooling jackets.

Once the projectile fragments were thermalized in the helium buffer gas, they were guided towards the exit nozzle by the DC drag and RF electric fields. A bias of 900V was applied between the entrance window (anode) and the exit nozzle (cathode) of the gas cell which produced an average DC drift field of 7.5 V/cm. Since the electrode spacing narrows in the cone, the RF frequency applied to the cone electrodes was 3.180 MHz at 50W where the peak-to-peak voltage, V_{pp}, was 31(2) V while the potential applied to the body electrodes was 3.514 MHz at 90 W with a V_{pp} of 32(2) V.

Under these conditions, the time needed for a typical ion of interest to drift half the length of the gas catcher was calculated to be 39(2) ms. Ions were jetted through a supersonic nozzle, where the total gas flow was measured to be 0.06(0.03) standard-L/s [2] and into a differentially pumped expansion chamber and RFQ ion-guide [52]. A three-stage differential pumping system was employed to evacuate the chambers in this section to 7.5 x 10^{-2} torr, 3.8 x 10^{-5} torr, and 1.2 x 10^{-7} torr. The gas cell and extraction system were floated on a high voltage platform at 30(0.5) kV to accelerate the ions into an electrostatic beam line that transported the ions to various experimental areas [2].

3.2.1.2   Measurements

The ionization created by the thermaliztion process provides important information on the incoming fast ions. In order to study the ionization, the negative ions (electrons) were collected inside the gas catcher, and the positive ions that exited the system were collected downstream of the catcher. Since the ions deposit their kinetic energy as they move through the gas, the gas cell can be operated as a large ionization chamber and thus measure the amount of ionization created by the incident beam.

Also, as discussed in Chapter 1, the stopping behavior observed for particles in gas is characteristically known as a Bragg curve [23]. The range distribution of the ^{76}Ga secondary beam in the gas was obtained by measuring (1) the total negative ion current collected on the window of the gas cell and (2) the total extracted positive ion current on a Faraday cup located downstream of the extraction system as a function of the final degrader's effective thickness. The examples shown in Fig. 3.9 were measured for an incoming beam intensity of 7.6 x 10^5 particles per second (pps), exhibit the typical Bragg curve shape, and agree within the uncertainties of the measurements. A systematic shift of 29(2) μm in the effective
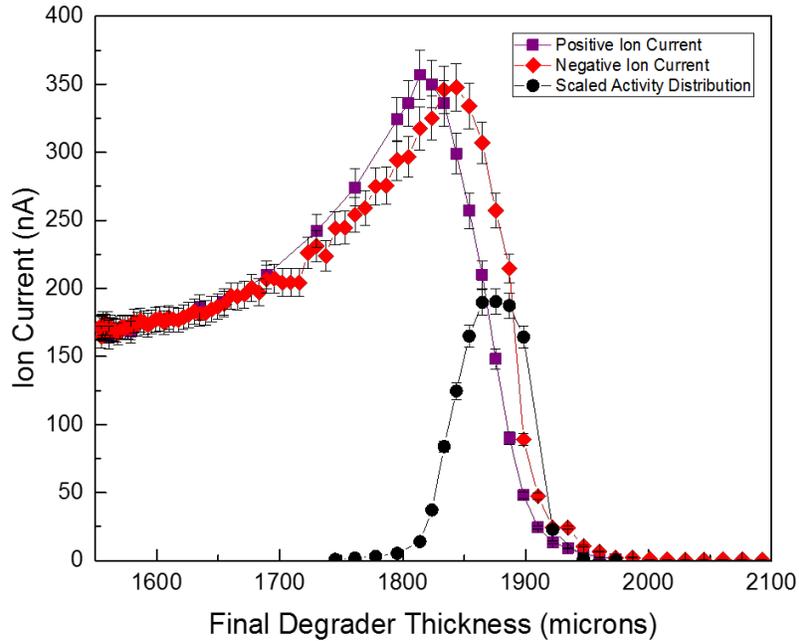
Figure 3.9: Measured positive (squares, nA) and negative (diamonds, pnA) ion current distributions for ^{76}Ga as a function of the effective final degrader thickness. The total activity distribution (circles, arbitrary scale) is shown for reference.

thickness of the final degrader was observed between the two measurements and was later found to be due to a mechanical lash in the system used to rotate the degrader. Here, the term "lash" describes the tendancy of the degrader system to return to a slightly different position after full rotation.

The total radioactivity extracted from the gas cell was collected on a thin foil, which was also operated as a Faraday cup, and measured by a silicon surface-barrier detector that was located directly behind the foil. The beta detector's efficiency was determined to be 33(2)% using a ^{90}Sr source with a known activity. In order to verify that the extracted radioactivity was indeed ^{76}Ga, growth and decay curves were collected with the silicon detector. An example of a measured decay curve is shown in Fig. 3.10 [2]. These decay curves were then used to determine the total extracted radioactivity as a function of the final degrader's
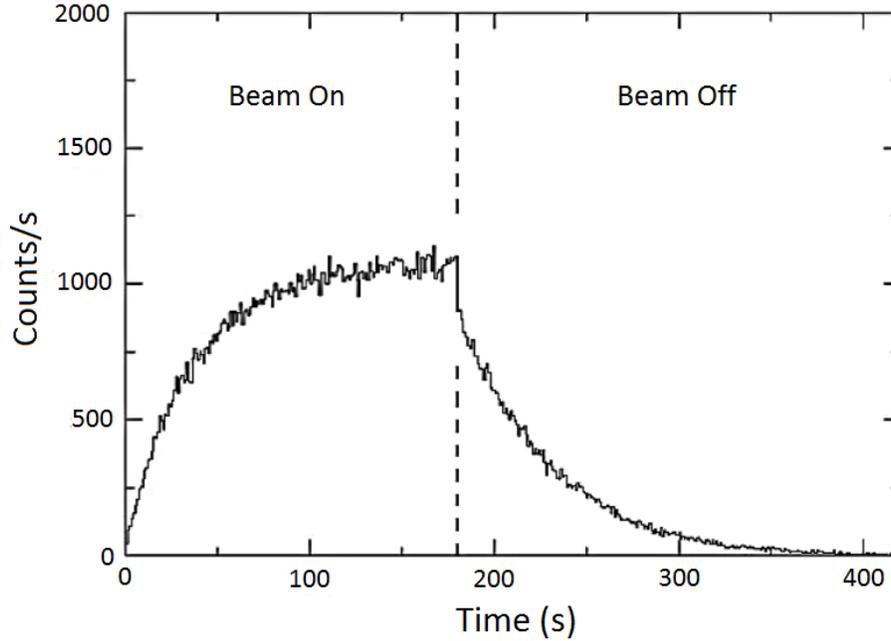
Figure 3.10: Example of a growth and decay curve for the total extracted radioactivity. This curve was obtained when the final degrader was set for the maximum extracted radioactivity (34°). The data are in agreement with the known 33s half-life for ^{76}Ga [2].

effective thickness, and an example of these results are shown by the black circles in Fig. 3.9.

The activity distribution was normalized in the y-axis for dispay purposes and is broad with a peak near the mid-point of the falling edges of the Bragg curves as expected. The broadening is a result of range straggling, where stochastic fluctuations in particle interactions cause slightly different path lengths for individual particles with the same initial energy combined with any residual energy spread after the wedge. The peak is typical because the mid-point of the falling edge of a Bragg curve is used to define the mean range of particles in a given material [23]. Since it is important to extract the maximum amount of radioactivity, the optimal angle for the final degrader was set at 34° (1876(5) μm) for measurements of the mass distribution of the ions [2].

The mass distributions for both the stable and radioactive ions extracted from the gas cell were determined by using a mass-analyzing magnet located downstream of the extraction

52
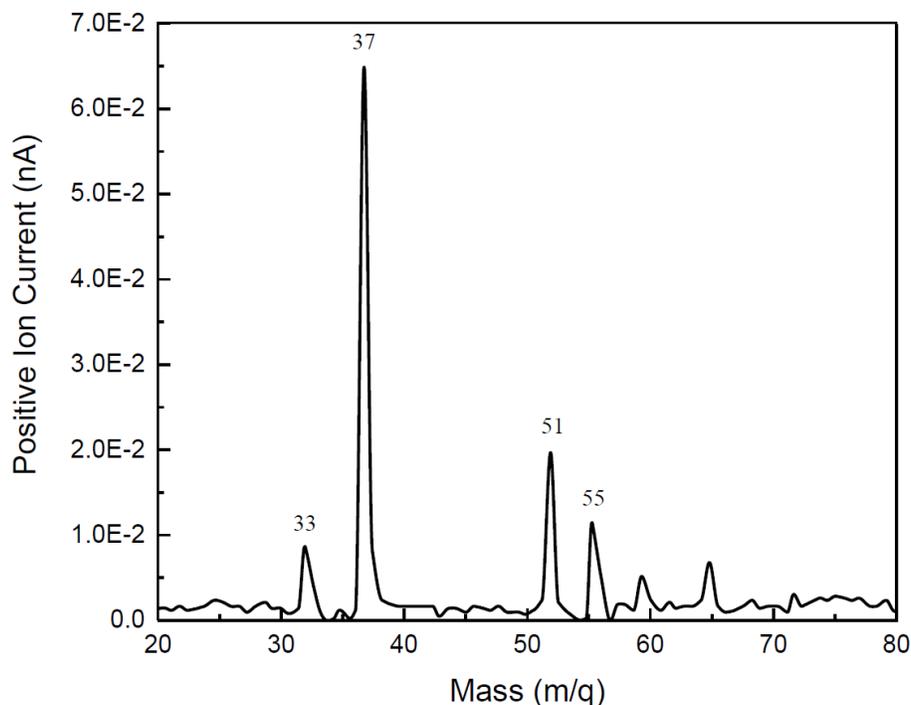
Figure 3.11: Part of the mass-to-charge spectrum obtained for the stable ions extracted from the gas cell, see text for details.

system. The resolution of the magnet, $m/\Delta m$, was on the order of 50 which provided sufficient separation of individual mass numbers in the region of interest. A second Faraday cup/silicon surface-barrier detector device was placed at the image position of the mass analyzer to measure the electrical current of stable ions and the counting rate of radioactive ions, respectively, as a function of their mass-to-charge value (m/q) [2].

It is interesting to note that peaks were observed at essentially all integral m/q values of positive ions extracted from the gas cell. Part of the observed mass spectrum is shown in Fig. 3.11 [2]. Recall that the chamber was not baked prior to commissioning, so water was expected to be present. The prominent peaks in the stable m/q spectrum at 37 and 55 were thus attributed to the molecular water ions $[H_3O(H_2O)]^+$ and $[H_3O(H_2O)_2]^+$, respectively, while peaks at 33 and 51 were attributed to the closely related $[CH_3(H_2O)]^+$ and $[CH_3(H_2O)_2]^+$ molecular ions. These molecular ions were most likely created by charge

Ion	m/q	Decay Rate (cps)	Fraction (%)
$^{76}\text{Ga}^{2+}$	38	< 20	< 1 (0.3)
$^{76}\text{Ga}^{+}$	76	2070	24.3 (0.6)
$[^{76}\text{Ga}(\text{H}_2\text{O})]^{+}$	94	2753	32.3 (0.5)
$[^{76}\text{Ga}(\text{H}_2\text{O})_2]^{+}$	112	2012	23.6 (0.7)

Table 3.1: ^{76}Ga radioactivity molecular ion distribution.

transfer reactions from primary helium ions to neutral impurities in the gas that undergo subsequent chemical reactions with the contaminant water molecules in the gas prior to extraction.

Note that the total radioactivity was measured prior to mass separation, but the radioactive ion distribution was determined for m/q values in the range of 30 to 120. For an incident beam rate of 7.3 x 10^3 pps, the bulk of the activity was localized in three peaks whose counting rates and percentage of the total extracted activity are given in Table 3.1. Although some water contamination was expected, the amount of water and exrint of its effects on the ion of interest was significantly underestimated. As such, the designated mass range could only account for roughly 80% of the total extracted radioactivity. The remaining 20% was, therefore, assumed to lie at higher mass values.

The yield of incident projectile fragments that are extracted from the gas cell is sensitive to two independent efficiencies: the stopping efficiency, ε_{stop}, and the extraction efficiency, ε_{ex}. The former describes the fraction of thermalized fragments stopped within the gas while the latter describes the fraction of thermalized fragments that are extracted from the gas. Therefore, the activity collected would be $R\,\varepsilon_{stop}\,\varepsilon_{ex}(1 - \text{e}^{-\lambda t})$ where t is the collection time, and the saturated activity observed in the beta-decay counter downstream of the extraction system, A_{sat}, can be written as $A_{sat} = R\,\varepsilon_{stop}\,\varepsilon_{ex}$ where R is the incoming ^{76}Ga beam

rate accounting for beam purity. The stopping efficiency was calculated to be 0.86 with the LISE++ program [6]. Details of this program and calculation will be discussed in Chapter 4. The extraction efficiency was thereby obtained by dividing A_{sat} by ε_{stop} and R as well as accounting for the detector and transmission efficiencies. Extraction efficiencies for the commissioning experiments with ^{76}Ga were determined for implantation rates ranging from 9.3 x 10^2 pps to 7.6 x 10^5 pps and varied from 37% to 18%, respectively.

3.2.2 Improvements after Commissiong

Following the commissiong runs, several improvements were made to enhance the performance of the NSCL's large volume gas cell. These changes included: enhancing the vacuum system of the cell, replacing the entrance window, and adding a stable ion test source. As previously mentioned, due to the inability of the cell to be baked, some water was expected to be present in the helium gas, which would result in unwanted chemical reactions. In fact, results from the commissioning runs indicated that water was involved in a substantial amount of reactions and less than 25% of the ^{76}Ga ions extracted from the large volume gas cell were free from an attached water [2]. A major change was made in an attempt to remove the water from the system when it was not in use: the gas volume was extended to allow a new turbomolecular (turbo) pump that could pump directly on the gas chamber.

Prior to commissioning, the only way to remove gases from the chamber was to pump through the small nozzle of the cell and a small bypass valve. Given the volume of the gas catcher and the size of the nozzle, the pumping of the chamber was limited to 0.06(0.03) standard-L/s as previously mentioned. By implementing a new high voltage insulator, the window section of the gas cell was redesigned to include a ring with multiple ports, as seen in Fig. 3.12. A small 6" turbo pump was added to one of the six new ports, and the chamber
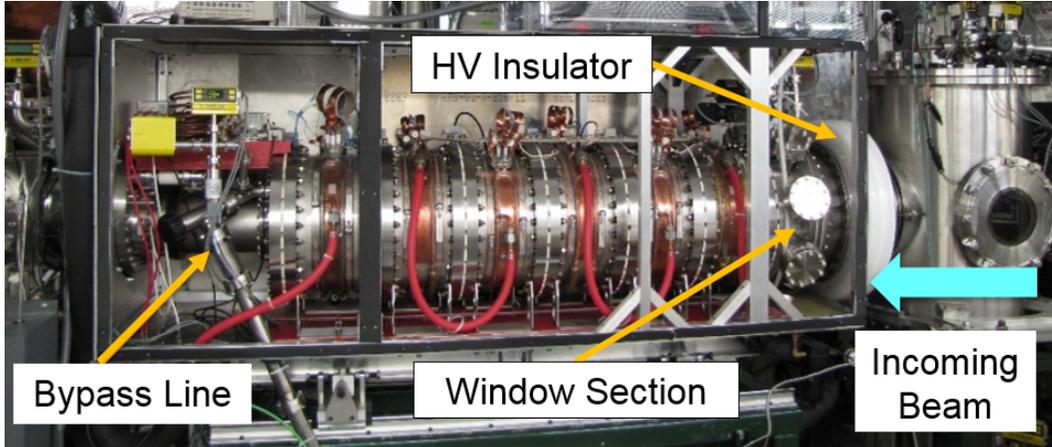
Figure 3.12: NSCL's large volume linear gas cell with upgraded insulator, ports, and dry box.

was left under high vacuum whenever it was not in use to reduce the residual gas.

A residual mass analyzer (RGA) was installed at the same time as the turbo, and was placed just downstream of the gas cell to quickly analyze any contaminants. Results from the RGA suggested that the water contaminant was essentially removed from the cell, which should have resulted in very little molecular ion formation from the ions of interest in later runs. Fig. 3.13 compares the molecular ion formation between two similar potassium experiments. One experiment was run prior to the addition of the turbo pump while the other was run after the addition of the turbo pump. These results confirm that the addition of the turbo pump successfully reduced the water contaminent within the gas cell to insignificant levels. The discrepancy in counts between the two experiments resulted from lower beam rates from the cyclotron in the second experiment.

The aluminum window located at the entrance of the gas cell was also replace. This window must be able to withstand the pressure difference between the high vacuum in the degrader pot just upstream of the cell ($\sim 10^{-7}$ torr) and the gas chamber itself ($\sim 10^2$ torr). The original window, 10 μm thick with a titanium alloy support grid, showed extreme
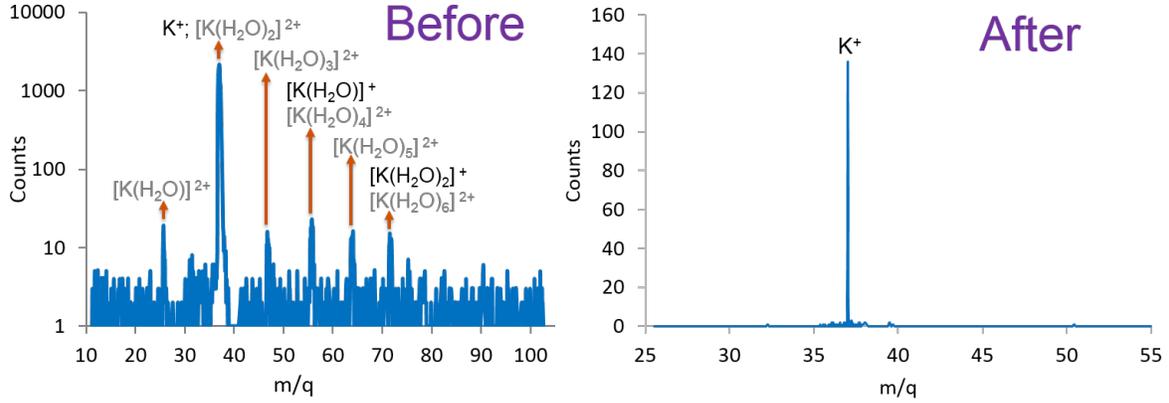
Figure 3.13: The graph on the left shows a mass scan for radioactive ions from an early ^{37}K experiment. The graph on the right shows a similar mass scan for the same ^{37}K radioactive ion from an experiment performed after a turbomolecular pump was added to the large volume linear gas cell. While the ^{37}K ion was fragmented among numerous molecular ions containing water during the first experiment, no molecular ion formation was observed in the second experiment. See text for more details.

deformation after the commissioning experiments, see Fig. 3.14. This deformation can cause increased range straggling because depending on the beam's position on the window, the ions could travel through variable thicknessess of material. In addition, the crinkles increase the probability of the window failing under the pressure difference. To ensure the proper behavior of the window, a new 49 μm window was installed. Photographs of the new and old window are shown in Fig. 3.14.

3.2.3 Summary of Efficiency Measurements

The extraction efficiency (ε_{ex}) of the NSCL's large volume linear gas cell was taken to be:

$$\varepsilon_{ex} = \frac{\frac{Outgoing\,Rate}{\varepsilon_{det}*\varepsilon_{trans}*\varepsilon_{stop}}}{Incoming\,Rate * Beam\,Purity}, \tag{3.1}$$

where ε_{det} is the detector efficiency, ε_{trans} is the transport efficiency to the detecor, and ε_{stop} is the stopping efficiency within the gas. Remember, that the detector efficiency was
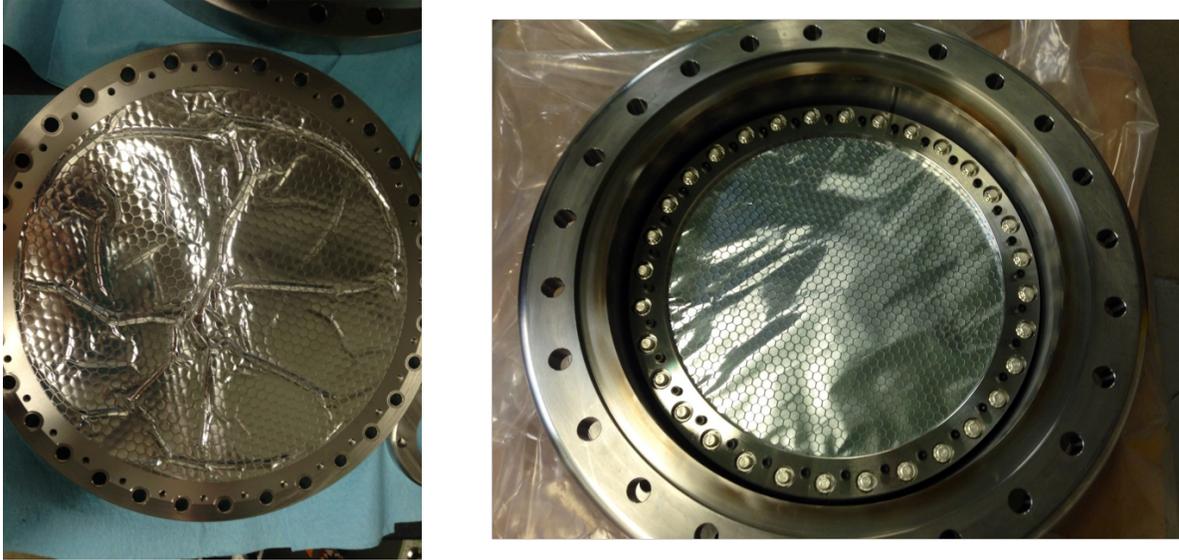
Figure 3.14: The picture on the left shows the deformed 10 μm thick aluminum window while the new 49 μm thick window is shown on the right.

measured with a radioactive source and was found to be 0.33(0.05), and the transmission efficiency was measured with the current of stable ions and was found to be 0.85(0.05). The beam purity for each experiment was provided by the A1900.

Data from the commissioning experiments as well as other low-energy user experiments was used to determine the extraction efficiency of the NSCL's large volume linear gas cell was measured as a function of the incoming beam rate. These results were summarized and are shown in Fig. 3.15. The extraction efficiency can be seen to decrease with $\sim 1/\sqrt{IncomingRate}$ [38, 57] at incoming rates larger than ~ 5 x 10^5 pps, which indicates the instances where space charge and plasma effects become significant within the NSCL's large volume linear gas cell. For ionization-rate densities above this threshold, the space charge effects are apparent in the observed Bragg curves for both the extracted positive ion current and internally collect negative ion current.

In higher rate cases, not only is the positive ion current significantly suppressed, but due to recombination and other plasma effects within the gas, the negative ion current is
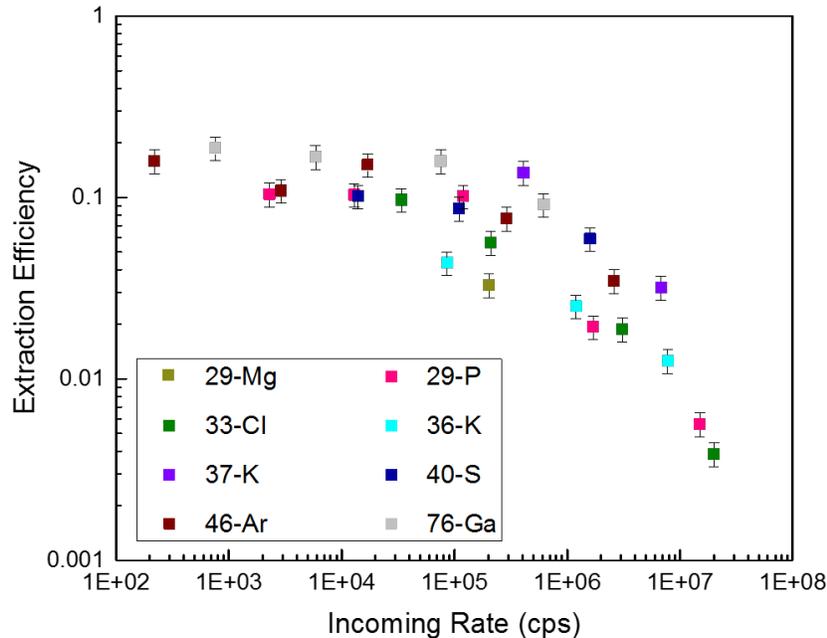
Figure 3.15: Graph of extraction efficiencies as a function of incoming rate for initial commissioning and chemistry experiments performed with the NSCL large volume gas cell.

also suppressed. This supressed behavior was more easily discernable in some of the later experiments. Results from one of the characterization experiments involving ^{33}Cl (see Table 3.2) was chosen as the best visual example of supression with increasing rates and shown in Fig. 3.16. Similar to the results shown for the ^{76}Ga commissioning experiments (Fig. 3.9), these graphs include both the positive and negative ion currents as well as the activity distribution as a function of final degrader thickness. Graph A shows the results for an incoming rate of 3.4 x 10^4 pps while graph B shows the results for an incoming rate of 3.1 x 10^6 pps. Given the incoming rates for graph B were about a factor of 100 higher than those of A, the extraction rates observed in graph B should have also been about a factor of 100 higher. Due to space charge and plasma effects, though, the negative ion current is supressed by 53% while the positive ion current is supressed by 96%.
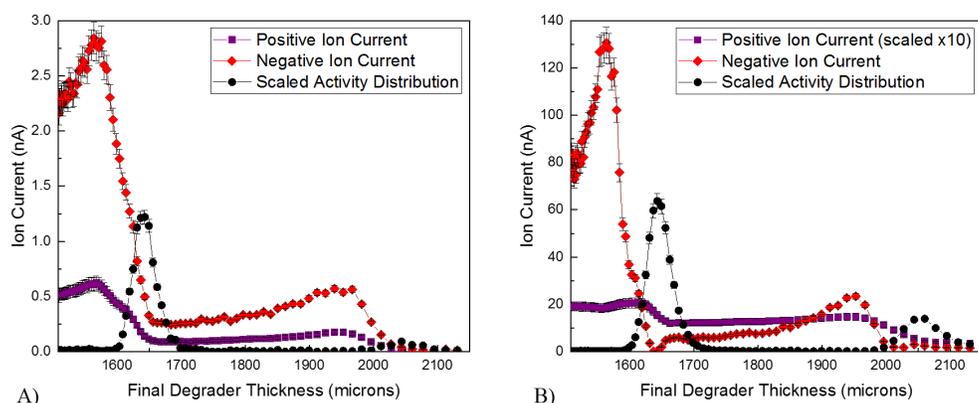
Figure 3.16: Measured positive (squares) and negative (diamonds) ion current distributions for ^{33}Cl as a function of the effective final degrader thickness for an incoming rate of A) 3.4 x 10^4 pps and B) 3.1 x 10^6 pps. A ^{30}P contaminant was present in the fragment beam delivered by the A1900. This contaminant accounts for the second observed peak in the graphs. See text for details.

In order to directly compare the results obtained from the NSCL's large volume linear gas cell to previous generation devices (Fig. 2.9 [38]), the ionization-rate density (Q) for each experiment needed to be determined. The ionization-rate density, discussed in 1.2.2, was calculated using Eq. (1.4) for each ion and its respective rates. The comparison between similar medium-massed measurements made with previous gas cells and measurements made with the NSCL large volume linear gas cell is show in Fig. 3.17.

Although similar such losses and trends observed in previous devices were also observed in the NSCL large volume linear gas cell, the more significant losses from this cell did not occur until significantly higher Q-values were attained. This observation indicates that the larger volume, enhanced electrode structure, and added RF potentials of the NSCL's large volume linear gas cell were successful in improving the overall efficiency of the system. Various experimental conditions and ions thermalized by the NSCL large volume linear gas cell are summarized in Table 3.2. Detailed simulations and conclusions of the complete system are presented in the next chapter.
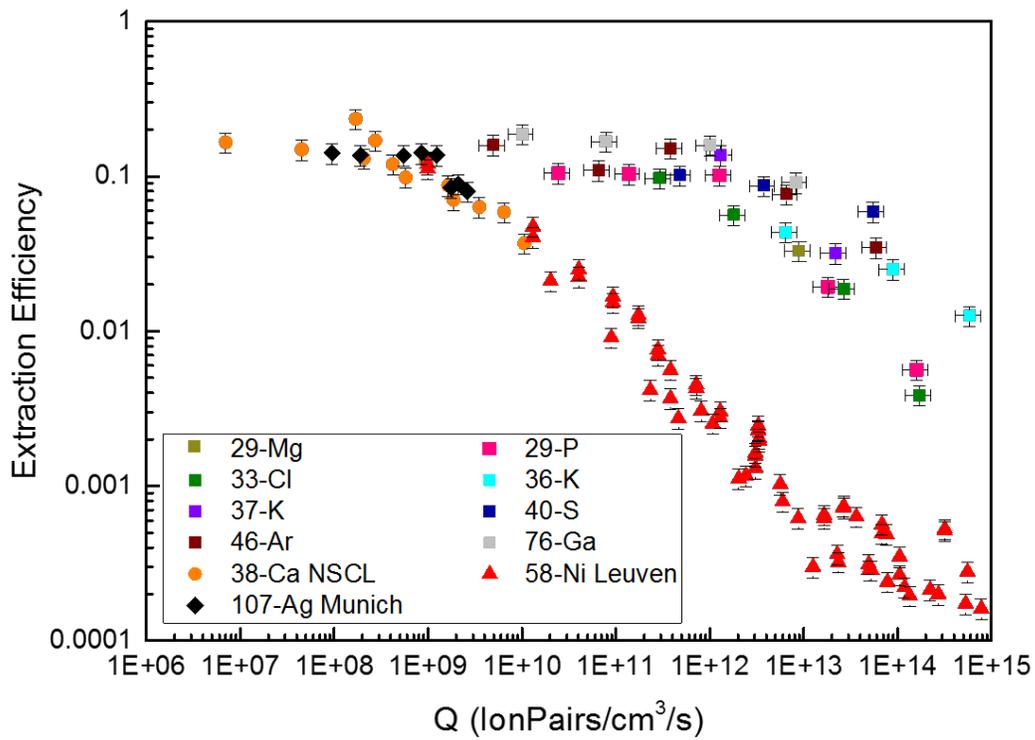
Figure 3.17: Graph of extraction efficiencies as a function of Q for previous generation devices (orange circles, red triangles, and black diamonds) as well as the initial commissioning and chemistry experiments performed with the NSCL large volume gas cell (all squares).

Ion	Incoming Rate (cps)	Q (IonPairs/cm^3/s)	Beam Purity	ε_{stop}	Outgoing Rate (cps)	ε_{ex}
^{29}Mg	2.1 x 10^5	2.5x10^{12}	0.90	0.51	1.7 x 10^3	0.032
^{29}P	1.5x10^7	1.3x10^{14}	0.12	0.38	1.0x10^3	0.006
	1.7x10^6	1.5x10^{13}			4.2x10^2	0.019
	1.2x10^5	1.1x10^{12}			1.5x10^2	0.102
	1.3x10^4	1.2x10^{11}			1.7x10^1	0.103
	2.3x10^3	2.1x10^{10}			3.0x10^0	0.105
^{33}Cl	2.0x10^7	6.7x10^{13}	0.21	0.76	3.5x10^3	0.004
	3.1x10^6	1.0x10^{13}			2.6x10^3	0.019
	2.1x10^5	7.0x10^{11}			5.3x10^2	0.056
	3.4x10^4	1.1x10^{11}			1.5x10^2	0.097
^{36}K	7.8x10^6	1.8x10^{14}	0.03	0.89	7.4x10^2	0.013
	1.2x10^6	2.7x10^{13}			2.3x10^2	0.025
	8.6x10^4	1.9x10^{12}			52.8x10^1	0.044
^{37}K	6.8x10^6	7.5x10^{12}	0.27	0.91	1.4x10^3	0.032
	4.1x10^5	4.5x10^{11}			3.5x10^2	0.137
^{40}S	1.6x10^6	1.6x10^{13}	0.83	0.55	2.4x10^4	0.059
	1.1x10^5	1.1x10^{12}			2.4x10^3	0.087
	1.4x10^4	1.4x10^{11}			3.8x10^2	0.102
^{46}Ar	2.6x10^6	1.2x10^{14}	0.86	0.48	2.1x10^4	0.035
	2.9x10^5	1.3x10^{13}			5.1x10^3	0.077
	1.7x10^4	7.8x10^{11}			6.0x10^2	0.152
	2.9x10^3	1.3x10^{11}			7.3x10^1	0.109
	2.2x10^2	1.0x10^{10}			8.0x10^0	0.159
*^{76}Ga	6.2x10^5	1.7x10^{12}	0.79	0.86	1.1x10^4	0.091
	7.6x10^4	2.1x10^{11}			2.3x10^3	0.159
	5.9x10^3	1.6x10^{10}			1.9x10^2	0.168
	7.6x10^2	2.1x10^9			2.7x10^1	0.187

Table 3.2: Summary of various low-energy chemistry experiments performed with the NSCL large volume linear gas cell. ^{76}Ga is starred because it is the only experiment shown that was conducted prior to the improvements made to the vacuum system.

Chapter 4

Simulating the NSCL's Large Volume Linear Gas Cell

As discussed in Chapter 3, results from the commissioning and other low-energy experiments were used to establish a decreasing trend for the extraction efficiency, as well as the directly related Q-value, as a function of the incoming beam rate. This trend indicates that space charge and plasma effects are still present within the NSCL's large volume linear gas cell. In order to understand how and where the efficiency losses from these effects occur and also to reproduce and to one day predict the observed behavior of this device, numerous modeling programs and simulations were incorporated and performed. These simulations integrated not only the intricate electrode structure but also the multiple electric fields and potentials present throughout the large volume cell. Given the extensive measurements made during the commissioing experiments, ^{76}Ga was used as the example case for the simulations.

4.1   SRIM

The Stopping and Range of Ions in Matter (SRIM) code calculates the energy loss of ion beams in matter. This calculation tracks each individual ion and its respective collisions with atoms of various target materials. Here, the stopping powers of the target compounds are estimated with Bragg's Rule, and the collisions between the moving projectile ions and

stationary target atoms are simulated by Monte-Carlo methods. These statistical algorithms account for both short and long range interactions and allow an ion to make jumps between calculated collisions, while the collision results are averaged over the intervening gap [3]. For the present work, the Transport of Ions in Matter (TRIM) program, part of the SRIM package, was used to study the energy deposited by the ^{76}Ga ions as well as the range of these ions through the degraders, wedge, window, and helium buffer gas [4].

The ion, ion mass, and kinetic energy of the projectile beam as well as the compounds, thicknesses, and density values for the target materials used during the commissiong experiments were first loaded into the program. Next, the beam energy, wedge, window, and gas material settings were held constant while the degrader thickness was varied between 1555–1740 μm. Finally, a fixed number of 1000 ions were generated from a point-source and introduced into the system. The resulting affect on the ionization, or energy deposited per ion, and the range of the ions through the system was studied for the varyious degrader thicknesses. An example of the TRIM set up window with applicable values is given in Appendix A.

As discussed in Chapter 3, the beam was delivered with a 0.5% momentum spread. This spread was accounted for by changing the kinetic energy setting for the projectile beam and re-evaluating the results for each degrader thickness. Results from one kinetic energy setting are shown in Fig. 4.1. The ionization and range curves were generated by calculating the average energy loss per ion and the average range per ion, respectively, at each degrader thickness. Although the ionization curve was plotted directly, the first derivative of the original range curve was calculated and plotted in order to determine the optimal thickness of degrader material.

These individual energy plots were integrated and compared to the experimental results
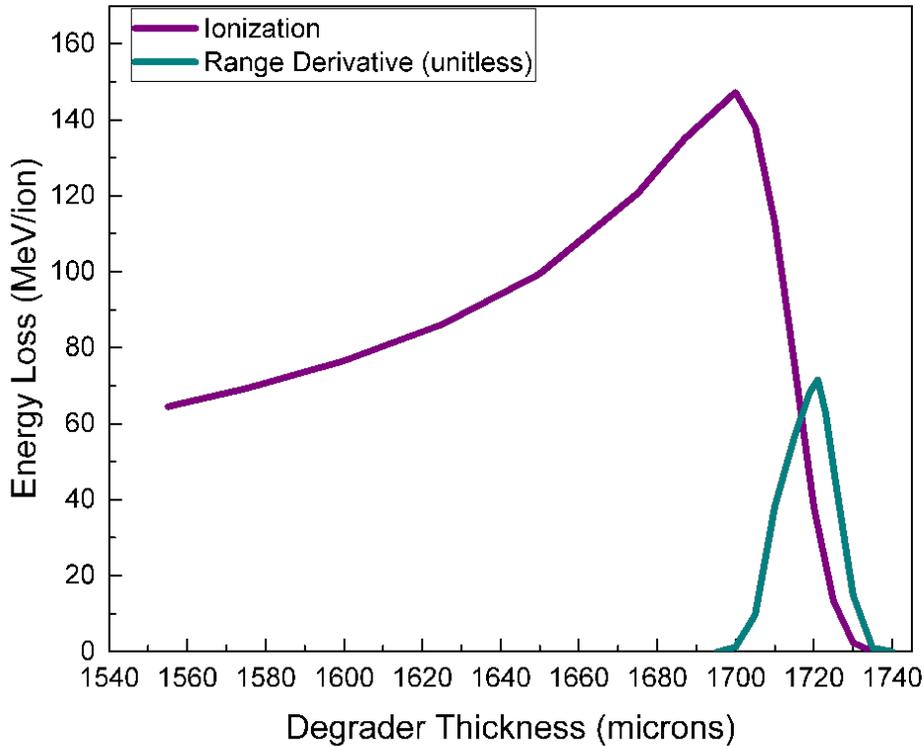
Figure 4.1: Summary of ionization and range results obtained for the center of the momentum distribution of the ^{76}Ga ions with TRIM program.

as shown in Fig. 4.2 [2]. It should be noted that the simulated data was shifted $+136(1)\mu$m for this comparison. Aside from this shift, which was attributed to a slight miscalibration in the magnetic rigidity of the A1900 [34] fragment separator, the simulated data generally agrees with the experimental results in both shape and maximum energy loss. The small width differences observed between the experimental data and the TRIM calculations was attributed to both the TRIM assumption of the beam as a point-source and the increased range straggling experienced by the ions due to the deformation in the original window (see Chapter 3 for details).
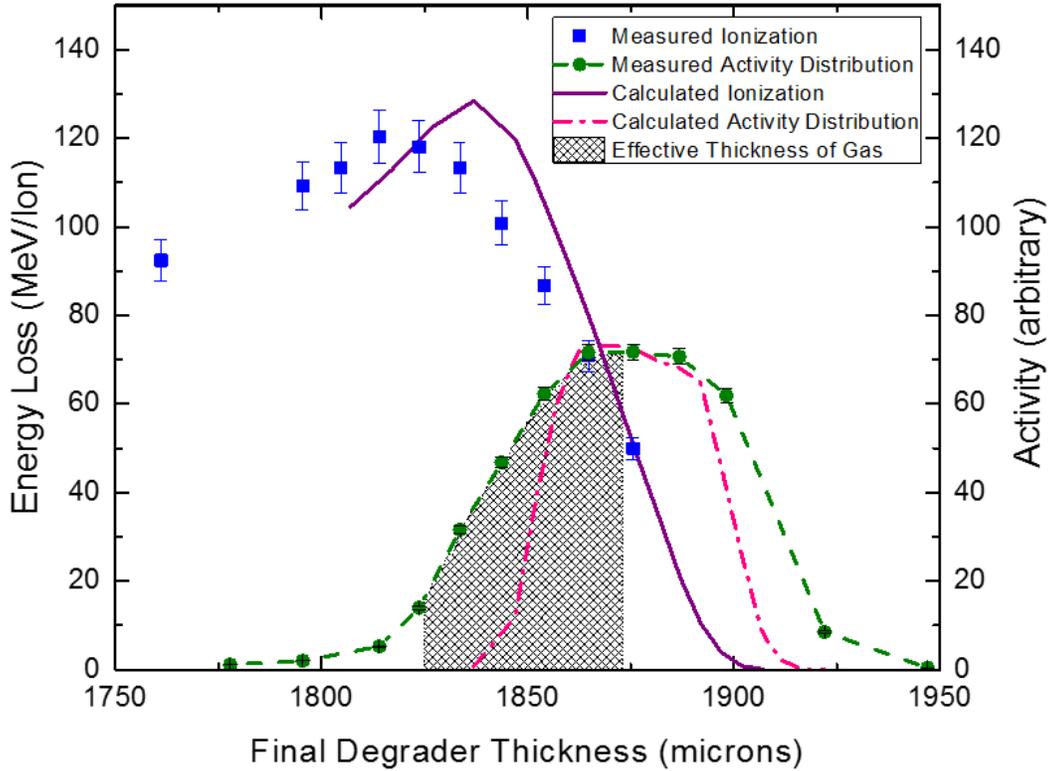
Figure 4.2:   The measured Bragg curve (squares) and activity distribution (circles with dashed line) for ^{76}Ga are compared to the predicted curves from the TRIM code (solid line and dash dot line, respectively). The hatched area represents the equivalent thickness of the helium gas and is shown for reference.

4.2   LISE++

LISE++ is a program designed to predict the purity and intensity of radioactive ion beams produced with in-flight separators. Although numerous production mechanisms and reaction models are included in the code, projectile fragmentation is appropriate for the current work [6]. In accordance with its most common functions, LISE++ was used for both experimental planning and on-line tuning during experiments. The focus here, though, will be placed on the various utilities and tools available with this program to study the range distribution of the fragment beam ions, the energy deposited by these ions in the helium buffer gas, and the stopping efficiency of the buffer gas itself.
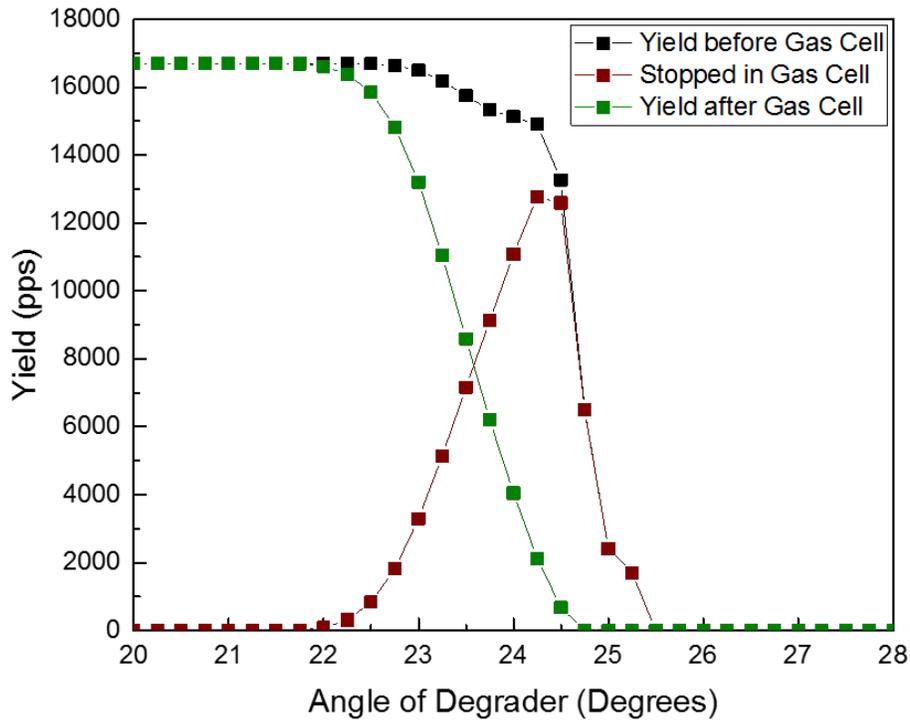
Figure 4.3: Range optimization in gas results for ^{76}Ga ion beam thermalized during the commissioning experiments. These results were generated with the LISE++ program and show an optimal degrader angle of $24.5°$.

Unlike SRIM, which can only calculate the interactions of a pure secondary beam, LISE++ calculations begin with a primary ion beam. This primary beam is impinged upon a target, therby producing a secondary fragment beam through projectile fragmentation. Given the production mechanism, the secondary fragment beam is initially composed of numerous ions and isotopes. However, after separation with the A1900 fragment separator, this beam is mostly composed of the desired isotope of interest. Although the A1900 is already built into the program, the beamline downstream of the separator must be constructed using the "set-up" options [6]. Once assembled, complete calculations and simulations from production through thermalization can be performed.
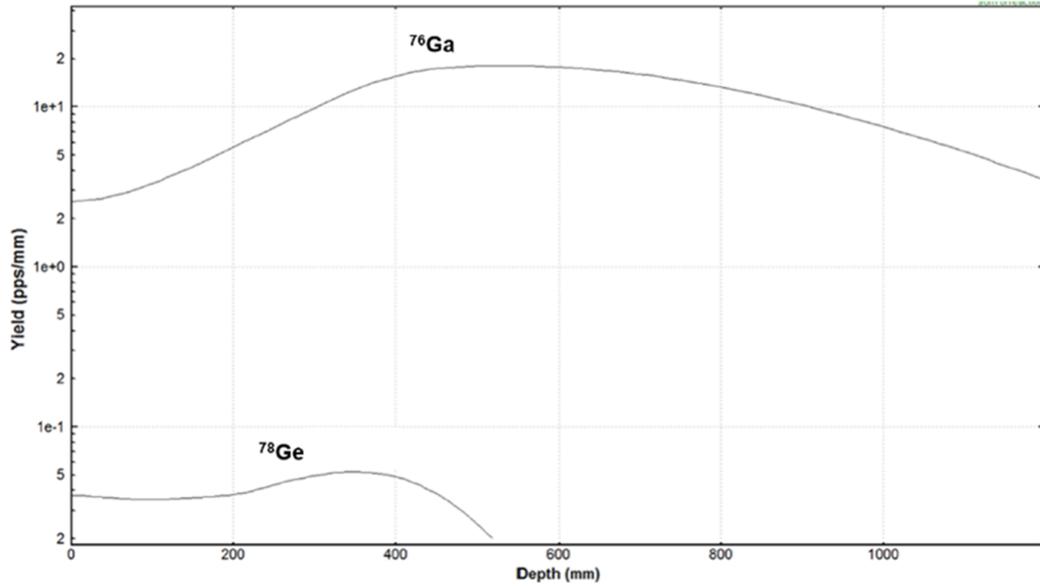
Figure 4.4: Range distribution for ^{76}Ga fragment beam calculated with the LISE++ program. At the optimal degrader setting, the ions of interest will stop in the middle of the large volume cell (600 mm). Notice that the ^{78}Ge contaminant ion is supressed to zero pps/mm at the optimal setting while the ^{76}Ga ion of interest will be extracted at its peak of 19(1) pps/mm.

As alluded to above, fragment beams produced through projectile fragmentation and subsequent separation are rarely 100% pure. As such, it is important to recognize that the composition of the fragment beam will change due to isotopes varying range distributions in the gas. For the commissioning runs, an 81(1)% pure ^{76}Ga fragment beam was delivered to the beam thermalization area. The main contaminant of this secondary beam was ^{78}Ge. Suppression of contaminant ions is one of the more understated, but significant, functions of a variable degrader. The optimal variable degrader setting for maximum suppression of contaminants with minimal loss to the ion of interest can be quickly determined, similar to SRIM methods, through a "Range optimizer (gas cell utility)" function found within the LISE++ program, see for example Fig. 4.3. Results from this optimization were checked by the respective SRIM results (Fig. 4.1) and found to vary by less than 1%. Fig. 4.4 confirms
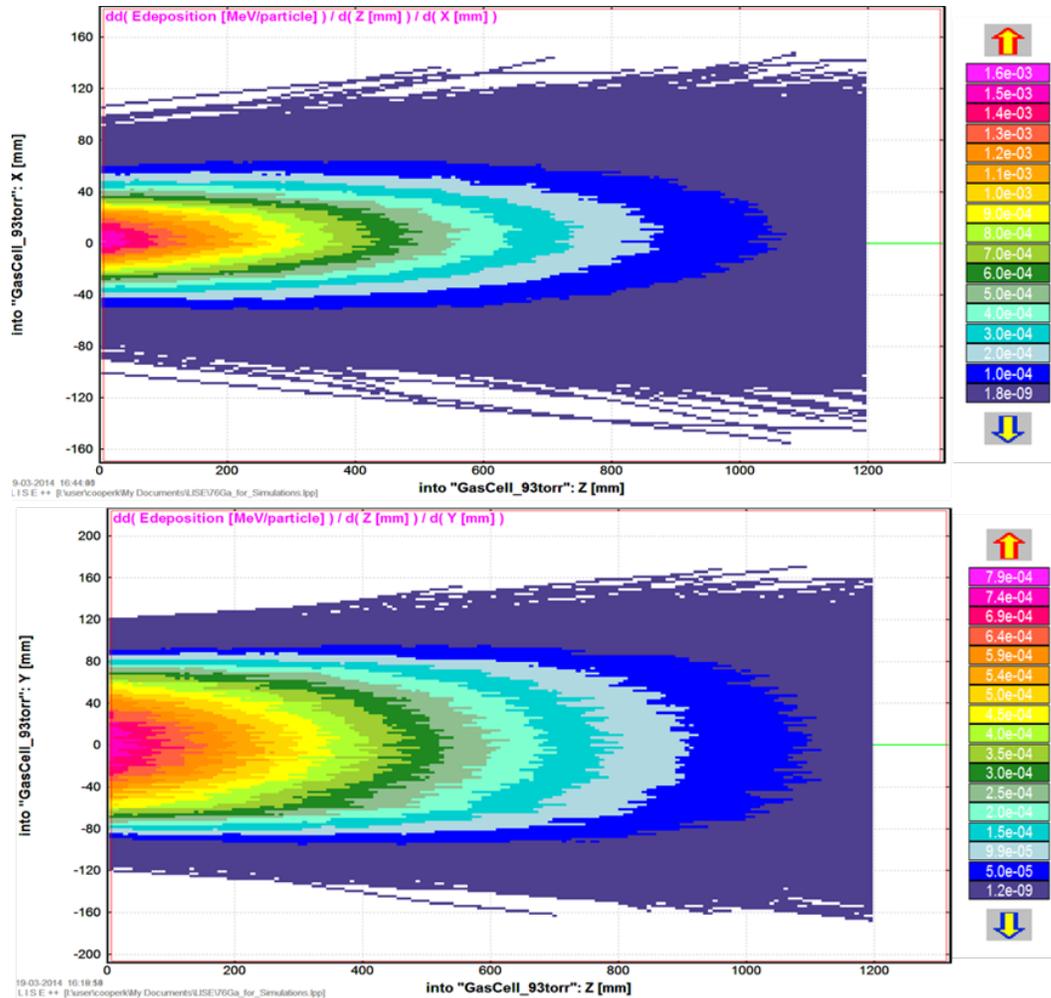
Figure 4.5: Energy deposition in X vs Z (Top) and Y vs Z (Bottom) for the ^{76}Ga fragment beam simulated with the LISE++ program.

that the ^{78}Ge contaminant will be significantlly supressed with minimal loss to the ^{76}Ga ion of interest at the optimal final degrader angle.

Along with determining the optimal degrader angle, the range optimizer function can also be used to estimate the stopping efficiency of the gas at each angle. The number of ions stopped in the gas per angular step can first be deduced by comparing the number of ions present in the ^{76}Ga beam before and after interactions occur within the gas. Then, the stopping efficiency for the large volume linear gas cell can be calculated by comparing the number of ions stopped in the gas to the number of ions entering the gas cell at the peak

of the stopping curve. For the example shown in Fig. 4.3, the theoretical stopping efficiency was calculated to be 0.86 at the optimal degrader angle which agreed within error of the experimentally determined value of 0.84 (0.04).

Once the optimal degrader angle was determined, it was possible to simulate the energy deposited in the gas. LISE++ includes a calculation of the ion-optics of the beam line and can simulate the size and angular divergence of the secondary beam at any position along its path. In the present work, this feature was used and Monte Carlo simulations were performed to calculate the ionization in the gas as a function of position. Projections of the calculated energy deposition in MeV/particle are shown for the ^{76}Ga case in the X-Z and Y-Z planes in Fig. 4.5. The data was then uploaded to Mathematica and both the energy deposited in a volume element and the number of ion pairs created per particle in that element were determined. These values, along with the values obtained from the projection of each graph onto its respective axes, became inputs for the particle-in-cell code (3DCylPIC) which relates the energy deposited to the space charge created in the gas.

4.3   3DCylPIC

3DCylPIC [7] is a 3D particle-in-cell (PIC) code that was developed to study and characterize the space charge effects in various cylindrical ion traps and transport devices. This program solves Poisson's equation for an arbitrary number of charged particles on a cylindrical grid at every time step. As a result, it can calculate a self-consistent charge density and the resulting space charge potential on that grid. In order to obtain the most accurate results, 3DCylPIC allows for the inclusion of internal electrodes, magnetic fields, and hard sphere collisions and scattering of ions with a neutral buffer gas [7]. For the present large volume

linear gas cell, this code was used to calculate the self-consistent space charge potential for a given incoming ^{76}Ga ion beam rate, gas pressure, and DC drag field in the body of the cell.

The dimensions of the cell and the electrode design were hardcoded into the simulations, while all other relavant parameters were variables input with a configuration file. These variable parameters included the pressure, temperature, and mass of the buffer gas, the applied DC drag field, and the ion and electron masses, mobilites, and charges. The charges were scaled in order to account for the various incoming beam rates, and this factor was calculated with the equation [58]:

$$chargescale = \frac{\Phi_{RI} * \bar{E} * \Delta t}{E_{IP} * \Phi_{IP}}, \tag{4.1}$$

where Φ_{RI} is the incoming beam rate (pps), $\bar{E}$ is the average energy deposited per particle (eV/ion), Δt is the simulation time step (s), Φ_{IP} is the energy required to create an ion pair (eV/IP), and Φ_{IP} is the number of ion pairs created per time step in the simulation. For these simulations, the time step was limited to values less than the theoretical time for an electron to advance one grid unit. This input parameter, along with the number of ions released per time step and the ion advancement steps, controlled the resolution of the simulation. The physical size and energy deposition results obtained from LISE++ for the ^{76}Ga beam were also used as input parameters in this file. After the configuration file was successfully uploaded, charged particles were continuously introduced into the system, and the charge density was tracked until an equilibrium was established. An example configuration file is shown and discussed in Appendix B while some of the simulation results are shown and discussed below.

The evolution of the charge density as a function of time for the various incoming beam

rates studied in the commissioning experiments is shown in Fig. 4.6. In these visualizations, the red line shows the rapid migration and collection of the electrons while the black line shows the slower migration and collection of the helium ions. Although essentially all of the ions injected into the system are collected after $\sim$0.1 s, a plasma begins to form at higher incoming beam rates ($\geq$$10^5$ pps). This plasma is evident in the erratic electron, red line, fluctuations seen in the bottom right of Fig. 4.6. Remember that the positive space charge potential that builds up inside the gas cell as the incoming beam rate increases. At higher rates, this potential becomes large enough to form a plasma that traps both the ions and electrons inside the system. This increased potential also adds an extra push to the positive ions located on the edge of the plasma and explains why the time required for the system to reach equilibrium decreases as the incoming rate is increased.

In order to better understand these space charge effects, the evolution of the space charge potential is also studied. Fig. 4.7 shows the applied potential, the space charge potential at equilibrium, and a graph of the evolution of the space charge potential over time. All of these illustrations are shown for an incoming beam rate of 10^4 pps. The upper left illustration is a temperature map that shows the applied potential of the system including the effects of the electrode spokes at a specific Z point in the gas cell. The upper right illustration is a similiar temperature map but is representative of the space charge potential present at equilibrium throughout the whole gas cell. Here, the space charge potential was determined by subtracting the applied potential from the total potential calculated at the given time step. The resultant shape of the space charge potential is an affect of both the distribution of the incoming beam as well as the configuration of the electrode structure. Finally, the graph located in the bottom of the figure plots the calculated space charge potential at regular time intervals of 0.01 s until equilibrium is established. For the individual temperature maps

Figure 4.6: 3DCylPIC results for the collection of the ion (black) and electron (red) ionization pairs created for incoming beam rates of 10^2, 10^3, 10^4, and 10^5 pps. The time required to reach an equilibrium state was 0.13, 0.13, 0.12, and 0.10 s, respectively. See text for details.

obtained from each time step, please see Appendix B.

Since higher incoming beam rates are associated with higher space charge potentials and higher space charge potentials can have negative effects on extraction efficiencies, it was also important to study the strength of this potential at increasing incoming beam rates. The results from this study are shown in Fig. 4.8. Note that the intensity of the space charge potential dramatically increases at rates higher than 10^5 pps. Therefore, the space charge results as a whole indicated that the performance of the NSCL's large volume linear gas cell would decrease significantly at incident beam rates higher than 10^5 pps. Although these calculated results are generally consistent with the experimental results shown in Fig. 3.15, the cone located in the extraction region of the cell was unaccounted for by the 3DCycPIC

Figure 4.7: 3DCylPIC initial potential, equilibrium space charge potential, and evolution of the space charge potential for an incoming beam rate of 10^4 pps. The space charge potential was determined by subtracting the initial potential at Time = 0.00 s from the total potential at each time step.

calculation. For a more complete simulation, the space charge potential calculated for the body of the cell was incorporated into the SIMION model discussed below.

4.4 SIMION

SIMION is a commercial software package that calculates electromagnetic fields and the trajectories of charged particles that migrate in those fields. The code includes the electrode configuration, initial particle distributions, applied electric and magnetic voltages, and buffer gas presence. SIMION can simulate trajectories in either 2D or 3D space [8], and for the

74

Figure 4.8: Comparison of the equilibrium space charge potentials calculated for various incoming beam rates. See text for further details.

present work, it was used to predict the trajectories of ^{76}Ga ions through a 3D-model space. This space replicated the electrode geometry, applied electric fields, space charge potential (from 3DCycPIC), and helium buffer gas conditions of the large volume linear gas cell. Results from these simulations were then compiled and compared to the various experimental results with respect to the extraction efficiency as a function of the incoming beam rate.

The SIMION 3D-model began with recreating the electrode structure located within the NSCL's large volume linear gas cell. As discussed in Chapter 2, the body of the gas cell contains ∼750 thin, closely packed, independent electrodes. Each electrode includes 12 spokes that are 30 degrees apart from one another and vary in size. These structures help guide the ions of interest to the extraction region while simultaneously collecting the helium ions created during the ionization process. The extraction region of the cell contains an RF cone composed of ∼280 thin, closely packed, independent, concentric ring electrodes that decrease in diameter from ∼246 mm to ∼2.74 mm. The SIMION gas cell as a whole, as well as a comparison between the actual and simulated body and cone electrode structures are

75

Figure 4.9: Above: The SIMION models of the body and cone electrodes are compared to photographs of the actual electrode structures. Below: The SIMION gas cell model as a whole.

shown in Fig. 4.9. Next, the appropriate RF and DC potentials along with the helium buffer gas atoms were added to the model. Finally, the space charge potential calculated with the 3DCycPIC code was applied, and the LISE++ distribution of ^{76}Ga ions was migrated through the SIMION system.

As previously discussed, the space charge potential grew with increased incoming beam rates. This potential is evident by the increased variation in the equipotential lines just upstream of the cone in the SIMION results shown in Fig. 4.10. Although the field lines and therefore the potential experienced by the ions are affected by the space charge, eventually all of the ions are collected in the simulation. By combining the near 100% collection in both the 3DCycPIC and SIMION results for the simulated beam rates with the 0.84(0.04) stopping efficiency, 0.33(0.05) detector efficiency, 0.85(0.05) transmission efficiency through the window, and the 0.79(0.02) beam purity, the expected extraction efficiency for the large volume linear gas cell can be calculated to be 0.19(0.05).

Figure 4.10: SIMION results obtained for Y vs X where X is the length of the gas cell. The ion beam (blue) is shown to follow the equipotential lines (red) through the gas cell. Here, the ion beam consisted of 1000 ^{76}Ga ions that were distributed in accordance with the LISE++ results, and the equipotential lines were shaped by both the DC and RF applied potentials as well as the calculated space charge potential. The beam rate (in pps) associated with the space charge potential applied is shown in the upper right corner of each figure. "NONE" indicates that no space charge potential was included in the simulation.

The 3DCycPIC and thereby the SIMION simulations, however, only account for the space charge effects within the body of the gas cell. Not only do these simulations exclude space charge effects within the cone of the cell, they also exclude gas flow, and any losses from decay. Given the number of ions that have to pass through the nozzle, increased space charge effects could be experienced by the ions in the cone. Moreover, larger space charge potentials cause the ions to travel along the walls of the gas cell which could increase the necessary extraction time. Considering these exceptions, it is suspected that the losses at higher incoming beam rates ($\geq 10^5$ pps) result from space charge affects within the cone of the gas cell and/or decay losses. More detailed simulations of the ions' behavior in the cone and the time required for the ions to move down the walls of the gas cell are, therefore, required to fully understand the observed experimental losses.

Chapter 5

Outlook and Summary

Given the success of the NSCL's large volume linear gas cell and the increasing demand for experiments with thermalized ion beams, additional enhancements and operating conditions are currently being explored that could improve the thermalized beam purities, increase the variety of ions that can be thermalized by the system, and reduce the space charge and plasma effects experiend by the ions of interest. These next generation devices can be incorporated into both the present NSCL beam thermalization area as well as in the beam thermalization area for the next generation FRIB facility.

5.1 New Operating Practices

Impurities in the buffer gas, although significantly reduced by additional vacuum pumping when the gas cell is not being used, are still present and observable in the beams delivered from the current large volume linear gas cell. Operating at cryogenic temperatures can potentially eliminate impurities and provide cleaner, or non-fractionated, ion beams to experimenters. Along with lowering impurity levels, the extraction time can also be reduced by implementing a new ion transport technique– ion surfing. Ion surfing promises shorter extraction times which will allow more exotic nuclei to be thermalized and studied by experimenters. Finally, new geometries and set-ups will allow for the more efficient removal of the buffer gas ions produced during the thermalization process. These ions are ultimately

attributed with the efficiency losses caused through space charge and plasma effects. Effective removal of these unwanted buffer gas ions would therefore lead to higher efficiencies and rate capabilities of the thermalization systems.

5.1.1 Cryogenic Operation

Molecular impurities in the buffer gas arise from the buffer gas supply, outgassing of the chamber, and backstreaming from the vacuum pumps [56]. As discussed in the previous chapters, these impurities can react with the ion of interest while they are drifting towards the exit and even after extraction [56] resulting in a distribution of the radioactivity over a large range of masses. Impurity ions can also charge exchange with buffer gas ions and lead to stable contaminant beams. The radioactive ion distribution and contaminant beams can reduce the overall extraction efficiency of the system and the beam purity, respectively.

Although special measures can be taken to ensure the cleanliness of the set-ups and systems–such as using ultra high purity helium, ensuring ultra high vacuum standards are met, and baking the chamber–current room temperature devices have typical impurity levels on the order of ppb [56]. Such is the case for the present chamber which can only be heated to $\sim$60°C due to its indium metal seals. At temperatures below $\sim$40K, though, the majority of molecular contaminants will freeze out of the gas phase, which improves efficiencies and also allows a wider variety of materials to be used for fabrication. Along with improving the efficiencies and the beam qualities, the NSCL is also working to improve the extraction times of large gas cells.

Figure 5.1: Cartoon of ion surfing concept where the ions are transported by a traveling wave that is superimposed over an RF potential [60].

5.1.2 Ion Surfing

One of the improvements made to previous ion transport techniques was the addition of stacked ring electrodes along the body of the gas cell. As discussed in Chapters 2 and 3, the transport time was limited by the maximum electric field that could be applied before dielectric breakdowns occur within the helium buffer gas. "Ion surfing" was recently proposed [59] and proven to be [60] a successful transport method for thermal ions.

The surfing method simplifies the electrode system design while also significantly improving transport speeds. Similar to the current gas cell's method, this method also relies on an RF repelling force. Here, however, the ions are moved by a traveling wave potential parallel to the surface of a multi-electrode carpet, as seen in Fig. 5.1. Only four RF signals and one static (DC) push voltage are required to ensure quick and efficient transport of ions. Results from the ion surfing method showed reliable operation with ion transport speeds greater than 60 m/s [61].

These speeds are at least twice that possible with current stopping systems which can have significant implications on extraction times. For example, the average ion extraction

times for the NSCL's large volume linear gas cell are on the order of 40 ms while the average ion extraction times with the ion surfing technique for a gas cell of similar length would be on the order of 10 ms or less [2, 60, 62]. Such short extraction times would allow collection of the vast majority of producable exotic nuclei. Given these possibilities, the NSCL is developing new cryogenic gas cells that will also incorporate the ion surfing technique as part of its thermal beam development program.

5.2   ACGS

The Advanced Cryogenic Gas Stopper (ACGS) [62], is one such cell currently under development at the NSCL. Similar to the current NSCL gas cell, this device is also a large volume linear gas cell with an extraction area that extends the length of the cell. The ACGS, however, will be operated at cryogenic temperatures ($\sim$40K) and will incorporate the ion surfing technique [59] with a simple but innovative geometry.

The geometry for the current NSCL large volume linear gas cell consists of concentric electrodes located along the walls of the stopping chamber which extends the extraction area the entire length of the cell. Positively charged helium buffer gas ions produced from the thermalization process are collected on these chamber electrodes while the electrons produced are collected on a thin window. The ions of interest are guided and focused through the cell by applied DC and RF fields to a supersonic nozzle where they are jetted into a differentially pumped ion guide system. A detailed discussion of these processes was given in Chapter 3.

The geometry for the ACGS, shown schematically in Fig. 5.2 [62], is considerably different. A horizontal RF-based, ion surfing capet is positioned in the middle of the stopping chamber while push electrodes are located on the top and bottom of the chamber. Electrons

Figure 5.2: Conceptual design of the ACGS [62].

are collected on the push electrodes while the positively charged ions are pushed toward the central carpet. Once the ions reach the carpet surface, they are prevented from leaving in the transverse direction by additional lateral electrodes. Remember that the force exerted by an RF field is both position and mass dependent. Therefore, the light, unwanted helium buffer gas ions that lead to space charge and plasma effects can be collected on the carpet surface while the ions of interest are guided to the extraction region.

The extraction region is composed of two vertical, concentric circular ion surfing carpets that are used to transport the ions of interest to the extraction orifice. Due to the quick and efficient neutralization of the helium ions on the central carpet as well as the expected extraction speeds, this geometry is expected to increase the beam rate capability of the device by more than an order of magnitude with respect to other linear gas cells [62]. Although similar upgrades have been and will continue to be implemented to improve the efficiencies of linear gas cells, these cells are inexorably limited by their finite size with respect to the thermalization of light ions.

82

5.3 Cycstopper

In an attempt to create the conditions required to successfully thermalize ions of all masses at high incoming beam rates, the NSCL is currently developping a gas-filled reverse cyclotron, dubbed the "cycstopper." This next generation stopping device will operate at cryogenic temperatures, employ the ion surfing technique, and offer an "infinite" stopping distance in low pressure gas [63, 64, 65].

5.3.1 Concept

The ultimate limitations of linear gas cells arise from the size of the range straggling of light energetic projectile fragments compared to the length of the gas cells. Recall from Chaper 1, that the linear stopping power of a material, also called specific energy loss, is proportional to mZ^2/E. Thus, higher kinetic energies and lower atomic numbers lead to longer ranges. Substituting the Bethe formula for specific energy loss (3.2) into the range equation, the relationship between the range of an ion and its mass, m can be described as:

$$R \propto \frac{E_o^{\frac{3}{2}}}{\sqrt{m}}, \tag{5.1}$$

which show that ions with smaller atomic numbers and lighter masses have a much longer range within a material.

Therefore, in order to thermalize the lightest ions, either the stopping power of the gas would have to be increased and/or the length of the cell would need to be increased. Unfortunately, both of these options have significant consequences. Increasing the stopping power of the gas would require either a higher density buffer gas and/or higher gas pressures.

As discussed in Chapter 2, helium is the best buffer gas given that it has the highest ionization potential of any other element. This high potential leads to most of the ions of interest retaining their charge and exiting the chamber in either the 1^+ or 2^+ charge state. Changing the buffer gas could, therefore, lead to increased losses from neutralization. Higher gas pressures or longer gas cells would both lead to increased extraction times. Increasing the extraction time, increases the half life limit of ions that could survive the thermalization process and be delivered to other experimental set-ups.

5.3.2   Design and Capabilities

Various differences exist between linear gas stoppers and the cyclotron gas stopper, shown schematically in Fig. 5.3 [64]. For example, the degrader systems employed by linear gas cells are typically located upstream of the cell whereas the degrader system employed by the cycstopper is part of the device itself. Also, linear devices have cylindrical gas chambers that are located on the beam axis whereas the cycstopper has a disk-like gas chamber that is located tangent to the incoming beam axis. Finally, linear gas cells do not employ a magnetic field whereas the cycstopper exploits the focusing properties, or spiraling effect that a sectored cyclotron magnet has on charged particles [63, 64, 65].

Fast ions are injected into the cycstopper through a beam port located on the outer radius of the device. As the ions ener the roughly 2T magnetic field, they are passed through an adjustable solid degrader and begin to spiral. This motion is confined both radially and axially by the magnetic field and carries the ions into the gas stopping chamber. The thermalization process, or collisions with the buffer gas atoms, causes the ions radii of trajectory to decrease until they reach the center of the chamber which also corresponds to the center of the device. Similar systems have been used to successfully thermalize antiprotons,

Figure 5.3: Conceptual design of the cycstopper [64].

pions, and muons, and have also been previously proposed for stopping light ions [63, 64]. From here, the now thermal ions are moved to the extraction region of the device by RF-carpets [63, 64, 65].

Since the ions are free to make multiple turns within the gas, the mass thickness encountered by the ions will vary depending on the ion's range. Given that light ions have a longer range, these ions will simply make more turns in the gas before thermalization is achieved. This "infinite" stopping volume will allow lower gas pressures to be used which not only reduces the space charge effects but also ensures efficient functionality of the RF techniches employed [63].

As previously discussed, space charge and plasma affects are attributed with the most significant efficiency losses. These affects arise from the insufficient removal of helium ions created during the thermalization process. By applying an electric field in the same direction as the magnetic field, the cycstopper should be able to efficiently remove both the helium ions and electrons created during the thermalization process. Efficient removal of these pairs will also significantly decrease the space charge and plasma effects inside the gas and thereby,

85

Figure 5.4: Left: Rendering of the mechanical model of the cyclotron gas stopper with an indication of the spiral path of a stopping ion [65]. Right: Photograph of the cyclotron-stopper magnet in the open state showing the pole pieces.

further increase the extraction efficiency of the system [64, 65].

Simulation results for the cystopper confirm significantly enhanced stopping and extraction efficiencies for light and medium massed ions when compared to current linear gas cells [65]. Construction of this device is nearly complete, and characterization tests are currently underway. Figure 5.4 shows a mechanical drawing of the cyclotron gas stopper [65] along side a photograph of the device in its current state.

5.4 Summary

The present work has explored the capabilities of a new large volume linear gas cell for the thermalization of projectile fragments. Experimental results from this device indicated improved performance compared to earlier devices, and simulations were employed to un-

derstand the observed behavior. It can be concluded that this improved performance was a result of the larger stopping volume, improved electrode structure, and additional RF potential which increased the stopping efficiency, decreased the space charge potential, and increased the extraction efficiency, respectively. Although the simulated results accounted for a majority of the experimental losses, more detailed simulations of the ions' behavior in the cone of the gas cell and the time required for the ions to move down the walls of the cell are required to account for the losses observed at higher incoming beam rates ($\geq 10^5$ pps). A few issues also remain with regard to beam purity, extraction times, and the collection of the lightest ions that next generation devices are being developed to address.

APPENDICES

Appendix A

: SRIM Example

The TRIM setup window shown in Fig. A.1 contains the experimental parameters used during the ^{76}Ga commissioning experiments. These parameters include an adjustable aluminum degrader, 1050 μm-thick silicon dioxide (glass) wedge, 10 μm-thick aluminum window, 120 cm-long helium gas volume, and a 1000 μm-thick aluminum back wall for completeness. While most of the material densities were standard and set as pictured, the density of the gas was calculated to be 2.06 x 10^{-5} g/cm^3. This density was calculated for the operating temperature and pressure of -4°C and 123 mbar, respectively. The final parameters include the identity and mass of the ion of interest as well as its kinetic energy. The kinetic energy was calculated to be 6864870 keV by the "physical calculator" in the LISE++ program.

During commissioning, the degrader thickness nor the kinetic energy of the beam remained constant. As such, these parameters are highlighted with a gold box in Fig. A.1. Although the effective thickness of the degrader was intentionally varied, the kinetic energy of the ions inherently varied due to a 0.5% momentum spread. These variations were accounted for by manually changing the settings and re-running the simulation. The ionization and range results from all of the associative simulations were combined and compared to the experimentally determined values as shown in Chapter 4.

Figure A.1: TRIM setup window with example parameters from the ^{76}Ga commissioning experiments.

Appendix B

: 3DCycPIC

B.1 Example Configuration File

The 3DCycPIC configuration file used for the highest incoming beam rate of 6.2 x 10^5 is shown in Fig. B.1. A simple description of each value is given in the .config file. The values highlighted in yellow are the scale factor for the charge values. This factor, as discussed in Chapter 3, is calculated with the equation [58]:

$$chargescale = \frac{\Phi_{RI} * \bar{E} * \Delta t}{E_{IP} * \Phi_{IP}},$$ (B.1)
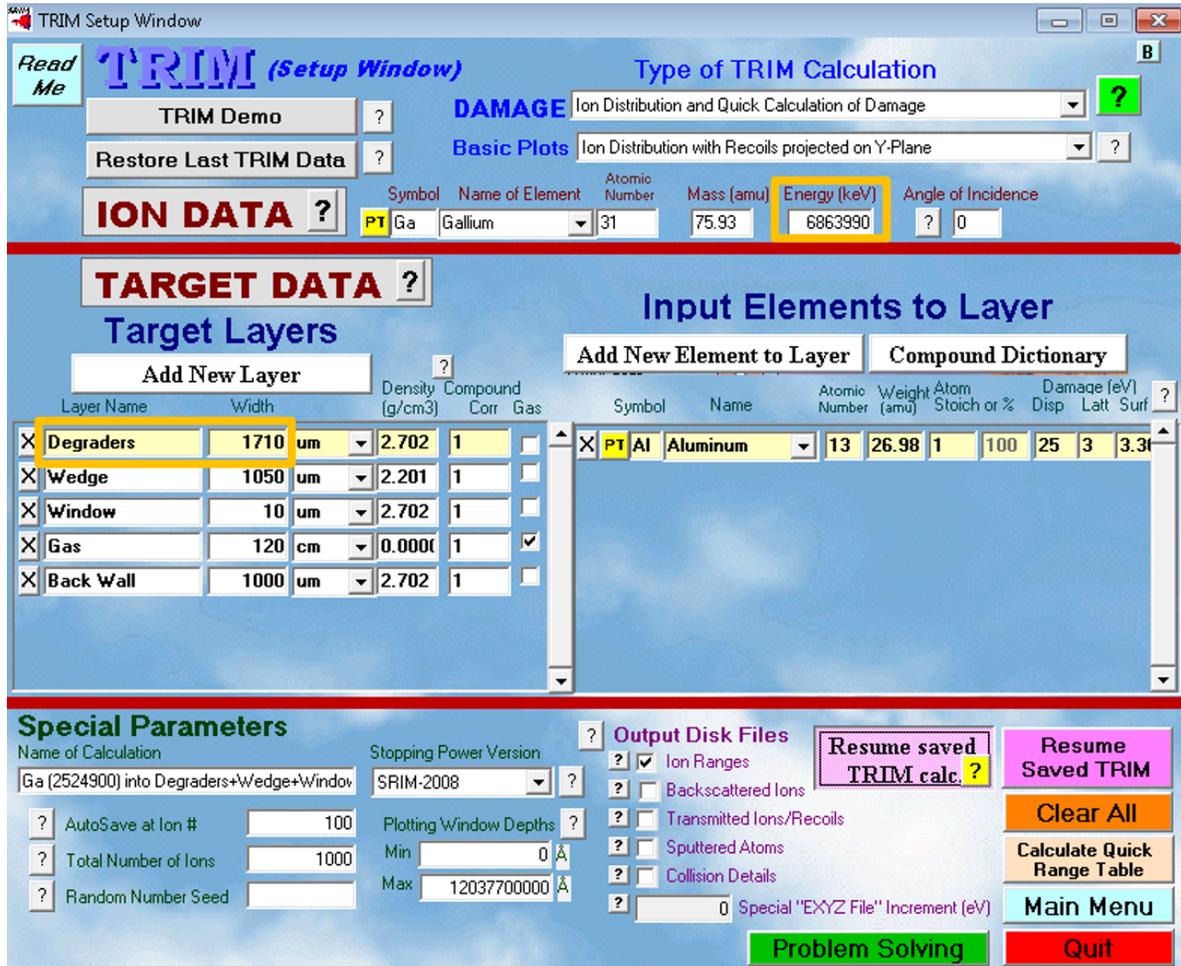
The values highlighted in blue are obtained from the LISE++ projections in the X, Y, and Z planes, and the values highlighted in green are the main, variable experimental parameters. Finally, the values highlighted in purple are the main, adjustable parameters specific to the PIC simulation. The number of ions released per time step, as well as the time step itself and ion advancement steps, control the resolution of the simulation. As the resolution is increased, though, the amount of time required to run the simulation also increases. Therefore, these values are optimized for resolution and simulation time, where the electrons can not adavance further than one grid unit per time step and the time required to run the simulation is less than two days.

```
# Configuration file for ANL_GC_3DCyl
# INITIAL ION AND ELECTRON DISTRIBUTION
# -------------------------------------------------------------------------------
numions                 = 5000000     # number of ions
numelectrons            = 5000000     # number of electrons
ionmass                 = 4           # ion mass in amu
ioncharge               = 1           # ion charge in e
ionchargescale          = 33922       # scale the ion charge for increased space charge
electronmass            = 5.486e-4    # electron mass in amu
electroncharge          = -1          # electron charge in e
electronchargescale     = 33922       # scale the electron charge for increased space charge
ionreleasestep          = 1           # release ions every X timesteps
numionsreleased         = 5           # release X number of ions
electronreleasestep     = 1           # release electrons every X timesteps
numelectronsreleased    = 5           # release X number of electrons
xo                      = 0           # mean x position of initial ion/electron distribution in m
yo                      = 0           # mean y position of initial ion/electron distribution in m
zo                      = -0.52591    # mean z position of initial ion/electron distribution in m
sigx                    = 0.026       # 1 stand. dev. in x of initial ion/electron distribution in m
sigy                    = 0.055       # 1 stand. dev. in y of initial ion/electron distribution in m
sigz                    = 0.519       # 1 stand. dev. in z of initial ion/electron distribution in m
# -------------------------------------------------------------------------------
# RF AND FIELDS
# -------------------------------------------------------------------------------
frontendpot             = 900         #potential at z = z0 boundary in V
seg1pot                 = 900         #first segment potential in V
seg2pot                 = 673         #first segment potential in V
seg3pot                 = 447         #first segment potential in V
seg4pot                 = 220         #first segment potential in V
seg5pot                 = 210         #first segment potential in V
seg6pot                 = 20          #first segment potential in V
backendpot              = 3           #potential at z = z1 boundary in V
# -------------------------------------------------------------------------------
# BUFFER GAS
# -------------------------------------------------------------------------------
buffergasmass           = 4           # mass of buffer gas in amu
gastemp                 = 269         # temperature of buffer gas in K
gaspress                = 123         # pressure of buffer gas in mbar
gaspol                  = 1.02e-40    # electric polarizability of background gas atom in F*m^2
iondiameter             = 1e-9        # diameter of ion in m
ionko                   = 10e-4       # reduced mobility of ion in buffer gas in m^2/(V*s)
electronko              = 10000e-4    # reduced mobility of electron in buffer gas in m^2/(V*s)
numunitvecs             = 100000      # number of unit vectors to generate for collisions
# -------------------------------------------------------------------------------
# SIMULATION PARAMETERS
# -------------------------------------------------------------------------------
runtime                 = 0.02005     # total simulation time in s
dt                      = 5e-7        # time step in s
iondtmultiplier         = 10          # advance ions every Xth timestep
bufflength              = 100         # buffer size for position recording (not used)
infodisplaycount        = 100         # print info every X time steps
deadionskip             = 4           # record every nth dead ion
deadelectronskip        = 100         # record every nth dead electron
writedatafiles          = yes         # yes to record potentials, part. pos. files (caps sensitive)
potdatacount            = 20000       # write potential and position files every nth timestep
ionregencount           = 10000       # regenerate dead ions every X timesteps
electronregencount      = 10000       # regenerate dead electrons every X timesteps
capmatfilename          = ANL_GC_3DCyl_v2.capmat    # file name of capacity matrix file
```

Figure B.1: PIC config file example from the ^{76}Ga commissioning simulations.

B.2 Example Temperature Maps

Since the space charge potential evolves over time, it is possible to track its development until equilibrium is reached. Temperature maps show the potential at a given Z slice through the gas cell. Example maps, along with a graph that summarized the evolution of the space charge potential for an incoming beam rate of 10^4 pps, was shown in Chapter 4 (Fig. 4.7). The individual temperature maps used to create this graph are shown in Fig. B.2. While the applied potential is shown in the top left map, only the space charge potential is shown in the remaining maps. In order to solely view and determine the space charge potential, the applied potential was subtracted from the total potential calculated for each time interval. The resultant shape of the space charge potential is an affect of both the distribution of the incoming beam as well as the configuration of the electrode structure.
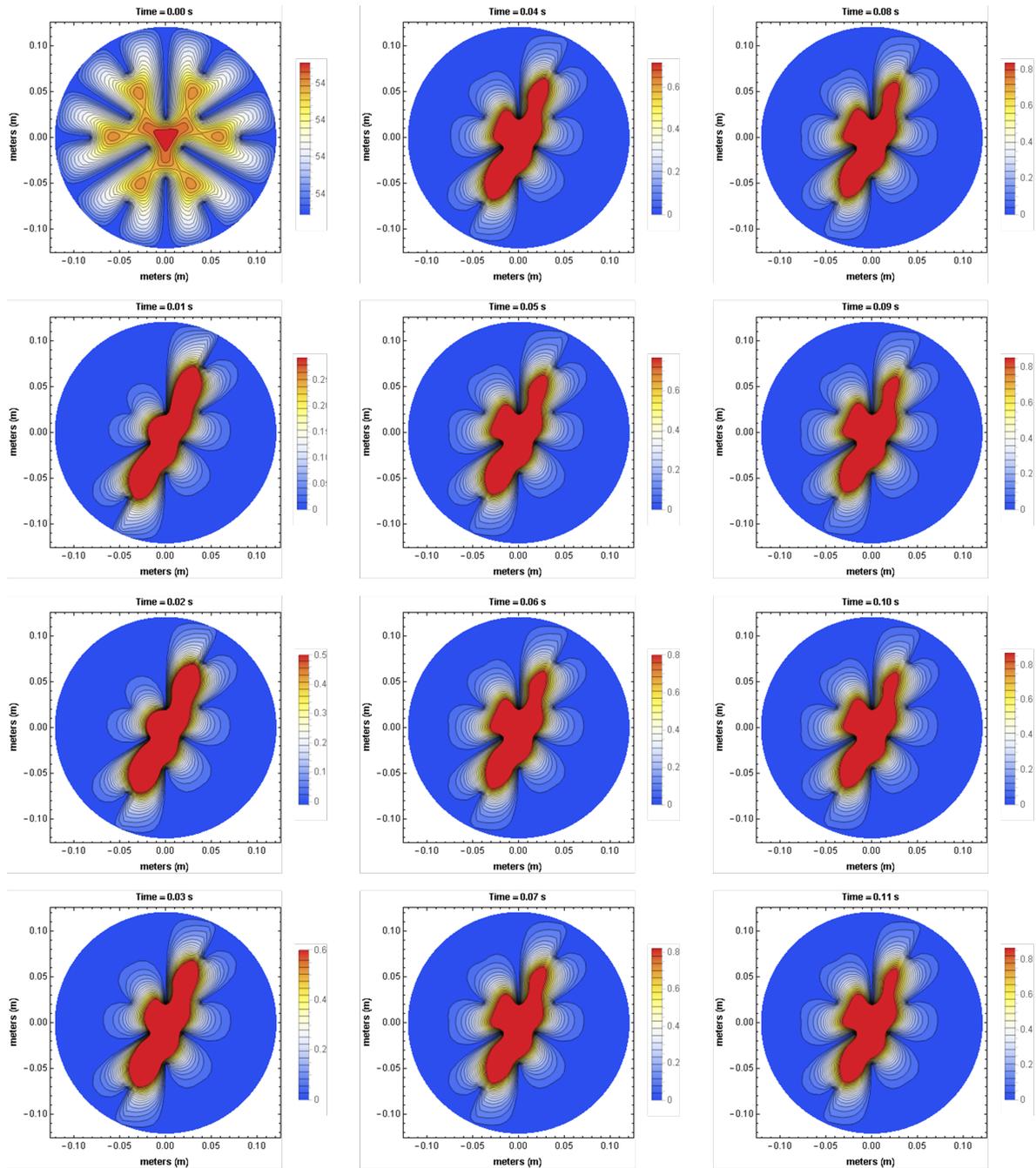
Figure B.2: Evolution of the space charge potential (in Volts) as a funtion of time for an incoming beam rate on the order of 10^4 pps. This space charge potential was determined by subtracting the initial electrode potential at Time = 0.00 s from the total potential at each time step.

REFERENCES

REFERENCES

[1] L. Weissman, P. A. Lofy, D. A. Davies, D. J. Morrissey, P. Schury, S. Schwarz, T. Sun, and G. Bollen. First extraction tests of the nscl gas cell. *Nuc. Phys. A*, **746** (2004) 655c–648c.

[2] K. Cooper, C. S. Sumithrarachchi, D. J. Morrissey, A. Levand, J. A. Rodriguez, G. Savard, S. Schwarz, and B. Zabransky. Extraction of thermalized projectile fragments from a large volume gas cell. *Nuc. Instr. and Meth. A*, **763** (2014) 543–546.

[3] J. F. Ziegler, M. D. Ziegler, and J. P. Biersack. SRIM - the stopping and range of ions in matter (2010). *Nuc. Instr. and Meth. B*, **268** (2010) 1818–1823.

[4] J.F. Ziegler. The SRIM energy-loss package. `http://www.srim.org/`.

[5] O. Tarasov and D. Bazin. LISE++: Radioactive beam production with in-flight separators. *Nuc. Instr. and Meth. B*, **266** (2008) 4657–4664.

[6] O.B. Tarasov and D. Bazin. LISE++: design your own spectrometer. *Nuc. Phys. A*, **746** (2004) 411–414. `http://lise.nscl.msu.edu/lise.html`.

[7] R. Ringle. 3DCylPIC - a 3D particle-in-cell code in cylindrical coordinates for space charge simulations of ion trap and ion transport devices. *Intl. J. Mass Spectr.*, **303** (2011) 42–50.

[8] D. A. Dahl. SIMION for the personal computer in reflection. *Intl. J. Mass Spectr.*, **200** (2000) 3–25. `http://simion.com/`.

[9] D. J. Morrissey and B. Sherrill. Radioactive nuclear beam facilities based on projectile fragmentation. *Phil. Trans. R. Soc. Lond. A*, **356** (1998) 42–50.

[10] P. Dendooven. The development and status of the IGISOL technique. *Nuc. Instr. and Meth. B*, **126** (1997) 182–189.

[11] R. D. Macfarlane and R. D. Griffioen. A system for studying acelerator-produced short-lived alpha emitters. *Nuc. Instr. and Meth.*, **24** (1963) 461–464.

[12] Joseph Cerny (editor). *Nuclear Spectroscopy and Reactions: Part A*, volume 40-A (Academic Press, New York and London1974).

[13] W. Wiesehahn, G. Bischoff, and J. D'auria. The role of cluster size in a gas jet transport system. *Nuc. Instr. and Meth.*, **129** (1975) 187–192.

[14] J. Äystö, P. Puumalainen, and K. Valli. The carrier-loaded helium-jet transport method. *Nuc. Instr. and Meth.*, **115** (1974) 65–73.

[15] H. Wollnik, H. G. Wilhelm, G. Robig, and H. Jungclas. The improvement of a gas-jet system by the use of an aerosol generator. *Nuc. Instr. and Meth.*, **127** (1975) 539–545.

[16] W. D. Schmidt-Ott, R. L. Mlekodaj, E. H. Spejewski, and H. K. Carter. He-jet on-line ion source of the unisor mass separator. *Nuc. Instr. and Meth.*, **124** (1975) 83–91.

[17] J. Äystö, V. Rantala, K. Valli, S. Hillebrand, M. Kortelahti, K. Eskola, and T. Raunemaa. Efficiency of an on-line isotope separator system employing cooled and NaCl-loaded He-jet methods. *Nuc. Instr. and Meth.*, **139** (1976) 325–329.

[18] V.T. Koslowsky, M.J. Watson, E. Hagberg, J.C. Hardy, W.L. Perry, M.G. Steer, H. Schmeing, P.P. Unger, and K.S. Sharma. The Chalk River high-temperature helium-jet ion source. *Nuc. Instr. and Meth. B*, **70** (1992) 245–253.

[19] S. Ichikawa, M. Asai, K. Tsukada, A. Osa, T. Ikuta, N. Shinohara, H. Iimura, Y. Nagame, Y. Hatsukawa, I. Nishinaka, K. Kawade, H. Yamamoto, M. Shibata, and Y. Kojima. Mass separation of neutron-rich isotopes using a gas-jet coupled thermal ion source. *Nuc. Instr. and Meth. A*, **374** (1996) 330–334.

[20] R. Kirchner. Review of isol target-ion-source systems. *Nuc. Instr. and Meth. B*, **204** (2003) 179–190.

[21] P. Van Duppen, P. Decrock, M. Huyse, and R. Kirchner. High efficiency ion sources for on-line mass separators: A brief review. *Rev. Sci. Instrum.*, **63** (1992) 2381–2386.

[22] J. Äystö. Development and applications of the IGISOL technique. *Nuc. Phys. A*, **693** (2001) 477–494.

[23] Glenn F. Knoll. *Radiation Detection and Measurement* (Jon Wiley & Sons, Inc., New Jersey2010), 4th edition.

[24] J. Ärje and K. Valli. Helium-jet ion guide for an on-line isotope separator. *Nuc. Instr. and Meth.*, **179** (1981) 533–539.

[25] J. Ärje. Charge creation and resent mechanisms in an ion guide isotope separator (IGIS). *Physica Scripta*, (1983) 37–40.

[26] I.D. Moore, T. Kessler, T. Sonoda, Y. Kudryavstev, K. Peräjärvi, A. Popov, K.D.A Wendt, and J. Äystö. A study of on-line gas cell processes at IGISOL. *Nuc. Instr. and Meth. B*, **268** (2010) 657–670.

[27] A. Iivonen, K. Riikonen, R. Saintola, K. Valli, and K. Morita. Focusing ions by viscous drag and weak electric fields in an ion guide. *Nuc. Instr. and Meth. A*, **307** (1991) 69–79.

[28] H.J. Xu, M. Wada, J. Tanaka, H. Kawakami, I. Katayama, and S. Ohtani. A new cooling and focusing device for ion guide. *Nuc. Instr. and Meth. A*, **333** (1993) 247–281.

[29] R. Ringle, G. Bollen, A. Prinke, J. Savory, P. Schury, S. Schwarz, and T. Sun. The LEBIT 9.4T Penning trap mass spectrometer. *Nuc. Instr. and Meth. A*, **604** (2009) 536–547.

[30] K. Minamisono, P.F. Mantica, A. Klose, S. Vinnikova, A. Schneider, B. Johnson, and B.R. Barquest. Commissioning of the collinear laser spectroscopy system in the BECOLA facility at the NSCL. *Nuc. Instr. and Meth. A*, **709** (2013) 85–94.

[31] A. Lapierre, S. Schwarz, K. Kittimanapun, J.A. Rodriguez, C. Sumithrarachchi, B. Barquest, E. Berryman, K. Cooper, J. Fogleman, S. Krause, J. Kwarsick, S. Nash, G. Perdikakis, M. Portillo, R. Rencsok, D. Skutt, M. Steiner, L. Tobos, W. Wittmer, G. Bollen, and D. Leitner. Commissioning results of the ReA EBIT charge breeder at the NSCL: first reacceleration of stable-isotope beams. *Nuc. Instr. and Meth. B*, **317** (2013) 399–401.

[32] Walter Loveland, David J. Morrissey, and Glenn T. Seaborg. *Modern Nuclear Chemistry* (John Wiley and Sons Inc, New Jersey2006).

[33] D.J. Morrissey and B.M. Sherrill. Radioactive nuclear beam facilities based on projectile fragmentation. *Phil. Trans. R. Soc. Lond. A*, **356** (1998) 1985–2006.

[34] D.J. Morrissey, B.M. Sherrill, M. Steiner, A. Stolz, and I. Wiedenhoever. Commissioning the A1900 projectile fragment separator. *Nuc. Instr. and Meth. B*, **204** (2003) 90–96.

[35] M. Wada, Y. Ishida, T. Nakamura, Y. Yamazaki, T. Kambara, H. Ohyama, Y. Kanai, T.M. Kojima, Y. Nakai, N. Ohshima, A. Yoshida, T. Kubo, Y. Matsuo, Y. Fakuyama, K. Okada, T. Sonoda, S. Ohtani, K. Noda, H. Kawakami, and I. Katayama. Slow RI-beams from projectile fragment separators. *Nuc. Instr. and Meth. B*, **204** (2003) 570–581.

[36] G. Savard. Large radio-frequency gas catchers and the production of radioactive nuclear beams. *Journal of Physics: Conf. Series*, **312** (2011) 052004: 1–9.

[37] L. Weissman, P.A. Lofy, D.A. Davies, D.J. Morrissey, P. Schury, S. Schwarz, T. Sun, and G. Bollen. First extraction tests of the NSCL gas cell. *Nuc. Phys. A*, **746** (2004) 655c–658c.

[38] D.J. Morrissey. Extraction of thermalized projectile fragments from gas. *Eur. Phys. J. Special Topics*, **150** (2007) 365–366.

[39] G. Bollen. Ion traps–precision measurements and more. *Eur. Phys. J. A*, **15** (2002) 237–243.

[40] Ryan Ringle, Stefan Schwars, and Georg Bollen. Penning trap mass spectrometry of rare isotopes produced via projectile fragmentation at the LEBIT facility. *Intl. J. Mass Spectr.*, **349**.

[41] A.A. Valverde, G. Bollen, M. Brodeur, R.A. Bryce, K. Cooper, M. Eibach, K. Gulyuz, C. Izzo, D.J. Morrissey, M. Redshaw, R. Ringle, R. Sandler, S. Schwarz, C.S. Sumithrarachchi, and A.C.C. Villari. First direct determination of the superallowered β-decay of Q_{EC} value for ^{14}O. *Phys. Rev. Lett.*, **114** (2015) 232502:1–5.

[42] R. Ringle, P. Schury, T. Sun, G. Bollen, D. Davies, J. Huikari, E. Kwan, D.J. Morrissey, A. Prinke, J. Savory, S. Schwarz, and C. Sumithrarachchi. Precision mass measurements with LEBIT at MSU. *Intl. J. Mass Spectr.*, **251** (2006) 300–306.

[43] A.A. Valverde, G. Bollen, K. Cooper, M. Eibach, K. Gulyuz, C. Izzo, D.J. Morrissey, R. Ringle, R. Sandler, S. Schwarz, C.S. Sumithrarachchi, and A.C.C. Villari. Penning trap mass measurement of ^{72}Br. *Phys. Rev. C*, **91** (2015) 037301:1–3.

[44] R. Ringle. Recent high-precision Penning trap mass measurements performed at LEBIT. *Hyperfine Interact.*, **196** (2010) 215–217.

[45] D.M. Rossi, K. Minamisono, H.B Asberry, G. Bollen, B.A. Brown, K. Cooper, B. Isherwood, P.F. Mantica, A. Miller, D.J. Morrissey, R. Ringle, J.A. Rodriguez, C.A. Ryder,

A. Smith, R. Strum, and C. Sumithrarachchi. Charge radii of neutron-deficient ^{36}K and ^{37}K. *Phys. Rev. C*, **92** (2015) 014305:1–9.

[46] T. M. Baumann, A. Lapierre, S. Schwarz, K. Kittimanapun, and G. Bollen. Energy spread and time structure of ion beams extracted from the ReA-EBIT rare isotope charge breeder. *AIP Conf. Proc.*, **1640** (2015) 80–87.

[47] L.E. Linhardt, L. Baby, D.W. Bardayan, J.C. Blackmon, H. Gardiner, E. Johnson, E. Koschiy, D.T. Macon, M. Matos, B.C. Rasco, G. Rogachev, D. Santiago-Gonzalez, and I. Wiedenhoever. Measurement of ^{17}F + p reactions with ANASEN. *J. Phys.:Conf. Ser.*, **403** (2012) 012036:(1–5).

[48] D. Suzuki, M. Ford, D. Bazin, W. Mittig, W.G. Lynch, T. Ahn, S. Aune, E. Galyaev, A. Fritsch, J. Gilbert, F. Montes, A. Shore, J. Yurkon, J.J. Kolata, J. Browne, A. Howard, A.L. Roberts, and X.D. Tang. Prototype AT-TPC: toward a new generation active target time projection chamber for radioactive beam experiments. *Nuc. Instr. and Meth. A*, **691** (2012) 39–54.

[49] A. Simon, S.J. Quinn, A. Spyrou, A. Battaglia, I. Beskin, A. Best, B. Bucher, M. Couder, P.A. DeYoung, X. Fang, J. Gőrres, A. Kontos, Q. Li, S.N. Liddick, A. Long, S. Lyons, K. Padmanabhan, J. Peace, A. Roberts, D. Robertson, K. Smith, M.K. Smith, E. Stech, B. Stefanek, W.P. Tan, X.D. Tang, and M. Wiesher. Sun: Summing NaI(Tl) gamma-ray detector for capture reaction measurements. *Nuc. Instr. and Meth. A*, **703** (2013) 16–21.

[50] D.W. Bardayan, K.A. Chipps, S. Ahn, J.C. Blackmon, U. Greife, K.L. Jones, A. Kontos, R.L. Kozub, L. Linhardt, B. Manning, M. Matos, P.D. O'malley, S. Ota, S.D. Pain, W.A. Peters, S.T. Pittman, A. Sachs, H. Schatz, K.T. Schmitt, M.S. Smith, P. Thompson, and The JENSA Collaboration. The JENSA gas-jet target for radioactive beam experiments at ReA3 and FRIB. *Physics Procedia*, **66** (2015) 451–456.

[51] S. Schwarz, M. Block, G. Bollen, C.M. Campbell, M. Facina, R. Ferrer, C.M. Folden III, A.A. Kwiatkowski, D.J. Morrissey, G.K. Pang, A.M. Prinke, R.J. Ringle, J. Savory, and P.H. Schury. Precision Penning trap mass measurements of rare isotopes produced by projectile fragmentation. *Eur. Phys. J. A*, **42** (2009) 323–326.

[52] B.R. Barquest. *An advanced ion guide for beam cooling and bunching for collinear laser spectroscopy of rare isotopes.* Ph.D. thesis, Michigan State University (2014).

[53] W. Trimble, G. Savard, B. Blank, J.A. Clark, F. Buchinger, T. Cocolios, J.E Crawford, A. Frankel, J.P. Greene, S. Gulick, J.K.P. lee, A. Levand, M. Portillo, K.S. Sharma, J.C. Wang, B.J. Zabransky, S. Shou, and the S258 Collaboration. Development and

first on-line tests of the RIA gas catcher prototype. *Nuc. Phys. A*, **746** (2004) 415c–418c.

[54] G. Savard, J. Clark, C. Boudreau, F. Buchinger, J.E. Crawford, H. Geissel, J.P. Greene, S. Gulick, A. Heinz, J.K.P. Lee, A. Levand, M. Maier, G. M'unzenberg, C. Scheidenberger, D. Seweryniak, K.S. Sharma, G. Sprouse, J. Vaz, J.C. Wang, B.J. Zabransky, Z. Zhou, and the S258 collaboration. Development and operation of gas catchers to thermalize fusion-evaporation and fragmentation products. *Nuc. Instr. and Meth. B*, **204** (2003) 582–586.

[55] H. Geissel, Th. Schwab, P. Armbruster, J.P. Dufour, E. Hanelt, K-H. Schmidt, B. Sherrill, and G. Münzenberg. Ions penetrating through ion-optical systems and matter–non-Liouvillian phase-space modeling. *Nuc. Instr. and Meth. A*, **282** (1989) 247–260.

[56] D.J. Morrissey, G. Bollen, M. Facina, and S. Schwarz. Pulsed extraction of ionization from helium buffer gas. *Nuc. Instr. and Meth. B*, **266** (2008) 4822–4828.

[57] M. Huyse, M. Facina, Y. Kudryavtsev, P. VanDuppen, and ISOLDE Collaboration. Intensity limitations of a gas cell for stopping, storing and guiding of radioactive ions. *Nuc. Instr. and Meth. B*, **187** (2002) 535–547.

[58] S.J. Harris and C.E. Doust. Energy per ion pair measurements in pure helium and helium mixtures. *Radiation Measurements*, **66** (1976) 11–18.

[59] G. Bollen. "Ion surfing" with radiofrequency carpets. *Intl. J. Mass Spectr.*, **299** (2011) 131–138.

[60] M. Brodeur, A.E. Gehring, G. Bollen, S. Schwarz, and D.J. Morrissey. Experimental investigation of the ion surfing technique. *Intl. J. Mass Spectr.*, **336** (2013) 53–60.

[61] A.E. Gehring. *Development of the "ion surfing" method for thermal ion transport in buffer gas.* Ph.D. thesis, Michigan State University (2013).

[62] G. Bollen. Private communication.

[63] G. Bollen, D.J. Morrissey, and S. Schwarz. A study of gas-stopping of intense energietic rare isotope beams. *Nuc. Instr. and Meth. A*, **550** (2005) 27–38.

[64] G. Bollen, C. Campbell, S. Shouhan, G. Guénaut, D. Lawton, F. Marti, D.J. Morrissey, J. Ottarson, G. Pang, S. Schwarz, A.F. Zeller, and P. Zavodszky. Manipulation of

rare isotope beams–from high to low energies. *Nuc. Instr. and Meth. B*, **266** (2008) 4442–4448.

[65] S. Schwarz, G. Bollen, M. Brodeur, S.S. Chouhan, J. DeKamp, A.E. Gehring, N.S. Joshi, C. Magsig, D.J. Morrissey, R. Ringle, J. Ottarson, and A.F. Zeller. The NSCL cyclotron gas stopper–under construction. *Nuc. Instr. and Meth. B*, **317** (2013) 463–467.